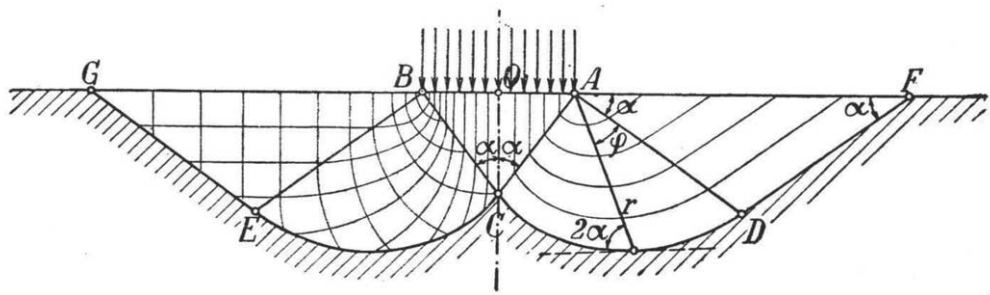
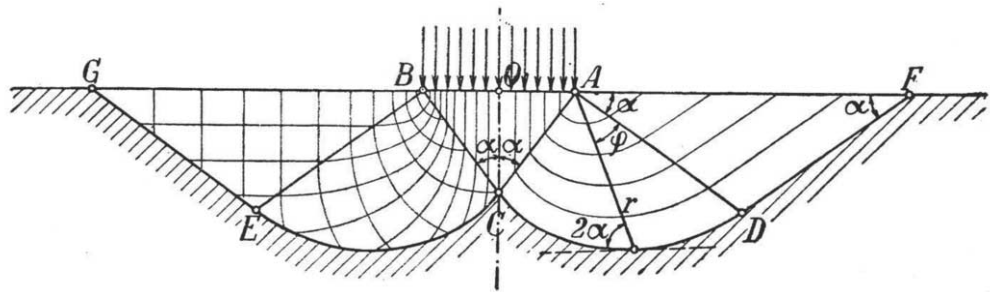


100 Years of Prandtl's Wedge



Original drawing of the Prandtl-wedge

100 Years of Prandtl's Wedge



Stefan Van Baars

© 2018. *The author and IOS Press. All rights reserved.*

This monograph is published online with Open Access by IOS Press and distributed under the terms of the Creative Commons Attribution Non-Commercial License 4.0 (CC BY-NC 4.0).

ISBN 978-1-61499-849-5 (print)

ISBN 978-1-61499-850-1 (online)

DOI 10.3233/978-1-61499-850-1-i

Key words: soil mechanics, foundation engineering, bearing capacity, footings

Publisher

IOS Press BV

Nieuwe Hemweg 6b

1013 BG Amsterdam

The Netherlands

tel: +31-20-688 3355

fax: +31-20-687 0019

email: info@iospress.nl

www.iospress.nl

LEGAL NOTICE

The publisher is not responsible for the use which might be made of the following information.

PRINTED IN THE NETHERLANDS

PREFACE

During the first few years working as professor in Foundation Engineering and Soil Mechanics at the Faculty of Science, Technology and Communication of the University of Luxembourg, I performed research on pile tip bearing capacity. I noticed that some researchers assume the shape of the failure mechanism around the pile tip, to be like a logarithmic spiral, in the same way as the failure mechanism for shallow foundations. I therefore started to study the bearing capacity of shallow foundations, and became fascinated by the beauty of the analytical solutions made a century ago.

Since the publication of Ludwig Prandtl's article "*About the hardness of a plastic body*", in 1920, a lot of extensions have been made, for example with inclination factors and shape factors. In addition, numerous laboratory experiments have been carried out and many numerical calculations have been performed. Furthermore, as mentioned, some researchers have even tried to extrapolate the failure mechanism for shallow foundations to the failure mechanism around the tip of a pile. All this scientific work leads back to the first publication of the so-called "Prandtl-wedge" of 1920.

This book "*100 Years of Prandtl's Wedge*" has been created for all those who are interested in these fundamentals of foundation engineering and their history.

Luxembourg, June 2015

Stefan Van Baars

CONTENTS

I PRANDTL & REISSNER.....	1
1 Introduction.....	3
2 Ludwig Prandtl	5
3 Hans Jacob Reissner	8
II ORIGINAL PUBLICATIONS	11
4 Prandtl's publication of 1920.....	13
4.1 Introduction.....	13
4.2 Prandtl-wedge	14
4.3 Prandtl-wedge, also discovered by Prandtl?.....	15
5 Reissner's publication of 1924	18
5.1 Introduction.....	18
5.2 Effect of the surcharge	18
III BEARING CAPACITY FACTORS.....	19
6 Prandtl-wedge	21
7 Surcharge bearing capacity factor N_q	25
7.1 Analytical solution	25
7.2 Numerical solution	26
8 Cohesion bearing capacity factor N_c	29
8.1 Analytical solution	29
8.2 Numerical solution	30
9 Soil-weight bearing capacity factor N_y.....	33
9.1 Scaled modelling.....	33
9.2 Numerical solution	35
10 Superposition and bearing capacity factors.....	38
10.1 Table of bearing capacity factors.....	38
10.2 Superposition	38
IV CORRECTION FACTORS.....	41
11 Extensions: correction factors	43
12 Inclination factors	44
12.1 Meyerhof and Brinch Hansen.....	44
12.2 Surcharge fan reduction angle ψ_q	46
12.3 Cohesion fan reduction angle ψ_c	47
12.4 Surcharge inclination factor i_q	49
12.5 Cohesion inclination factor i_c	51

12.6 Soil-weight inclination factor i_γ	54
13 Shape factors	56
13.1 Meyerhof and De Beer	56
13.2 Axisymmetric failure versus plane strain failure.....	56
13.3 Cohesion shape factor s_c	57
13.4 Surcharge shape factor s_q	59
13.5 Soil-weight shape factor s_γ	62
13.6 Superposition of the shape factors	64
14 Eccentric loading.....	65
15 Slope factors	69
15.1 Meyerhof and Vesic	69
15.2 Modern research and German norms.....	70
15.3 Cohesion slope factor λ_c	72
15.4 Soil-weight slope factor λ_γ	73
15.5 Surcharge slope factor λ_q	75
16 Inclined footing factors	78
17 Special footings.....	79
17.1 Perforated footings.....	79
17.2 Shell footings	81
17.3 Footings on layered soil and punching	82
V PILE TIP BEARING CAPACITY	85
18 Pile tip bearing capacity using Meyerhof.....	87
19 Pile tip bearing capacity, CPT and failure mechanism	89
20 Pile tip bearing capacity versus horizontal stress	94
VI APPENDICES	97
21 Mohr-Coulomb and Rankine	99
22 N_c simplification	101
23 Prandtl's publication of 1920.....	103
24 Reissner's publication of 1924	117
25 Literature	131
26 Background of the author.....	135

I Prandtl & Reissner

1 Introduction

The discipline of Soil mechanics and Foundation Engineering is one of the younger basic civil engineering disciplines. It was developed in the beginning of the 20th century. The need for this discipline arose in many countries, often as a result of spectacular accidents such as landslides and foundation failures. The first important contributions to soil mechanics were made by Coulomb, who published an important treatise on the failure of soils in 1776, and to Rankine, who published an article on the possible stress states in soils in 1857. Important pioneering contributions to the development of soil mechanics were made by the Austrian Karl Von Terzaghi. In 1925 he described in his book “*Erdbaumechanik*” how to deal with the influence of the pressures of the pore water on the behaviour of soils. His concept of effective stresses is an essential element of the theory of soil mechanics. Karl emigrated to the United States in 1938. Thereafter he no longer published under his real name “*Von Terzaghi*”, but always as “*Terzaghi*”, no doubt in order to hide his origin due to World War II.



Figure 1-1. Karl Von Terzaghi (Oct. 2, 1883 – Oct. 25, 1963).

The biggest problem for a shallow foundation, just as any other type of foundation, is a failure due to an overestimation of the bearing capacity (see Figure 1-2 and Figure 1-3). This means that the correct prediction of the bearing capacity of the shallow foundation is often the most important part of the design of a civil structure. That is why the publication of Prandtl in 1920, about the hardness of plastic bodies, was a major step in solving the bearing capacity of a shallow foundation. However, it is highly possible that he never realised this, because his solution was not made for civil engineering purposes, but for mechanical purposes.



*Figure 1-2. Overloaded shallow foundation of a group of grain silos
(from Tschebotarioff, 1951).*



*Figure 1-3. Overloaded shallow foundation of a group of grain silos.
Transcona Grain Elevator, Manitoba, Canada, October 18, 1913*

This introduction will be followed by a summary of the life of Ludwig Prandtl, the publisher of the Prandtl-wedge, as well as a summary of the life of Hans Jacob Reissner, who extended this Prandtl-wedge for a surcharge, making this analytical solution more suitable for foundation engineering purposes.

2 Ludwig Prandtl

Details about the life of Ludwig Prandtl can be found on Wikipedia, on the homepage of the Deutschen Zentrum für Luft- und Raumfahrt (DLR), in the book “*Prandtl and the Göttingen School*”, written by Eberhard Bodenschatz and Michael Eckert, and especially in the book “*Ludwig Prandtl, A Biographical Sketch, Remembrances and Documents*”. There is a German original of the latter by Johanna Vogel-Prandtl but also an English translation by V. Vasanta Ram, published by The International Centre for Theoretical Physics Trieste, Italy. The information below was taken from these sources.

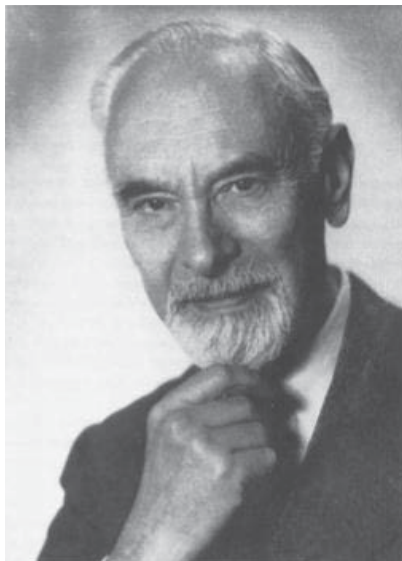


Figure 2-1. Ludwig Prandtl (Feb. 4, 1875 – Aug. 15, 1953)

Ludwig Prandtl was born in Freising, near Munich, Germany, in 1875. When Ludwig Prandtl was born his mother was only 19 years of age, his father 35. His mother suffered from a lengthy illness and, as a result, Ludwig spent more time with his father, a professor of engineering. He entered the Technische Hochschule Munich in 1894. Prandtl passed the final examination in 1898 with the grade "sehr gut" ("very good").

After this, he was offered the job of a “*Hilfsassistent*” by Professor Föppl, which he gladly accepted. This post, with a view to earn a doctor's degree, was assigned for one year only. Professor Föppl helped Prandtl to postpone military conscription by one year. The period when Prandtl worked with August Föppl in his mechanical engineering laboratory can be dated exactly: from October 1, 1898 to November 30, 1899. In this time Prandtl wrote his dissertation entitled: “*Kipp-Erscheinungen, ein Fall von instabilem elastischem Gleichgewicht*” (Lateral torsional buckling: A case of unstable elastic equilibrium). Prandtl was unable to get a doctor's degree with this

dissertation at the Technische Hochschule München (this institution was only given the right to award doctor's degrees in 1900). Instead he submitted his work to the Philosophische Fakultät of the Munich University. The defence took place on January 29, 1900.

In 1901 Prandtl became a professor of fluid mechanics at the technical school in Hannover, now the Technical University Hannover. It was here that he developed many of his most important theories. In 1904 he delivered his first famous paper, "*Fluid Flow in Very Little Friction*", in which he described the boundary layer and its importance for drag and streamlining. This paper also described flow separation as a result of the boundary layer, clearly explaining the concept of stall for the first time. The effect of the paper was so great that Prandtl became director of the Institute for Technical Physics at the University of Göttingen later that year.



Figure 2-2. Ludwig Prandtl with his fluid test channel, 1904.

Prandtl became close to the family of professor Föppl. At Easter 1909, Prandtl asked Gertrud Föppl to marry him. It was agreed that Prandtl would remain in the Catholic Church but Gertrud's Protestant ancestry would prescribe the formalities for the wedding. Thus, on September 11, 1909, Ludwig Prandtl and Gertrud Föppl married in a Protestant Church in Munich. The wedding festivities were held at the Föppl's house. Ludwig and Gertrud had two daughters, Hildegard born in 1914, and Johanna born in 1917.

During World War I, Prandtl continued working as director of the Institute for Technical Physics at the University of Göttingen. This large aerodynamics laboratory was created to support the German army and navy. Several of Prandtl's assistants who had been drafted for military duties were brought back to Göttingen to assist in this matter, which was considered of major importance for the war effort. In 1915, another wind tunnel project was started and completed in 1917. This more powerful, 300 horse-power, tunnel gave Prandtl more scope for research.

Prandtl and his student Theodor Meyer developed the first theories of supersonic shock waves and flow in 1908. The Prandtl-Meyer expansion fans allowed for the construction of supersonic wind tunnels. He had little time to work on the problem further until the 1920s, when he worked with Adolf Busemann and created a method for designing a supersonic nozzle in 1929. Today, all supersonic wind tunnels and rocket nozzles are designed using the same method. However, a full development of supersonics would have to wait for the work of Theodore von Kármán, a student of Prandtl at Göttingen.

In 1922, together with Richard Von Mises, Prandtl founded the GAMM (the International Association of Applied Mathematics and Mechanics) and was its chairman from 1922 until 1933.

Prandtl worked at Göttingen until he died on August 15, 1953. His work in fluid dynamics is still used today in many areas of aerodynamics and chemical engineering. He is often referred to as the father of modern aerodynamics.

The crater Prandtl on the far side of the Moon is named in his honour.

The Ludwig-Prandtl-Ring is awarded by the Deutsche Gesellschaft für Luft- und Raumfahrt (German Aerospace Association) in his honour for outstanding contributions in the field of aerospace engineering.



*Figure 2-3. Ludwig Prandtl at his water tunnel in the mid to late 1930s
(Reproduction from the original photograph DLR: FS-258).*

3 Hans Jacob Reissner

Information about the life of Hans Jacob can be obtained from Wikipedia or from the library of the University of California, San Diego. The information below is a summary from these two sources.



Figure 3-1. Josefine und Hans Jacob Reissner.

Hans Jacob was born on January 18, 1874, in Berlin, Germany. He earned a degree in civil engineering from Berlin's Technische Hochschule in 1897, and then spent a year in the United States working as a structural draftsman. Reissner returned to Germany to study physics with Max Planck at Berlin University. In 1900 he changed direction and attended the Technische Hochschule, where he studied under Heinrich Mueller-Breslau and completed one of the first engineering doctorates in 1902. His dissertation was on vibrations of framed structures. Reissner joined the faculty at Berlin's Technische Hochschule, but he also worked on outside projects, including structural analysis for Graf (Count) Von Zeppelin. In 1904, he was awarded a fellowship to study the use of iron in construction in the United States of America.

In 1906, Reissner returned to Germany and was appointed professor of mechanics at the Technische Hochschule in Aachen. Until this time, his research had dealt with topics at the intersections of mechanics and physics, but his attention now focused upon the new field of aviation.

On June 6, 1906, he married Josefine Reichenberger. They had four children; Max Erich (Eric Reissner), Edgar Wilhelm, Dorothea Gertrud (Thea) and Eva Sabine.

By 1908, Reissner was familiar enough with the basic areas of aircraft stability, control and propulsion to deliver a seminal paper published as "*Wissenschaftliche Fragen aus der Flugtechnik*" (Scientific Aerospace Questions), the first of many articles on these topics. Together with Hugo Junkers, who also worked at the faculty in Aachen, Reissner designed and constructed the first successful all-metal and tail-first airplane, the "*Ente*" (Duck). He also worked for Ferdinand Graf Von Zeppelin, during this time.



Figure 3-2. Tail-first airplane, the "*Ente*".

In 1913, after seven years at the Rheinisch-Westfälische Technische Hochschule Aachen (Aachen University of Technology), Reissner was invited to return to Berlin's Technische Hochschule as professor of mathematics in the civil engineering department. During World War I he was responsible for the structural analysis of the Staaken four-engine bomber and designed the first controllable-pitch propellers for this aircraft. He was awarded the Iron Cross for civilians for his work.

In 1929 he started to cooperate with Moritz Straus, the owner of both Argus-Werke and Horch. When Reissner was forced to retire in 1935 under the Nazi-Regime because of his Jewish background, he became an advisor of Argus Motoren Gesellschaft.

When Straus was forced to give the company Argus-Werke away in 1938 due to his Jewish background and the Aryansation, Reissner emigrated to the United States. He first taught at the Illinois Institute of Technology (1938-1944) and then, until his retirement, at the Polytechnic Institute of Brooklyn (1944-1954). For his seventy-fifth birthday in 1949 he was honoured with the presentation of the collection: The Reissner Anniversary Volume, at a dinner in New York. Reissner retired from professional life in 1954 and died in 1967. Reissner's son Eric became Professor Mechanical Engineering at the Massachusetts Institute of Technology.

II Original Publications

4 Prandtl's publication of 1920

4.1 Introduction

The publication of Prandtl in 1920 is called “*Über die Härte plastischer Körper*”, or in English “About the hardness of plastic bodies”. It was published in the journal *Nachrichten der Gesellschaft der Wissenschaften zu Göttingen, Mathematisch-physikalischen Klasse*, on page 74–85.

The publication can also be found in the appendices of this book (see Chapter 23), with thanks to the Niedersächsische Staats- und Universitätsbibliothek Göttingen (SUB), Georg-August-Universität Göttingen, Germany.

The title of the publication is in itself interesting, because “*The hardness of plastic bodies*”, does not suggest that a principal problem in shallow foundation engineering had been solved. In fact Prandtl was not a geotechnical engineer, not even a civil engineer.

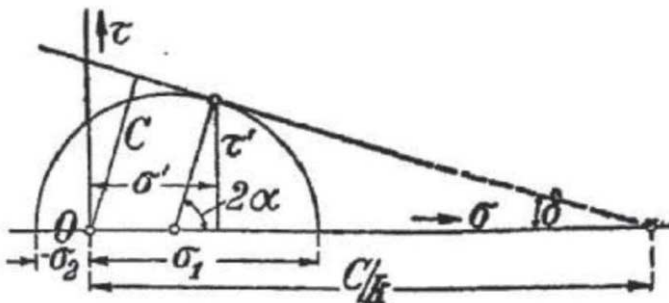
This explains why the publication of Prandtl did not refer to geotechnical solutions, which are well-known in the geotechnical world. For example, the analytical solution for the vertical stresses below a strip footing, made by Flamant in 1892 or the solution for the vertical stresses below a circular footing by Boussinesq in 1885. From laboratory tests it is known that these analytical solutions are very accurate (Türedi and Örnek, 2016).

The explanation of the title is given at the beginning of the publication: “*One owes Heinrich Hertz a theory about the contact of a solid elastic body*”. In fact, in 1881 Hertz solved the elastic, but non-linear, force-displacement relation between two balls or a ball and a flat surface. This was a major step for mechanical engineers, for example for checking if a ball bearing will be overloaded and to what extent plasticity would occur.

The publication of Prandtl was meant to find out at which load, full plasticity would be reached and, an object could be fully pushed into a solid body.

It is clear from the article that the author is not a geotechnical engineer, but a mechanical engineer, because it is written partially with the idea that (see the first page, page 74): “*the biggest shear stresses have a constant value C.....and the difference between the smallest and largest stress should be constant = 2C*”.

This is the case for steel since for steel the friction angle $\phi = 0$, but for soils this is not correct, because a part of the shear strength comes from the friction angle.



Figur 2.

Figure 4-1. Mohr's circle with Coulomb failure envelope.

In the article, for the friction angle, the parameter δ is used, instead of the parameter ϕ , also the parameter k is used, instead of $\sin \delta$ and the parameter C is used for the cohesion instead of the parameter c .

There are also two other remarkable points, see Figure 4-1.

First, the Coulomb failure envelope is drawn for geotechnical engineers as a mirror image, because in mechanical engineering tension is positive, while in geotechnical engineering pressure is positive.

Second, the cohesion is not drawn vertically as it should be, but perpendicularly to the Coulomb failure envelope. These two points explain why in the final solution (Equation 13b, page 84) there is a $-C/k$, which is a mistake; it should be only a c .

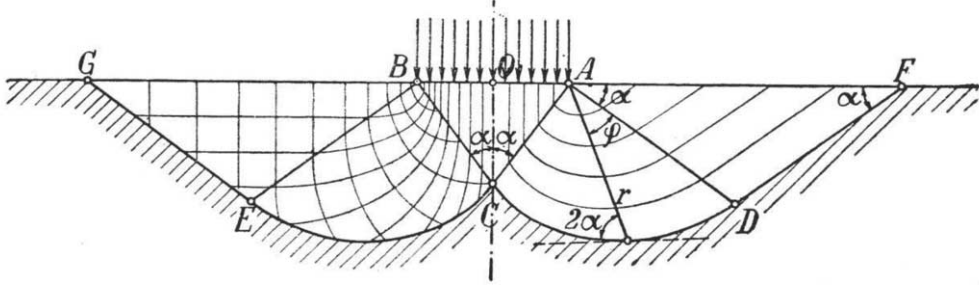
4.2 Prandtl-wedge

Prandtl was the first to publish the failure mechanism of the solid body due to a strip load, consisting of three different types of area. This failure mechanism is today known as “The Prandtl-wedge”

Unfortunately the article is very direct; final solutions are often given without much explication. For example the most important part of the publication, the “discovery” of the Prandtl-wedge is discussed in only a few lines, in a style something like;

“There must be an area below the strip load with the principal direction of the largest stress downwards and an area below the adjacent surface of the strip load, where the highest principal stress is horizontal and the lowest principal stress points downwards. These areas have shear surfaces with an angle of $\alpha = 45^\circ - \phi/2$ in comparison to the highest principal stress”.

And then the author simply concludes on page 76: “*Closer examination shows that the solution is found by the zoning depicted in Figure 1*”, which is followed by the famous “Prandtl-wedge” shown in Figure 4-2.



Figur 1.

Figure 4-2. The Prandtl-wedge.

The figure shows the sliding very clearly, both to the left and the right, while using the left side to show the directions of the principal stresses in the soil and the right side to show the shear lines which make an angle of $\alpha = 45^\circ - \phi/2$ in comparison to the highest principal stress.

A bit further the author says:

“Between the first and the two last triangles there are sector shaped parts ACD and BCE”, because “the curves CD and CE” are a part of “a system of shear lines” which cross “the radii leaving from A and B”, with “a constant angle 2α ”, from which “it follows directly that the shear lines are logarithmic spirals”.

How the final solution (Equation 13b, page 80) is found is not given in Prandtl's paper. It only says on this page: “...in this way, after simple calculations,...”.

Therefore a complete explanation of this solution will be given in Chapter 8.

4.3 Prandtl-wedge, also discovered by Prandtl?

In the past it was very common that the head of a research group would receive most if not all the credit for the output of his group. As an example, all astronomical objects discovered by Pierre Méchain, are not named after him, but after Charles Messier, “simply” because Méchain was hired by Messier.

The Prandtl Crater on the Moon is named after Prandtl, but was certainly not discovered by him. In a similar way it is not automatically clear if the Prandtl-wedge was really discovered by Prandtl himself, or by someone who was appointed by Prandtl. To answer this, some points have to be considered.

First, it is remarkable that the “Prandtl-wedge” article of 1920, which deals with solid mechanics, was published solely by Prandtl, a former professor in fluid mechanics, fully dedicated at that time to supersonic wind tunnels and rocket nozzles, but with scientific staff working, not only on fluid mechanics, but also on solid mechanics.

Second, another interesting point can be derived from the list of all publications of Prandtl, which can be found in the book:

Ludwig Prandtl Gesammelte Abhandlungen
Zur angewandten Mechanik, Hydro- und Aerodynamik
Herausgegeben von Walter Tollmein – Hermann Schlichting - Henry Görtler
Schriftleitung F.W. Riegels
Erster Teil (S.1-574) 1961 Springer-Verlag Berlin Heidelberg GmbH

Figure 4-3 has been made based on this list. It shows the number of publications Prandtl wrote during his career both as a single author and together with a co-author. It is striking that Prandtl, whilst working as director of the Institute for Technical Physics at the University of Göttingen and as chairman of the International Association of Applied Mathematics and Mechanics, not only still managed to publish so many articles per year but also most of them completely alone.

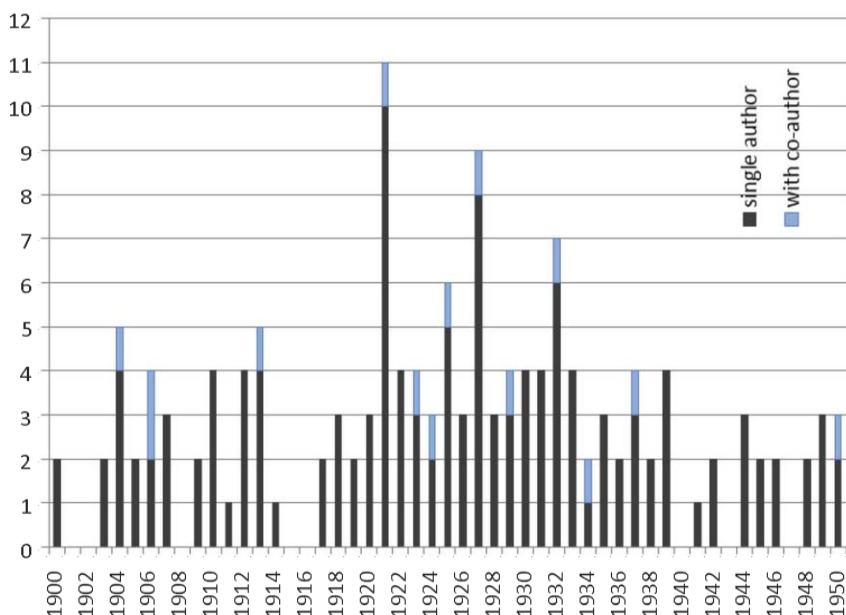


Figure 4-3. Publications of Prandtl, with and without co-author.

Third, the few articles which Prandtl did not publish alone, were almost all co-authored by his closest research collaborators, like the famous Albert Betz and Max Munk. Betz later progressed quickly in his career; in 1926 he was appointed professor at Göttingen and in 1936 he even replaced Prandtl under the Luftwaffe command as director of the Aerodynamische Versuchsanstalt (AVA, aerodynamics laboratory). Which raises the question; why are there not more co-authorships with the other colleagues?

Fourth, all scientists working for Prandtl at that time, had been saved from the trenches of the First World War by being declared indispensable by Prandtl. They would have been glad to escape the war and to do research “under the guidance and responsibility of the director”. It was certainly not a time to protest if your name was

missing on a publication. Even today some professors present the scientific work of their research assistants at conferences.

Therefore, the possibility cannot be excluded that the solution of the Prandtl-wedge was not actually discovered by Prandtl himself, but by one of his research collaborators, working on solid mechanics, unlike Prandtl himself. In this case, whoever really discovered the famous “Prandtl-wedge”, will most likely remain forever unknown.

5 Reissner's publication of 1924

5.1 Introduction

The publication of Reissner in 1924 is called “*Zum Erddruckproblem*”, or in English “Concerning the earth-pressure problem”. It was published in the International proceedings of the first International Congress of Applied Mechanics, Delft, the Netherlands, pages 295-311.

A part of this publication can also be found in the appendices of this book (see Chapter 24).

The title is rather general because several topics are discussed in the publication. Remarkably enough, of the 17 pages of the publication, only one page, page 307, discusses the effect of the surcharge on the bearing capacity.

5.2 Effect of the surcharge

In fact the solution for the surcharge is far simpler than the solution for the cohesion published by Prandtl, 4 years before Reissner. The simple reason why Prandtl never thought of solving the effect of the surcharge is that the effect of the surcharge is typically a civil engineering problem and Reissner was a civil engineer and Prandtl a mechanical engineer.

At the bottom of page 307, in only one or two lines, Reissner gives a solution for an inclined (unsymmetrical) load, which is incorrect, as can be seen from the solutions given in Chapter 12. This is directly followed by a solution, in only one or two lines, for a vertical (symmetrical) load, supported by the figure below.

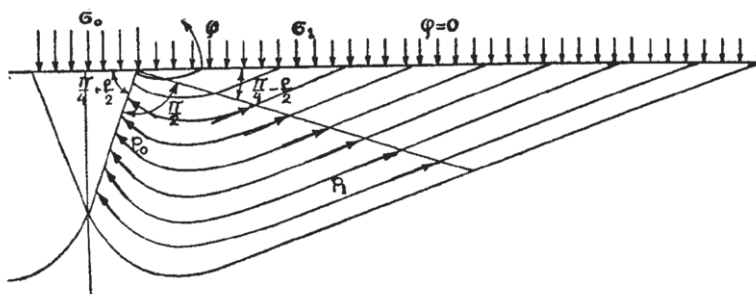


Abb. 6.

Figure 5-1. Prandtl-wedge according to Reissner.

The middle part of the Prandtl-wedge in Reissner's figure does not really look like a logarithmic spiral, but this was more a drawing problem than a scientific problem. Having a logarithmic spiral is crucial, because this is the only shape where the effects of the frictional part of the shear forces, acting along this middle part, are zero. This will be discussed in Chapter 7.

III Bearing capacity factors

6 Prandtl-wedge

The publication of Prandtl in 1920 gives an analytical solution for the bearing capacity of a strip foundation on a soil, loaded with a limit pressure, p , causing kinematic failure of the weightless infinite half-space underneath. The strength of the half-space is given by the angle of internal friction, ϕ , and the cohesion, c . The solution was extended by Reissner in 1924 with a surrounding surcharge, q . The article of Prandtl subdivided the sliding soil part into three zones (see Figure 6-1):

1. Zone 1: A triangular zone below the strip load. Since there is no friction on the ground surface, the directions of the principal stresses are horizontal and vertical; the largest principal stress is in the vertical direction.
2. Zone 2: A wedge with the shape of a logarithmic spiral, where the principal stresses rotate through 90° from Zone 1 to Zone 3. The pitch of the logarithmic spiral equals the angle of internal friction; ϕ , creating a smooth transition between Zone 1 and Zone 3 and also creating a zero frictional moment on the sliding surface of this wedge, see Chapter 7.1.
3. Zone 3: A triangular zone adjacent to the strip load. Since there is no friction on the surface of the ground, the directions of principal stress are horizontal and vertical; the largest principal stress is in the horizontal direction.

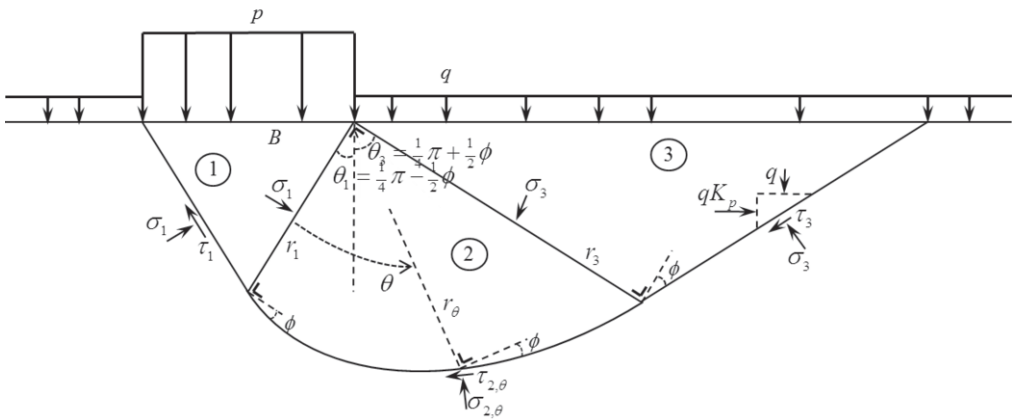


Figure 6-1. The Prandtl-wedge.

According to the Mohr-Coulomb failure criterion (see Appendix Chapter 21) the angles in the triangular zones are defined as:

$$\theta_1 = \frac{1}{4}\pi - \frac{1}{2}\phi \quad \text{and} \quad \theta_3 = \frac{1}{4}\pi + \frac{1}{2}\phi \quad \text{so that} \quad \theta_1 + \theta_3 = \frac{1}{2}\pi, \quad (6.1)$$

or:

$$\theta_1 = 45^\circ - \frac{1}{2}\phi \quad \text{and} \quad \theta_3 = 45^\circ + \frac{1}{2}\phi \quad \text{so that} \quad \theta_1 + \theta_3 = 90^\circ. \quad (6.2)$$

This means that zone 2 has a top angle of 90 degrees.

The fact that the angle between active and passive failure is an angle of $\theta_1 + \theta_3 = 90^\circ$ can also be shown with a clay sample with a small aluminium plate as retaining wall, (see Figure 6-2) which was gravity loaded in a top loaded centrifugal clothes dryer or laundry washing machine.

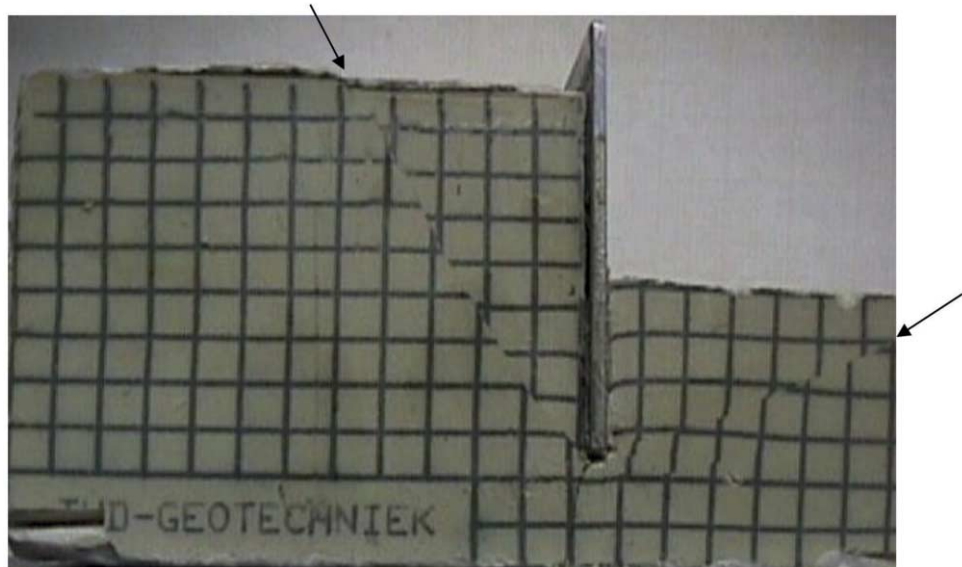


Figure 6-2. Active (left) and passive (right) failure plane in a clay sample.

The length of the legs of both triangles (Zone 1 and Zone 3 in Figure 6-1) can be determined from the width of the load strip (B) and the size and shape of the logarithmic spiral:

$$r(\theta) = r_1 \cdot e^{\theta \tan \phi}, \quad (6.3)$$

giving:

$$\frac{r_3}{r_1} = e^{\frac{1}{2}\pi \tan \phi}. \quad (6.4)$$

The shape of the failure mechanism has been validated by many researchers, first with centrifuge tests (see Figure 6-3) and numerous laboratory tests (see Figure 6-4), and later also with many numerical (Finite Element) calculations.

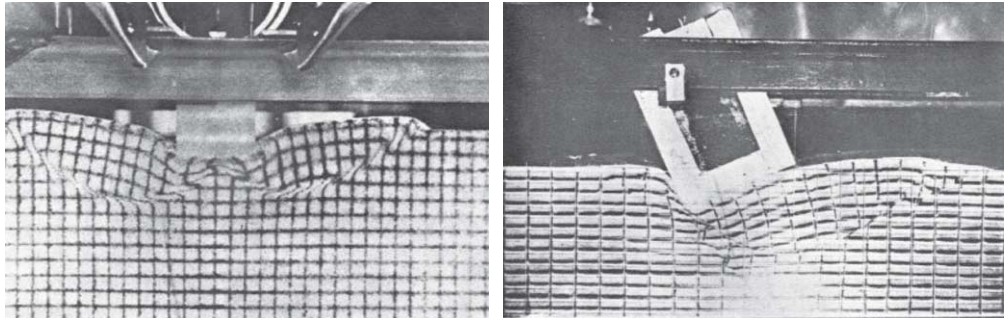


Figure 6-3. Failure planes in sand for centric loading (left: Selig and McKee, 1961) and eccentric loading (right: Jumikis, 1956).

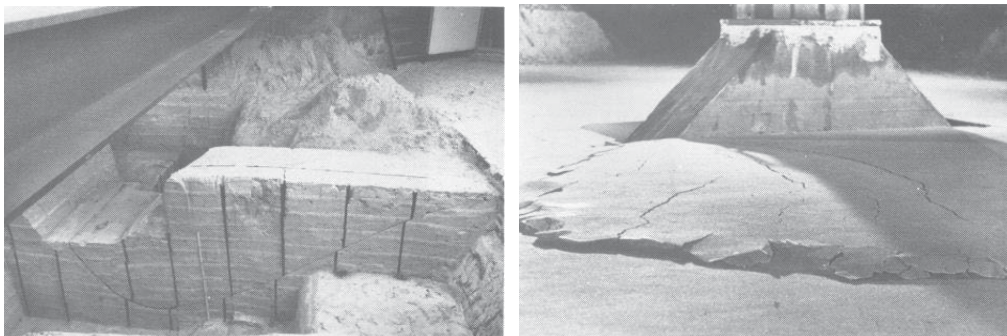


Figure 6-4. Failure planes in sand (Muhs and Weiß, 1972).

The rotation of the principal stress directions over 90 degrees in the logarithmic spiral zone, which means a 180 degree rotation of the pole of a Mohr circle, causes an interesting development of the poles of the Mohr-circles in this zone, see Figure 6-5. This figure, with the pole trail of the logarithmic spiral zone, has been published by (Gerard) De Josselin De Jong in 1959. Some numbers and circles have been added here to make the figure clearer. De Josselin De Jong developed a graphical method to find this pole trail.

It was Prandtl who published the bearing capacity due to the cohesion in 1920 and Reissner who published the bearing capacity due to the surcharge in 1924. These solutions were extended by Keverling Buisman (1940) for the soil weight, γ . Terzaghi (1943) was the first to write the bearing capacity with this extension as:

$$p = cN_c + qN_q + \frac{1}{2}\gamma BN_\gamma \quad (6.5)$$

The three bearing capacity factors N_c , N_q , N_γ , will be discussed in the following chapters. Since the surcharge bearing capacity factor N_q from Reissner is easier to solve and explain than the cohesion bearing capacity factor N_c from Prandtl, the surcharge factor will be discussed first.

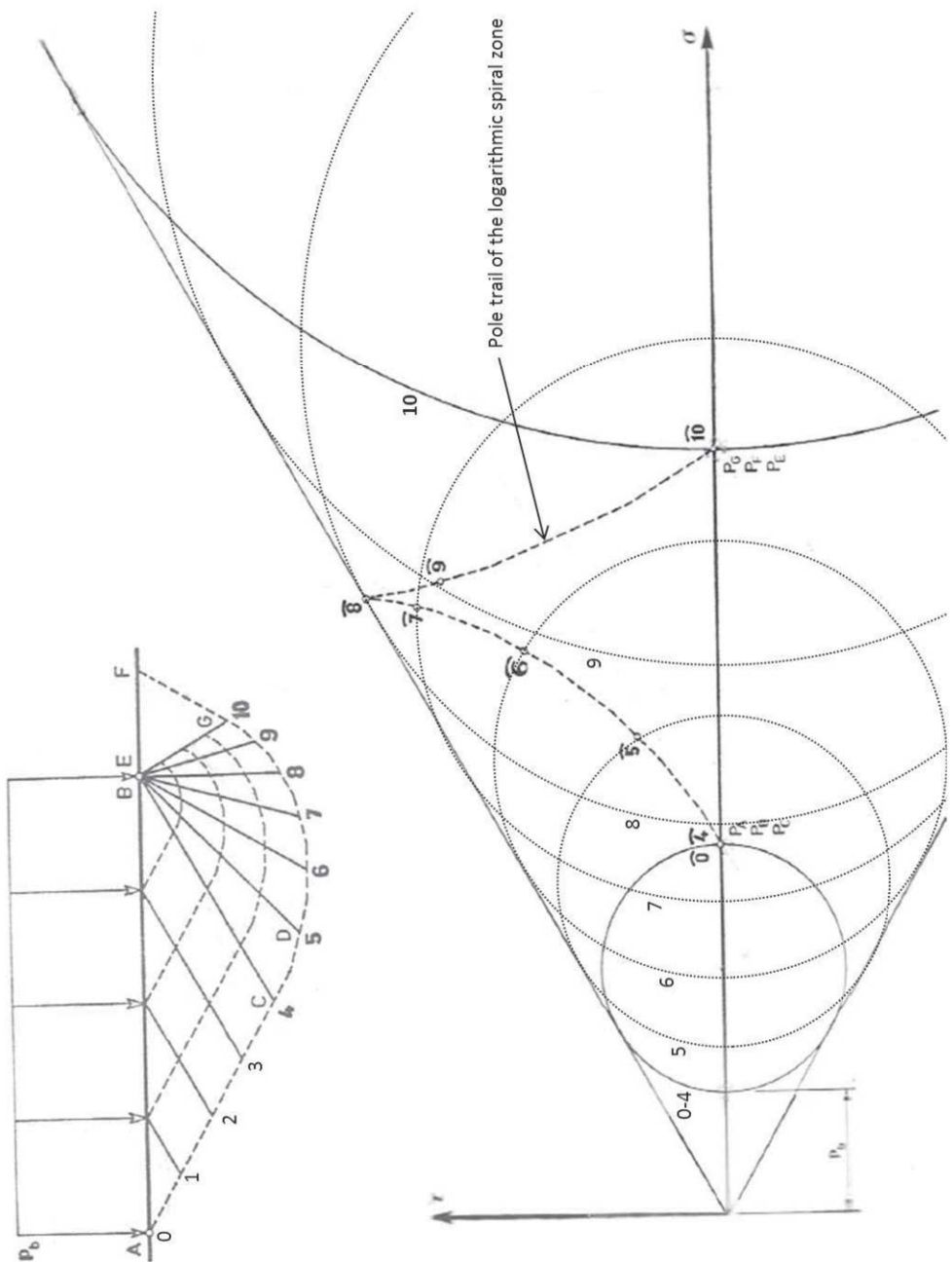


Figure 6-5. The pole trail of the Prandtl-wedge.

7 Surcharge bearing capacity factor N_q

7.1 Analytical solution

In order to solve the surcharge bearing capacity factor N_q , simply the stresses can be followed along the 3 zones, for a case in which there is no cohesion and no soil weight ($c = 0, \gamma = 0$).

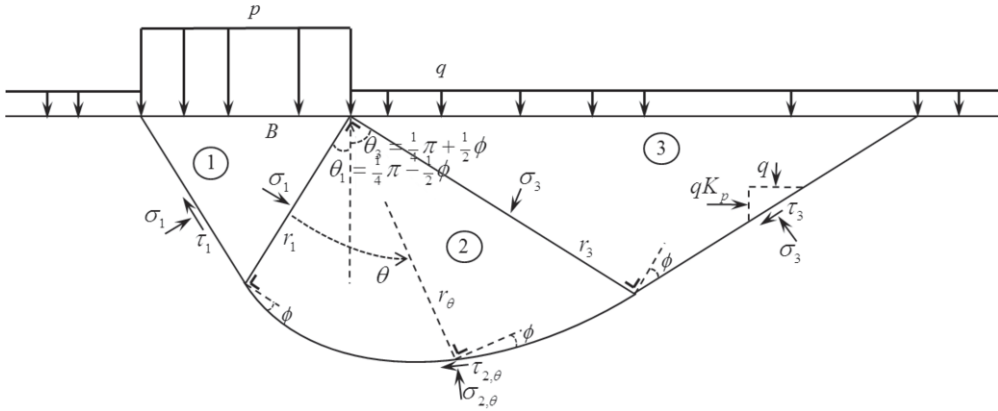


Figure 7-1. The Prandtl-wedge (copy of Figure 6-1).

Zone 3

For Zone 3 the vertical stress, at all points within the zone, is given by the surcharge ($\sigma_v = q = \sigma_{\min}$), and the horizontal stress is given by the Mohr-Coulomb criterion as follows (see Chapter 21):

$$\sigma_h = \sigma_{\max} = \sigma_{\min} K_p \quad \text{with} \quad K_p = \frac{1 + \sin \phi}{1 - \sin \phi} = \tan^2 \theta_3 \quad (7.1)$$

The normal stress, σ_3 , is found by using the principle of force equilibrium in the direction of σ_3 :

$$\frac{\sigma_3}{q} = K_p \cdot \cos^2 \theta_3 + \sin^2 \theta_3 = 2 \sin^2 \theta_3. \quad (7.2)$$

The shear stress, τ_3 , is simply found by using the Coulomb criterion (without cohesion):

$$\frac{\tau_3}{q} = \frac{\sigma_3}{q} \cdot \tan \phi. \quad (7.3)$$

Zone 2

The shape of the outside shear line of Zone 2 is a logarithmic spiral with a pitch of exactly ϕ . The important point of this is that along this outside, the additional moment

ΔM_θ created by the normal $\sigma_{2,i}$ and shear forces $\tau_{2,i}$ is for this pitch, for every angle θ_i , exactly zero during Mohr-Coulomb failure:

$$\Delta M_\theta = \int \frac{1}{2} \cdot r_{2,i}^2 (\tau_{2,i} \cdot \cos \phi - \sigma_{2,i} \cdot \sin \phi) d\theta_i = 0 \quad \text{because} \quad \tau_{2,i} = \sigma_{2,i} \cdot \tan \phi. \quad (7.4)$$

This means that a moment equilibrium of Zone 2 depends only on the loads coming from Zone 1 and Zone 3, so:

$$\sum M_\theta = 0 \Rightarrow \sigma_1 \cdot \frac{1}{2} \cdot r_1^2 = \sigma_3 \cdot \frac{1}{2} \cdot r_3^2, \quad (7.5)$$

or:

$$\frac{\sigma_1}{\sigma_3} = \frac{\tau_1}{\tau_3} = \frac{r_3^2}{r_1^2} = \left(e^{\frac{1}{2}\pi \tan \phi} \right)^2 = e^{\pi \tan \phi} \quad \text{and} \quad \frac{\tau_1}{q} = \frac{\sigma_1}{q} \cdot \tan \phi. \quad (7.6)$$

Zone 1

The horizontal stress σ_h in Zone 1 can be found in the same way as the vertical stress σ_v (or q) in Zone 3:

$$\frac{\sigma_h}{\sigma_1} = \frac{1}{2 \sin^2 \theta_3}. \quad (7.7)$$

The ultimate vertical load or stress p is simply the horizontal stress times the passive earth pressure coefficient, so:

$$\frac{p}{\sigma_h} = K_p. \quad (7.8)$$

Zone 1+2+3

By adding the effects of the three zones, which means by multiplying the previous steps, the surcharge bearing capacity coefficient N_q can be found:

$$\begin{aligned} N_q &= \frac{p}{q}, \\ &= \frac{p}{\sigma_h} \cdot \frac{\sigma_h}{\sigma_1} \cdot \frac{\sigma_1}{\sigma_3} \cdot \frac{\sigma_3}{q}, \\ &= K_p \cdot \frac{1}{2 \sin^2 \theta_3} \cdot e^{\pi \tan \phi} \cdot 2 \sin^2 \theta_3, \\ &= K_p \cdot e^{\pi \tan \phi}. \end{aligned} \quad (7.9)$$

7.2 Numerical solution

The analytical solution published by Reissner can of course be checked today with finite element calculations. In this study all solutions will be checked with finite element calculations using the software Plaxis 2D for a (bi-linear) Mohr-Coulomb (c, ϕ) soil model without hardening, softening, or volume change ($\psi = 0$) during

failure. Several researchers have worked on this numerical validation, but their publications often show one or more of the following mistakes:

- Using inaccurate numerical tools, for example the limit-equilibrium analysis method, instead of the finite element method.
- Using softening (in Plaxis there is a standard “tension cut off”-procedure which must be switched off).
- Using an extreme volume change during failure, for example by selecting an associated flow rule ($\psi = \phi$).

Plaxis produces incremental displacement plots during failure, which indicate the failure mechanism. For low friction angles, the failure mechanism is almost the same as the Prandtl-wedge failure mechanism, which is the basis of the analytical solution. For high friction angles though, the failure mechanism looks completely different, see Figure 7-2.

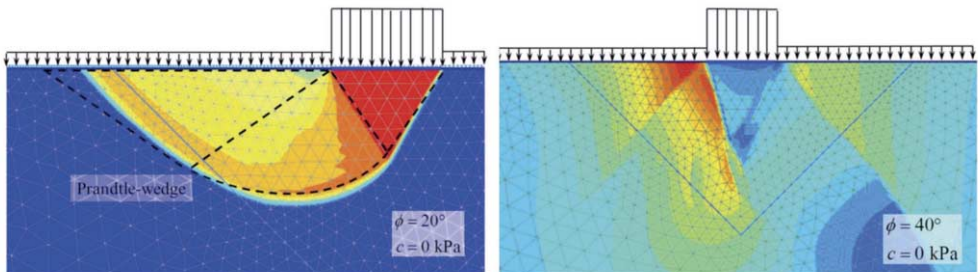


Figure 7-2. Failure mechanism; left: low friction angle; right: high friction angle.

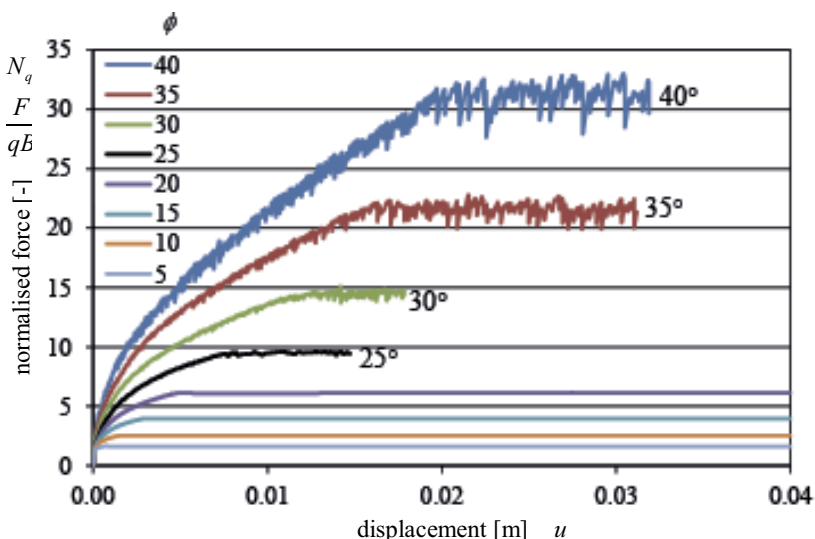


Figure 7-3. Normalised force versus displacement for different friction angles.

This change in failure mechanism has consequences; the force versus displacement plot is rather smooth for low friction angles, but becomes very rough for higher friction angles, see Figure 7-3. This is a sign that constantly new shear failure planes are found in the calculation, depending on the internal redistribution of stresses.

For the series of different friction angles of Figure 7-3, the maximum normalised force is the same as the surcharge bearing capacity. These factors have been plotted in Figure 7-4. For the Finite Element Modelling (FEM) two different options have been used; both stress controlled and displacement controlled. The two options give as expected (almost) the same results.

Remarkably, the analytical solution of Reissner gives values which are too high, especially for higher friction angles.

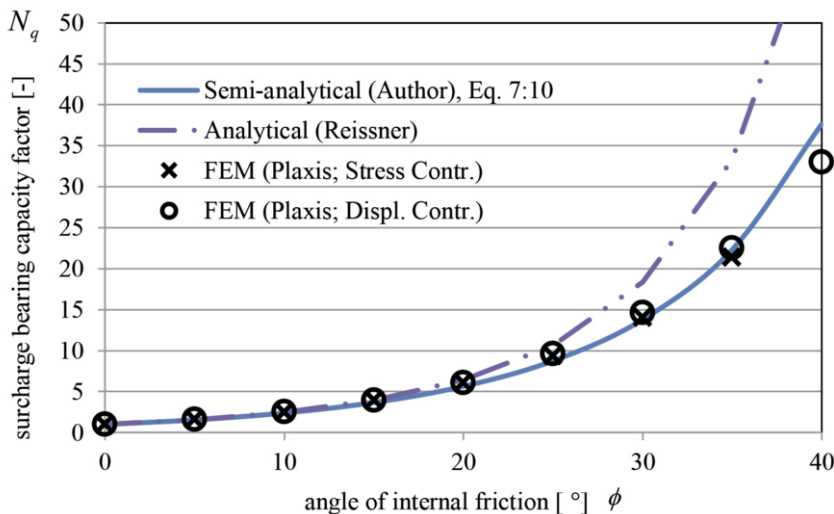


Figure 7-4. Surcharge bearing capacity factors: Reissner versus FEM.

The semi-analytical line in the figure describes the surcharge bearing capacity factors much better, and can be written as (see Van Baars, 2016b, 2017a, 2018a):

$$N_q = \cos^2 \phi \cdot K_p \cdot e^{\pi \tan \phi}. \quad (7.10)$$

Loukidis et al (2008) already noticed that non-dilatant (non-associated) soil is 15% - 30% weaker than associated soil ($\psi = \phi$), and has a rougher failure pattern.

The difference between the analytical solution (Equation 7.9) and the numerical results (Equation 7.10) was explained by Knudsen and Mortensen (2016): The higher the friction angle, the wider the logarithmic spiral of the Prandtl-wedge and the more the stresses reduce in this wedge during failure. So, the analytical formulas are only kinematically admissible for associated flow ($\psi = \phi$).

The problem of associated soil is of course, that such a high dilatancy angle is by far unrealistic for natural soils. In addition, this means that calculating the bearing capacity factor based on the analytical solutions is also unrealistic for higher friction angles.

8 Cohesion bearing capacity factor N_c

8.1 Analytical solution

In order to solve the cohesion bearing capacity factor N_c , simply the stresses have to be followed along the 3 zones, for a case in which there is no surcharge and no soil weight ($q = 0, \gamma = 0$). In the solution below, the load p_α will be inclined, so that this solution can also be used later for solving the inclination factor.

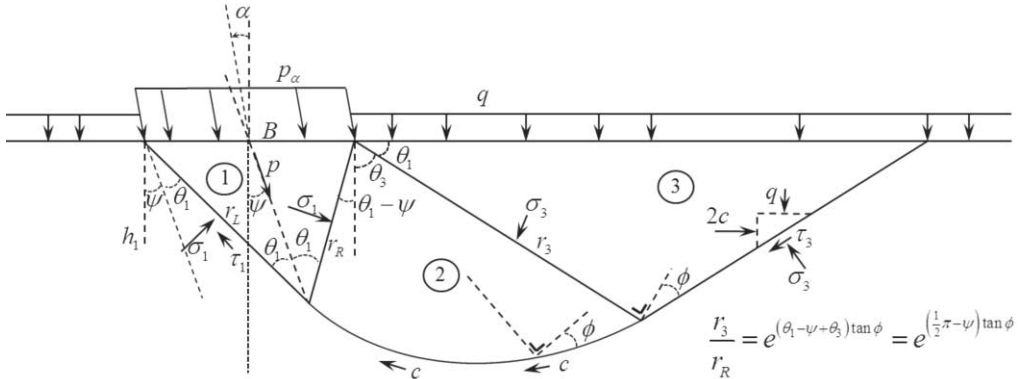


Figure 8-1. Prandtl-wedge for inclined loads.

The load inclination angle α is causing a rotation of Zone 1 and a reduction of the fan (Zone 2) with an angle ψ . The load inclination angle α and the fan reduction angle ψ are zero for non-inclined, or vertical, loads.

Zone 3

For Zone 3 the shear force follows from the Mohr-Coulomb failure criterion:

$$\tau_3 = c + \sigma_3 \cdot \tan \phi. \quad (8.1)$$

Vertical force equilibrium yields:

$$\sum F_v = 0 \Rightarrow \sin \theta_1 \cdot \tau_3 = \cos \theta_1 \cdot \sigma_3, \quad (8.2)$$

or with the first equation implemented in the second:

$$\sigma_3 = c \cdot \frac{\tan \theta_1}{1 - \tan \theta_1 \cdot \tan \phi}. \quad (8.3)$$

Zone 2

Chapter 7 already showed that for Zone 2, which has the shape of a logarithmic spiral, the additional moment ΔM_θ , created by the normal force $\sigma_{2,i}$ and the corresponding frictional shear forces $\tau_{2,i}$, is zero during Mohr-Coulomb failure. So along the outside only the cohesion needs to be taken into account for the moment equilibrium:

$$\sum M_\theta = 0 \Rightarrow \sigma_1 \cdot \frac{1}{2} \cdot r_1^2 = \sigma_3 \cdot \frac{1}{2} \cdot r_3^2 + \int_{\theta_i=0}^{\theta_3+\theta_1-\psi} r_i^2 \cdot \frac{1}{\cos \phi} \cdot c \cdot \cos \phi \cdot d\theta_i, \quad (8.4)$$

or:

$$\begin{aligned}\sigma_1 &= \sigma_3 \cdot \frac{r_3^2}{r_1^2} + 2c \int_{\theta_i=0}^{\theta_3+\theta_1-\psi} e^{2\theta_i \cdot \tan \phi} d\theta_i \\ \sigma_1 &= \sigma_3 \cdot e^{2(\theta_3+\theta_1-\psi) \tan \phi} + 2c \cdot \left[\frac{1}{2 \tan \phi} \cdot e^{2\theta_i \cdot \tan \phi} \right]_0^{\pi-\psi} \\ \sigma_1 &= \sigma_3 \cdot e^{(\pi-2\psi) \tan \phi} + c \cdot \cot \phi \cdot (e^{(\pi-2\psi) \tan \phi} - 1)\end{aligned}\quad (8.5)$$

Zone 1

The shear force along the triangle shaped Zone 1 will be according Mohr-Coulomb:

$$\tau_1 = c + \sigma_1 \cdot \tan \phi. \quad (8.6)$$

In fact, independently from the rotation angle ψ , a force equilibrium in the direction of ψ will result in the following equation of the main principal stress p :

$$\begin{aligned}\sum F_\psi &= 0 \Rightarrow p \cdot \sin \theta_1 = \cos \theta_1 \cdot \tau_1 + \sin \theta_1 \cdot \sigma_1, \\ &\Rightarrow p = c \cdot \cot \theta_1 + \sigma_1 \cdot (1 + \cot \theta_1 \cdot \tan \phi).\end{aligned}\quad (8.7)$$

For finding the size of the load p_α , or its vertical and horizontal components, the fan reduction angle ψ has to be solved first.

Zone 1+2+3

By implementing the equations of the three zones, the following equation is found:

$$\frac{p}{c} = \cot \theta_1 + \left\{ \left(\frac{\tan \theta_1}{1 - \tan \theta_1 \cdot \tan \phi} \right) \cdot e^{(\pi-2\psi) \tan \phi} + \cot \phi \cdot (e^{(\pi-2\psi) \tan \phi} - 1) \right\} \cdot (1 + \cot \theta_1 \cdot \tan \phi). \quad (8.8)$$

This equation can be used later for finding the corresponding inclination factor, but first the solution for a vertical load $p_v = p (\alpha = \psi = 0)$ will be derived:

$$\begin{aligned}N_c &= \frac{p(\psi=0)}{c}, \\ &= \cot \theta_1 + \left\{ \left(\frac{\tan \theta_1}{1 - \tan \theta_1 \cdot \tan \phi} \right) \cdot e^{\pi \tan \phi} + \cot \phi \cdot (e^{\pi \tan \phi} - 1) \right\} \cdot (1 + \cot \theta_1 \cdot \tan \phi).\end{aligned}\quad (8.9)$$

From Appendix Chapter 0 it follows after a long derivation that this equation is exactly the same as:

$$N_c = (N_q - 1) \cot \phi \quad \text{with: } N_q = K_p \cdot e^{\pi \tan \phi}. \quad (8.10)$$

This is the same solution as in the publication of Prandtl, but in the publication of Prandtl most of this derivation is missing; the reader can only find in the publication the words “*after simple calculations*”.

8.2 Numerical solution

The analytical solution published by Prandtl has been checked with finite element calculations performed with Plaxis 2D. The mesh has been made so fine that no

differences appear in the results anymore. In order to be certain that the calculations would not stop too soon, the Arc-length control function has been switched off, the over-relaxation-factor has been put to 1.0, the maximum unloading steps has been set high and the maximum load fraction per step low.

The incremental displacement plots during failure indicate the failure mechanism. For low friction angles the failure mechanism looks very much like the Prandtl-wedge failure mechanism, which is the basis of the analytical solution. For high friction angles though, the failure mechanism is very different and looks like a punching failure, see Figure 8-2.

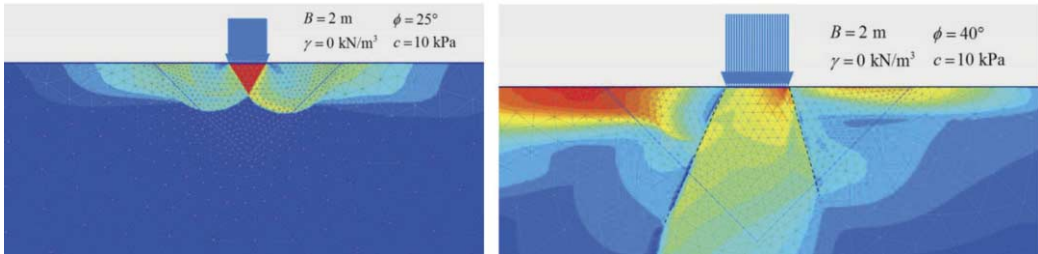


Figure 8-2. Failure mechanism; left: low friction angle; right: high friction angle.

This change in failure mechanism has consequences; the force versus displacement plot is rather smooth for low friction angles, but becomes very rough for higher friction angles, see Figure 8-3. This is a sign that constantly new failure planes are found in the calculation, depending on the internal redistribution of the stresses.

For a series of different friction angles, the maximum value of the normalised force, or the surcharge bearing capacity has been plotted, see Figure 8-4. For the Finite Element Modelling (FEM) both stress controlled and displacement controlled calculations have been used. These two gave, as expected, (almost) the same results. Remarkably, the analytical solution of Prandtl is a bit too high, especially for higher friction angles. This can be explained by the loosening of the soil in Zone 2, due to the logarithmic spiral, leading to an easier failure mechanism, just as happened for the surcharge bearing capacity factor N_q .

The semi-analytical line in the figure describes the cohesion bearing capacity factor much better, and can be written as (see Van Baars, 2016b, 2017a, 2018a):

$$N_c = (N_q - 1) \cot \phi \quad \text{with:} \quad N_q = \cos^2 \phi \cdot K_p \cdot e^{\pi \tan \phi}. \quad (8.11)$$

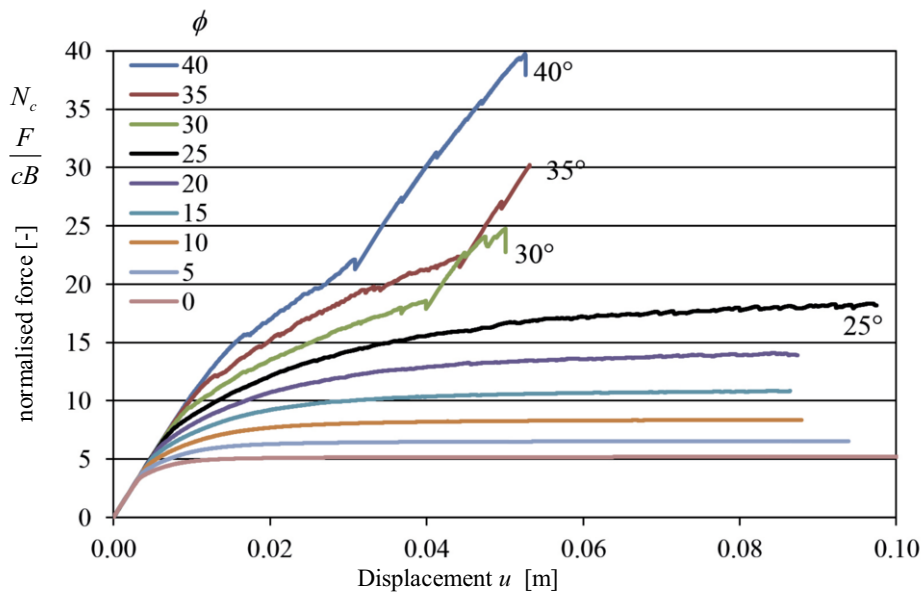


Figure 8-3. Normalised force versus displacement for different friction angles.

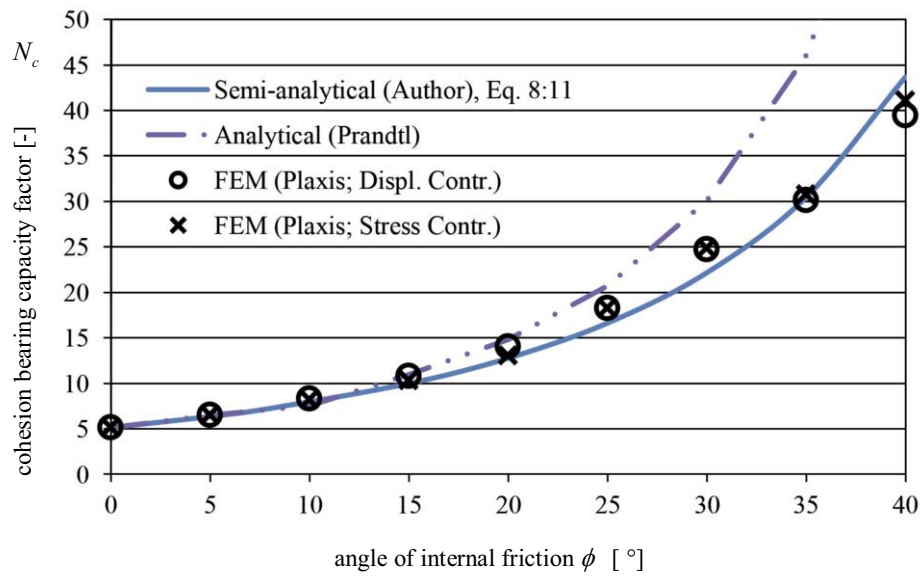


Figure 8-4. Cohesion bearing capacity factors: Prandtl versus FEM.

9 Soil-weight bearing capacity factor N_γ

9.1 Scaled modelling

The effects of the cohesion are taken into account by the cohesion bearing capacity factor N_c and the effects of a surcharge are taken into account by the surcharge bearing capacity factor N_q . So, the soil-weight bearing capacity factor N_γ regards the additional effect of the gravity on a frictional, but cohesionless material without a surcharge. The fact that the failure mechanism for the soil-weight bearing capacity is different from the bearing capacity for the cohesion, and also for the surcharge, has already been known for some time. In 1966 Caquot and Kerisel published in their book “*Traité de Méchanique des sols*” the circular or elliptical failure mechanism of Figure 9-1.

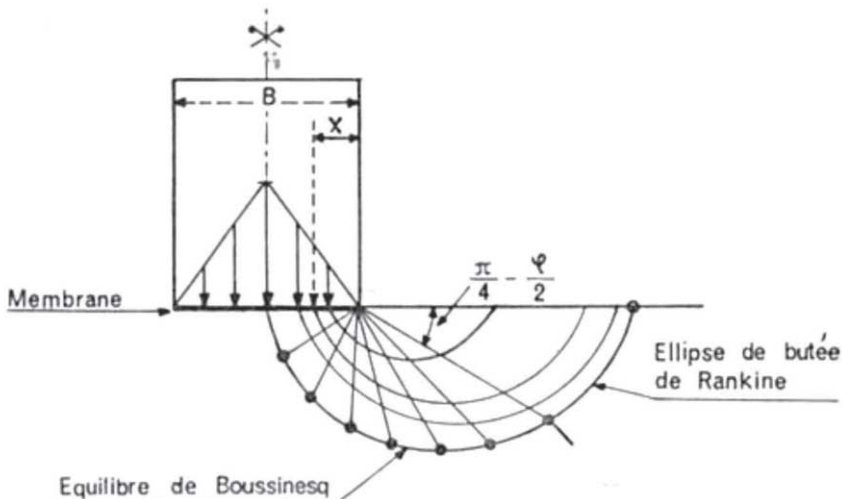


Figure 9-1. Failure mechanism for the soil weight bearing capacity factor N_γ .

This circular failure mechanism can also be observed in the photo of Figure 9-2 which can be found in the book “*Soil Mechanics*” of Lambe and Whitman from 1969.

A constant, or rectangular shaped, load p is impossible because just next to the load there is no strength for a cohesionless material without a surcharge. So, unlike the effect of the cohesion or the effect of the surcharge, the effect of the soil-weight does not result in a constant maximum load p . There will be though a maximum load in the middle and a zero load at the edges, where the shear and normal stresses go to zero too. This explains why, in the figure of Caquot and Kerisel, not a rectangular load, but a triangle shaped load is drawn. But in fact, finite element modelling shows that the stress under a footing on non-cohesive soil has a hyperbolic shape (see Figure 9-3).

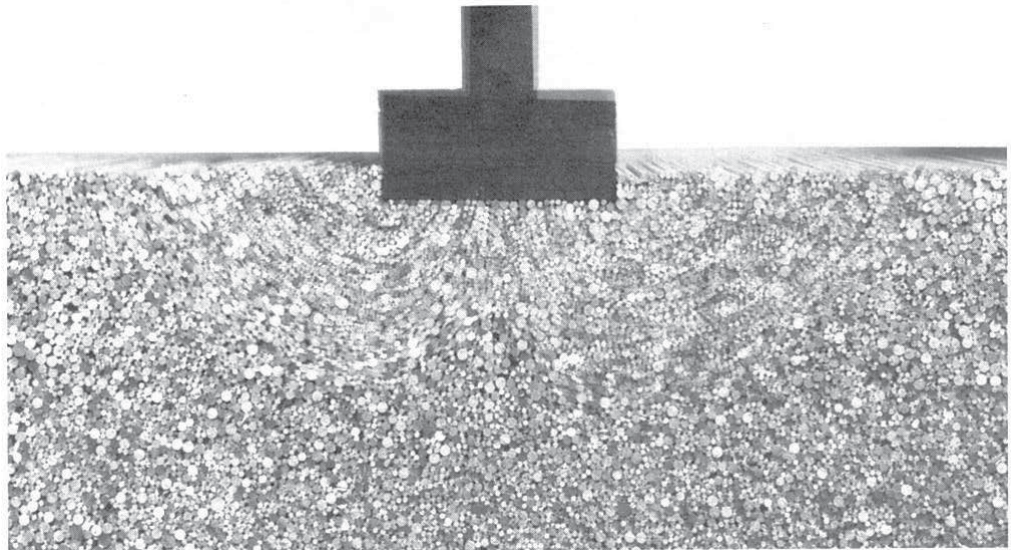


Figure 9-2. Laboratory test with cylinders: circular failure zones under a footing.

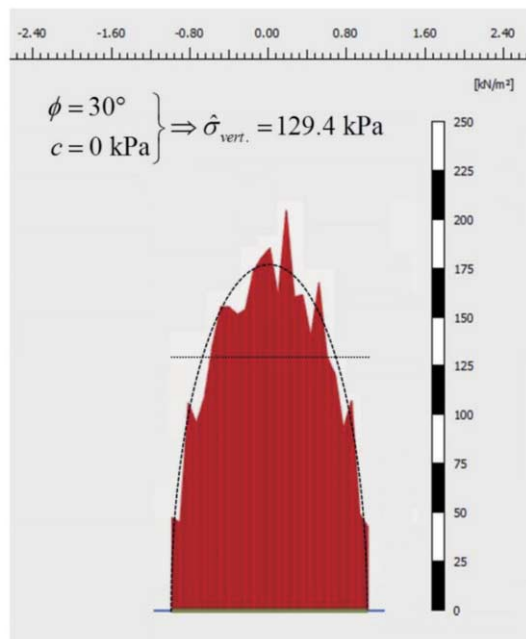


Figure 9-3. Finite Element Modelling: Stress under a footing has a hyperbolic shape.

The effect of the condition of zero bearing capacity at the edges, but not in the middle, explains the shape of a print in the sand of a flat shoe (see Figure 9-4), since for a shoe on the sand there is also no bearing capacity due to a surcharge or cohesion, but only due to the soil-weight.



Figure 9-4. Shoe print in sand: bearing capacity in the middle, but not at the edges.

The representation of this spatially variable load as a constant bearing capacity factor means that only an average component can be calculated for the soil-weight bearing capacity factor. Although the use of the soil-weight bearing capacity factor, in the same way as the other two bearing capacity factors, suggests also a constant maximum load or bearing capacity at the surface, it should be clear that this is definitely not the case.

9.2 Numerical solution

Keverling Buisman (1940), Terzaghi (1943), Caquot and Kérisel (1953, 1966), Meyerhof (1951, 1953, 1963, 1965), Brinch Hansen (1970), Vesic (1973, 1975) and Chen (1975) subsequently proposed different equations for the soil-weight bearing capacity factor N_y . Therefore the following equations for the soil-weight bearing capacity factor can be found in the literature:

$$\begin{aligned} N_y &= \left(K_p \cdot e^{\pi \tan \phi} - 1 \right) \tan(1.4\phi) \quad (\text{Meyerhof, 1963}), \\ N_y &= 1.5 \left(K_p \cdot e^{\pi \tan \phi} - 1 \right) \tan \phi \quad (\text{Brinch Hansen, 1970}), \\ N_y &= 2 \left(K_p \cdot e^{\pi \tan \phi} + 1 \right) \tan \phi \quad (\text{Vesic, 1973}), \\ N_y &= 2 \left(K_p \cdot e^{\pi \tan \phi} - 1 \right) \tan \phi \quad (\text{Chen, 1975}). \end{aligned} \tag{9.1}$$

In most publications the names of (Albert Sybrandus) Keverling Buisman and (Jørgen) Brinch Hansen are incorrectly cited. The equation from Brinch Hansen is, as he writes, “based on calculations first from Lundgren and Mortensen (1953) and later from Odgaard and N. H. Christensen”. The equation of Vesic is almost identical to the solution of Caquot and Kérisel (1953) because it is, as he writes, based on “the numerical results of an analysis made by them under the assumption that (the dilatancy angle) $\psi = 45^\circ + \phi/2$approximated with an error on the safe side”.

The equation of Chen and also others like Michalowski (1997) are based on the limit-equilibrium analysis, in which the soil is modelled as a perfectly plastic material obeying an associated flow rule.

Although Chen's equation is used in Eurocode 7, without reference, caution is still needed, because Yu et al. (1998) concluded: “*although the limit-equilibrium analysis is used widely...., its use may lead sometimes to significant errors as both kinematic and static admissibility are violated in the method*”.

Another important point is given by Hjiaj et al (2005), who wrote: “*As discussed by Chen (1975), the analysis of cohesionless (frictional) soil with self-weight is complicated by the fact that the shear strength increases with depth from a value of zero at the ground surface. This means that the Prandtl failure mechanism is no longer capable of yielding exact results, ..., this leads to the conclusion that the bearing capacity obtained (by) using this mechanism can, at best, only be an upper bound of the correct value.*”

Because of the discussions around the current solutions for the soil-weight bearing capacity factor, these solutions have been checked with displacement controlled calculations with the finite element model (FEM) Plaxis for a dilatancy angle $\psi = 0$.

The incremental displacement plots (see Figure 9-5), of these finite element calculations for the soil-weight bearing capacity factor, indicate that the displaced area (area with the lightest colour) forms a circular-wedge failure mechanism, which looks like the circular-wedge failure mechanism of Figure 9-2, and not like the much larger Prandtl-wedge failure mechanism (Van Baars, 2016a).

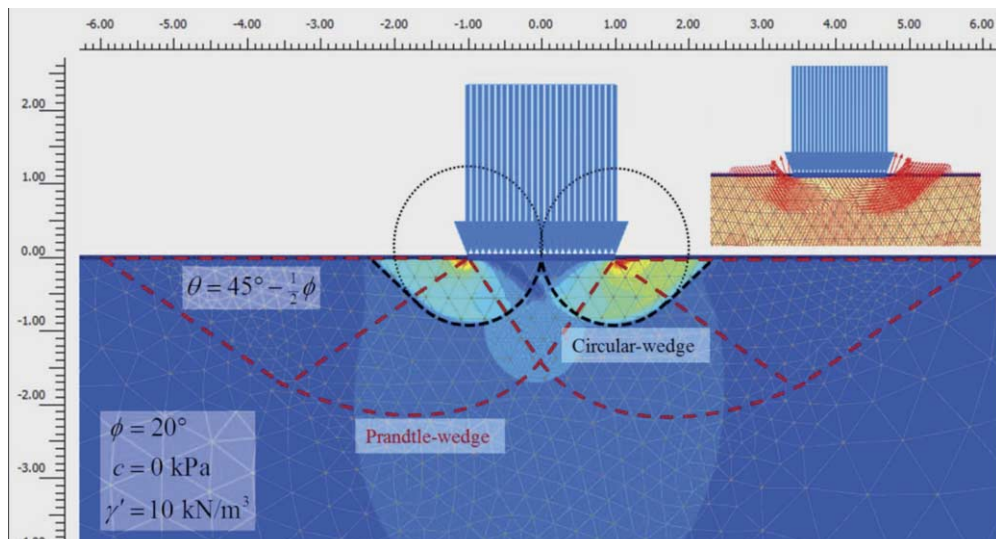


Figure 9-5. Numerical modelling: circular failure zones under a footing.

Figure 9-6 shows the results of the soil-weight bearing capacity factor. For this figure calculations have been made for both a rough plate (no horizontal displacement of the soil below the plate) and a smooth plate (free horizontal displacement). Nevertheless, for higher internal friction angles, the results of the equations in literature (Equation 9.1) are too high.

The highest results are found for the displacement controlled calculations for the rough plate:

$$N_y = 7 \sin \phi \cdot (e^{\pi \tan \phi} - 1) \text{ (Thin line).} \quad (9.2)$$

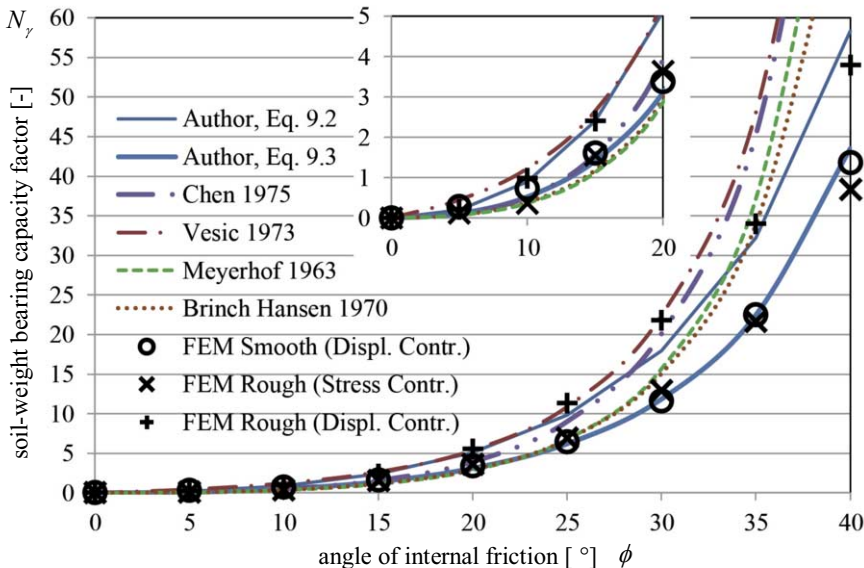


Figure 9-6. The soil-weight bearing capacity factor N_y .

Curiously, the stress controlled calculations with a rough plate give, for the displacement controlled calculations, results which are lower for the rough plate, and are at the same time rather identical for the smooth plate. Nevertheless, for higher internal friction angles, the results of the equations in literature (Equation 9.1) are too high. Van Baars (2015, 2016b, 2017a, 2018a) proposed therefore to use lower and safer equations, such as for example (see the empirical straight lines in the figure based on FEM):

$$N_y = 4 \tan \phi \cdot (e^{\pi \tan \phi} - 1) \text{ (Thick line).} \quad (9.3)$$

Both the stress controlled rough plate calculation results and the displacement controlled smooth plate calculation results can be described by this equation.

10 Superposition and bearing capacity factors

10.1 Table of bearing capacity factors

The outcome of the bearing capacity factors of the previous chapters can be summarised in the following table.

ϕ	N_c	N_q	N_γ	ϕ	N_c	N_q	N_γ
0	5.142	1.000	0.000	20	12.778	5.651	3.112
1	5.360	1.094	0.004	21	13.449	6.163	3.593
2	5.590	1.195	0.016	22	14.166	6.724	4.134
3	5.831	1.306	0.038	23	14.933	7.339	4.745
4	6.085	1.426	0.069	24	15.755	8.015	5.432
5	6.353	1.556	0.111	25	16.637	8.758	6.206
6	6.634	1.697	0.164	26	17.584	9.576	7.079
7	6.931	1.851	0.231	27	18.603	10.479	8.064
8	7.244	2.018	0.312	28	19.702	11.476	9.176
9	7.574	2.200	0.408	29	20.888	12.578	10.433
10	7.922	2.397	0.522	30	22.172	13.801	11.856
11	8.291	2.612	0.654	31	23.563	15.158	13.469
12	8.680	2.845	0.808	32	25.075	16.668	15.300
13	9.092	3.099	0.984	33	26.720	18.352	17.383
14	9.528	3.376	1.185	34	28.516	20.234	19.758
15	9.991	3.677	1.415	35	30.480	22.342	22.471
16	10.482	4.006	1.677	36	32.633	24.709	25.578
17	11.004	4.364	1.973	37	35.001	27.375	29.145
18	11.558	4.756	2.307	38	37.612	30.386	33.253
19	12.149	5.183	2.685	39	40.499	33.796	37.997
20	12.778	5.651	3.112	40	43.703	37.671	43.495

Table 10-1: Bearing capacity coefficients.

These factors are for non-dilatant soils and are all based on the Finite Element calculations mentioned in the previous chapters (Eqs. 7.10, 8.11 and 9.3) and are lower, especially for higher friction angles, more accurate and therefore safer than the factors mostly used.

10.2 Superposition

Terzaghi (1943) assumed that the bearing capacities of the three components are independent and that their failure mechanisms are the same, so that superposition is permitted ($p = cN_c + qN_q + \frac{1}{2}\gamma BN_\gamma$). In fact, this is not correct, because, as explained in Chapter 9, the failure mechanism belonging to the soil-weight (N_γ) is not the same as the failure mechanism belonging to both the cohesion (N_c) and the surcharge (N_q).

In order to illustrate this, several numerical calculations have been made (Van Baars, 2016b). One for a footing in which the three bearing components are combined with equal weight, by using a cohesion, surcharge and soil weight of $c = q = \frac{1}{2}\gamma B = 10$ kPa (Figure 10-1). Additionally three calculations have been made for the three bearing components independently (Figure 10-2). The friction angle is for all cases $\phi = 30^\circ$. The first calculation results in a combined bearing capacity of $N_c + N_q + N_\gamma = 61.0$, while independently the bearing capacities are: $N_c = 24.5$; $N_q = 14.6$; $N_\gamma = 12.6$, showing a $(61.0 - 24.5 - 14.6 - 12.6) / 61.0 = 15.2\%$ underestimation with the superposition rule. This error is caused by the fact that the failure mechanism for the combined loading (Figure 10-1), is different from the optimised failure mechanisms for the three individual bearing capacity components (Figure 10-2).

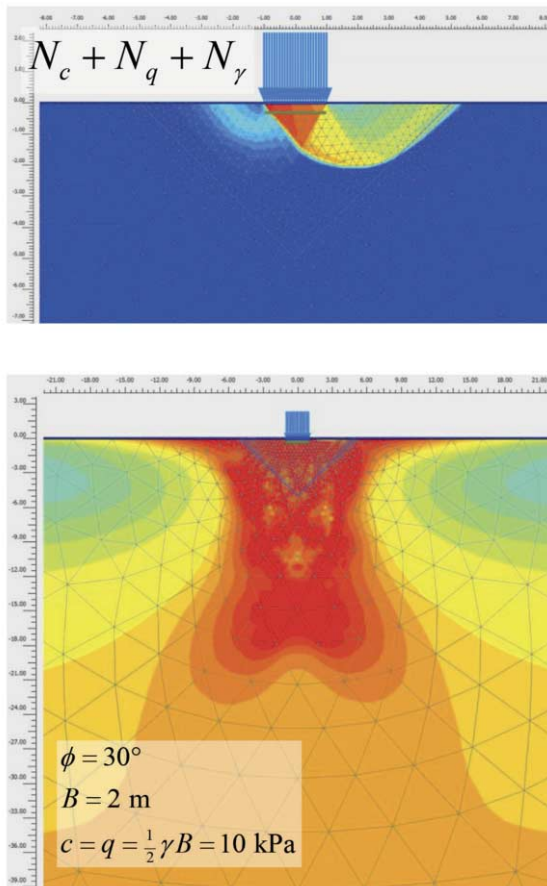


Figure 10-1. Failure of footing with combined: cohesion, surcharge and soil weight.
Above: Incremental displacements at failure (indicating failure mechanism).
Below: Relative shear stress at failure (indicating plastic zone).

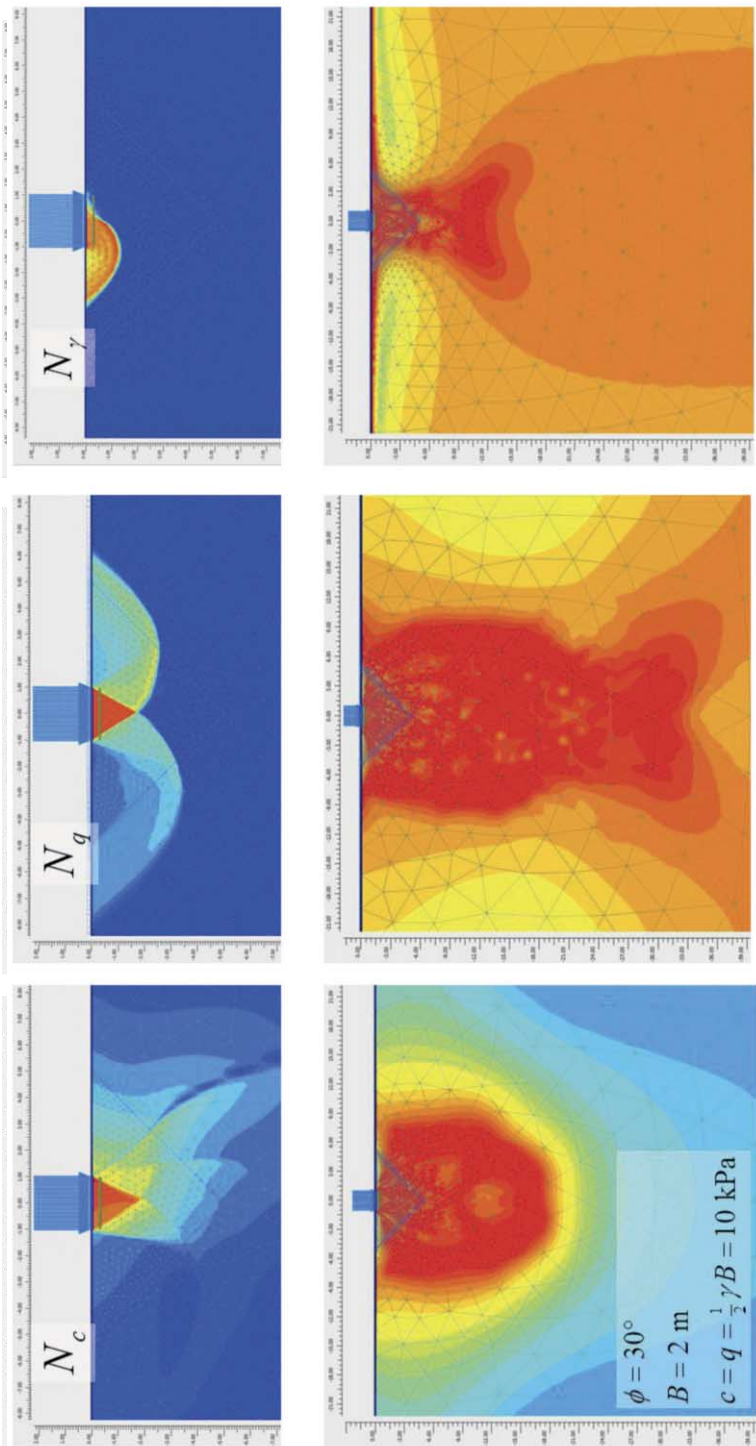


Figure 10-2. Failure of footing, independently: cohesion, surcharge and soil weight.

IV Correction factors

11 Extensions: correction factors

In 1953 the, German born, Canadian George G. Meyerhof was the first to propose equations for inclined loads. In 1963, he was also the first to write the formula for the (vertical) bearing capacity p_v , with both inclination factors and shape factors as correction coefficients, in order to take into account the shape of the loaded area and the inclination of the load:

$$p_v = i_c s_c c N_c + i_q s_q q N_q + i_\gamma s_\gamma \frac{1}{2} \gamma B N_\gamma. \quad (11.1)$$

In this equation the coefficients i_c , i_q and i_γ are correction factors for a possible inclination of the load (inclination factors), and s_c , s_q and s_γ are correction factors for the shape of the loaded area (shape factors).

Brinch Hansen (1970) later adopted this equation. Over the years, this equation has become the standard equation for the bearing capacity of shallow foundations.

There are also some other correction factors which are used today, such as the correction factors for a footing near a sloping soil surface, or a sloping (inclined) foundation footing.

Although Equation 11.1 is widely used nowadays, the applied superposition in this equation is scientifically speaking not correct, as explained in Chapter 9 and Chapter 10. However, it does not lead to large errors, and these are always an underestimation, which means predictions will always be on the safe side.

By using the inclination factors and the shape factors, or even both at the same time, there is a risk for additional errors in the assumed superposition.

12 Inclination factors

12.1 Meyerhof and Brinch Hansen

In the case of an inclined load, i.e. loading by a vertical force and a horizontal load at the same time, the additional horizontal load can considerably reduce the vertical bearing capacity. At the same time the horizontal component of the load is limited due to the Coulomb shear failure at the foundation surface:

$$p_h \leq c + p_v \tan \phi. \quad (12.1)$$

In 1953, Meyerhof published the results of his laboratory experiments on inclined loading on “purely cohesion materials” and “cohesionless materials”, (see Figure 12-1) for cases in which the horizontal component of the load is smaller than its maximum possible value (due to Coulomb shear failure). The correction factors for a certain load inclination angle α were expressed by him in 1963 as:

$$i_q = i_c = \left(1 - \frac{\alpha^\circ}{90^\circ}\right)^2, \quad i_\gamma = \left(1 - \frac{\alpha^\circ}{\phi^\circ}\right)^2, \quad \text{for: } \alpha < \phi. \quad (12.2)$$

In the United States of America, but also in many other countries, these factors are most commonly used (see also Das, 1999).

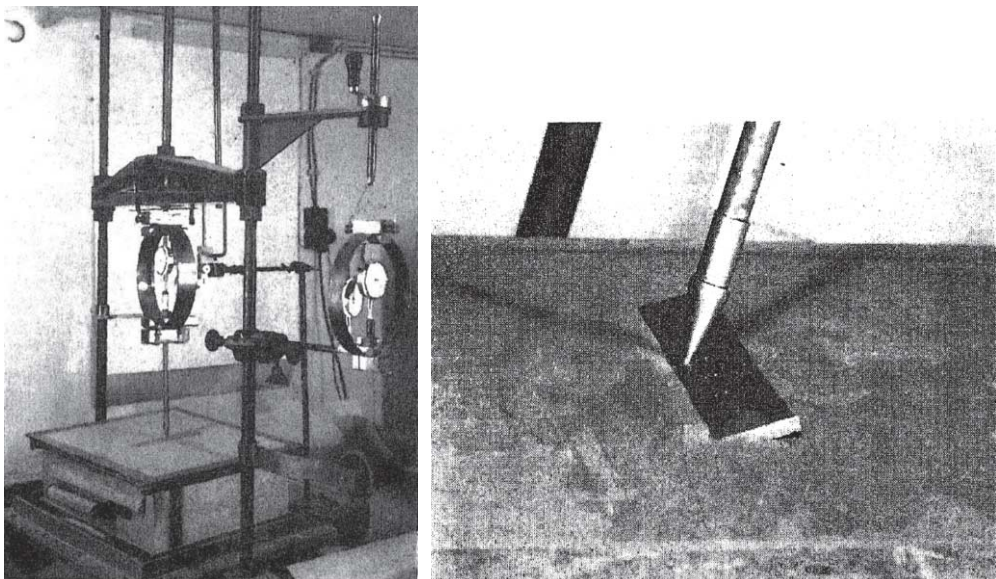


Figure 12-1. Model tests with inclined loaded footings (Meyerhof, 1953).

Brinch Hansen (1970) and Vesic (1975) proposed other inclination factors:

Brinch Hansen (1970):

$$i_c = 0.5 + 0.5 \sqrt{1 - \frac{p_h}{c}} \quad (\text{only for } \phi = 0),$$

$$i_q = \left(1 - \frac{0.5 p_h}{p_v + c \cdot \cot \phi} \right)^5, \quad i_\gamma = \left(1 - \frac{0.7 p_h}{p_v + c \cdot \cot \phi} \right)^5,$$
(12.3)

Vesic (1975):

$$i_c = \frac{i_q N_q - 1}{N_q - 1} = i_q - \frac{1 - i_q}{N_c \tan \phi},$$

$$i_q = \left(1 - \frac{p_h}{p_v + c \cdot \cot \phi} \right)^2, \quad i_\gamma = \left(1 - \frac{p_h}{p_v + c \cdot \cot \phi} \right)^3.$$

These equations for the inclination factors of Vesic (1975) are currently used in Eurocode 7 (2004). The last two equations of Vesic are, as he writes, based on the work of Sokolovskii (1960) and Brinch Hansen (1970).

The equations for i_q and i_γ are an incorrect mixture of the Coulomb shear failure criterion ($\tau = c + \sigma \cdot \tan \phi$) which should only be applied at the interface, with the Mohr-Coulomb bearing capacity failure (Figure 12-2) of the half-space below the interface. A clear indication of the incorrectness of his solution is the fact that the proposed inclination factors depend on the cohesion, c , while the bearing capacity factors, for any inclination, and therefore also the inclination factors, should not depend on the cohesion, c . The reason for this is that, the bearing capacity factors (especially the non-cohesive factors N_q and N_γ) only depend on the shape of the Prandtl-wedge, which only depends on the angle of internal friction and the load angle, and not on the cohesion.

The first equation, about the cohesion inclination factor, i_c , was published first by De Beer and Ladany (1961), and is based on the assumption that the equation for the cohesion bearing capacity ($N_c = (N_q - 1) \cot \phi$) is also valid for inclined loading ($i_c N_c = (i_q N_q - 1) \cot \phi$). Vesic (1975) calls this "*the theorem of correspondence*", and Bolton (1979) calls this "*the usual trick*". This relation between N_c and N_q is coincidentally valid for vertical ultimate loads. However, according to the results of the numerical calculations, and also according to the analytical solution given later in this book, the assumption that this is also the case for inclined loading, is not correct.

This indicates that the inclination factors proposed by Brinch Hansen and Vesic are incorrect and should not be used.

In the following chapters, the failure mechanism for inclined loads, presented in Figure 12-2, will be studied; analytical solutions will be derived and compared to the equation of Meyerhof, based on his laboratory test, and these will also be compared to the results of finite element calculations (Van Baars, 2018a).

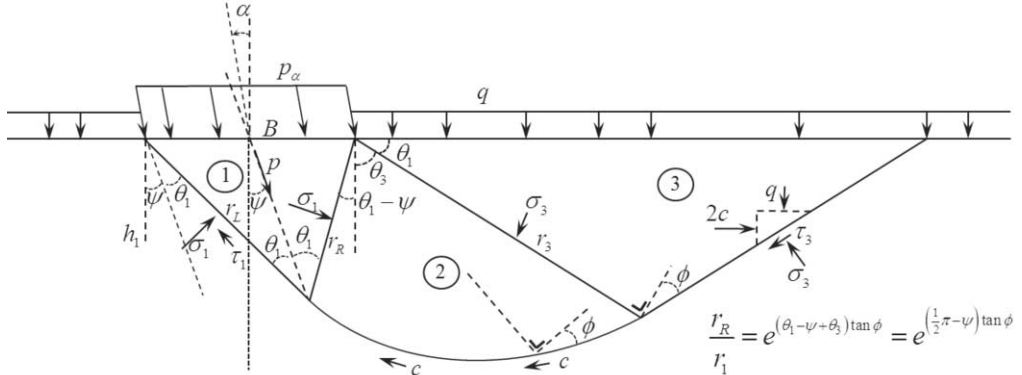


Figure 12-2. Prandtl-wedge for inclined loads (copy of Figure 8-1).

12.2 Surcharge fan reduction angle ψ_q

Zone 2 with the shape of the logarithmic spiral is also called the fan. The fan is reduced due to the inclined load. The surcharge fan reduction angle ψ_q of Zone 2 can be calculated for non-cohesive soils from Figure 12-3, which depicts the stresses of the inclined Prandtl-wedge and is also used by Bolton (1979).

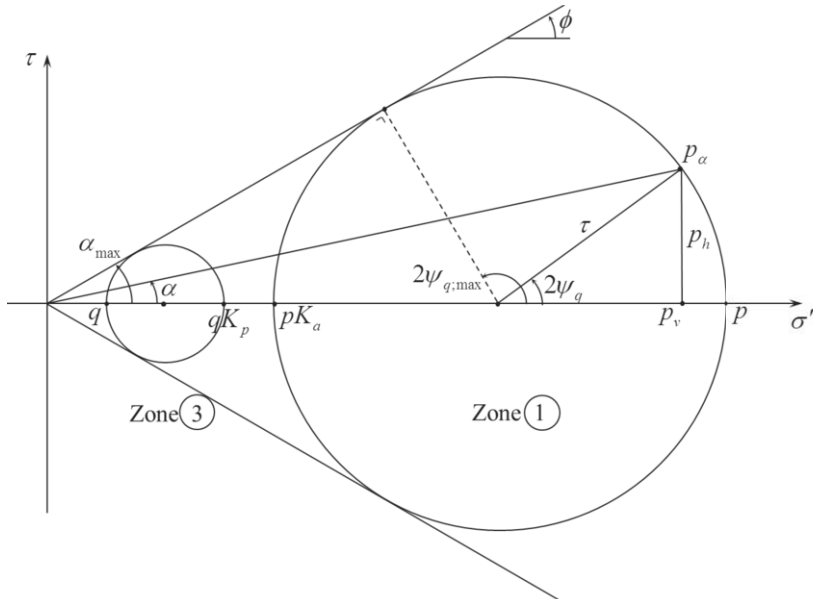


Figure 12-3. Mohr-Coulomb circles and fan reduction angle.

The following three equations follow from this figure. The load angle yields:

$$\frac{p_h}{p_v} = \tan \alpha. \quad (12.4)$$

The radius of the Mohr circle of Zone 1 gives:

$$\frac{\tau}{p} = \frac{(1 - K_a)}{2}$$

$$\Rightarrow \frac{\tau}{p} = S = \frac{\sin \phi}{1 + \sin \phi} \Rightarrow \frac{1}{S} - 1 = \frac{1}{\sin \phi}$$

with: $K_a = \frac{1 - \sin \phi}{1 + \sin \phi}$. (12.5)

The relation between the vertical stress and the maximum stress results in:

$$p_v + \tau(1 - \cos 2\psi_q) = p \Rightarrow$$

$$\frac{p_v}{p} = 1 + S(\cos 2\psi_q - 1) \quad \text{or for } \alpha \ll \phi : \frac{p_v}{p} \approx \cos \alpha \quad \text{span style="float: right;">(12.6)}$$

These three equations can be implemented in a fourth equation:

$$\begin{aligned} \sin 2\psi_q &= \frac{p_h}{\tau}, \\ &= \frac{p_h}{p_v} \cdot \frac{p_v}{p} \cdot \frac{p}{\tau}, \\ &= \tan \alpha \cdot [1 + S(\cos 2\psi - 1)] \cdot \frac{1}{S}, \\ &= \frac{\tan \alpha}{\sin \phi} + \tan \alpha \cdot \cos 2\psi, \end{aligned} \quad \text{span style="float: right;">(12.7)}$$

from which the surcharge fan reduction angle ψ_q can be calculated (iteratively). With this equation, the following surcharge fan reduction angles can be found:

$$\begin{aligned} \alpha = 0 : \quad \psi_q &= 0 \\ \text{for: } \alpha \ll \phi : \quad \psi_q &= \frac{1}{2} \arcsin \left(\frac{\sin \phi \cdot \sin \alpha}{1 + \sin \phi} \right) \\ \tan \alpha = \sin \phi : \quad \psi_q &= 45^\circ \\ \alpha_{\max} = \phi : \quad \psi_{q,\max} &= 45^\circ + \frac{1}{2}\phi \end{aligned}$$

12.3 Cohesion fan reduction angle ψ_c

The cohesion fan reduction angle ψ_c will be approximated by writing the cohesion as:

$$c = \frac{P_v}{i_c N_c}. \quad \text{span style="float: right;">(12.8)}$$

The radius of the Mohr circle of Zone 1 gives:

$$\frac{\tau}{p} = \frac{(1 - K_a + 2c\sqrt{K_a})}{2} \quad \text{with: } K_a = \frac{1 - \sin \phi}{1 + \sin \phi}. \quad \text{span style="float: right;">(12.9)}$$

This gives:

$$\begin{aligned}\sin 2\psi_c &= \frac{p_h}{p_v} \cdot \frac{p_v}{p} \cdot \frac{p}{\tau}, \\ &= \tan \alpha \cdot \frac{p_v}{p} \cdot \frac{2}{1 - K_a + \frac{2p_v}{i_c N_c p} \sqrt{K_a}}.\end{aligned}\quad (12.10)$$

Solving the cohesion fan reduction angle ψ_c would mean, that first the cohesion inclination factor i_c would have to be solved before solving the fan reduction angle ψ_c , and at the same time the fan reduction angle ψ_c would have to be solved before solving the cohesion inclination factor i_c . Due to the complexity of both equations, this is however not really possible. For a relatively small load inclination angle α , the fan reduction angle ψ_c can be solved though, because in this case:

$$\sin \alpha \approx \alpha; \quad i_c \approx 1; \quad \frac{p_v}{p} \approx \cos \alpha \approx 1; \quad \psi_c \leq 90^\circ. \quad (12.11)$$

This yields for the cohesion fan reduction angle:

$$\psi_c \approx \min\left(\frac{\alpha}{1 - K_a + \frac{2}{N_c} \sqrt{K_a}}; 90^\circ\right) \quad (12.12)$$

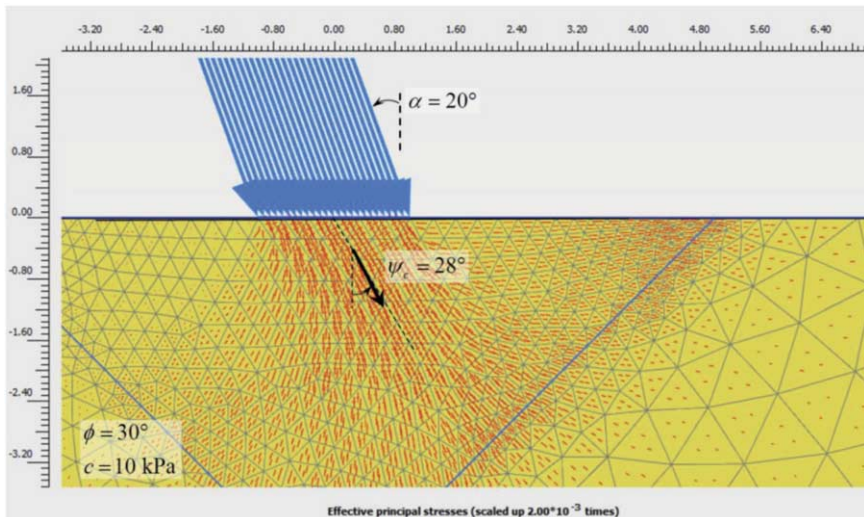


Figure 12-4. Rotation of the principal direction in Zone 1.

Having both a surcharge and a cohesion, will result in a single fan reduction angle, which will be somewhere in between the two fan reduction angles. This means the cohesion and the surcharge influence each other's inclination factors. Consequently, writing the surcharge part and the cohesive part completely separately, as suggested by the Meyerhof bearing capacity equation, is, scientifically speaking, not completely correct.

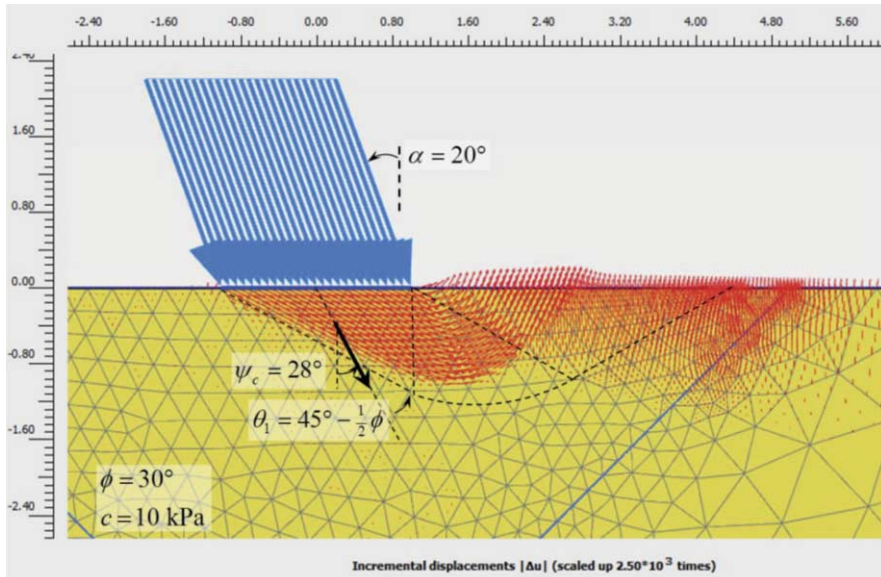


Figure 12-5. Incremental displacements and rotated Prandtl-wedge.

12.4 Surcharge inclination factor i_q

Van Baars (2014, 2018a) published the analytical solution for the surcharge inclination factor, i_q , based on a rotated Prandtl-wedge failure mechanism. For this mechanism, the solution for the surcharge inclination factor can be found analytically by determining and multiplying together the principal stress ratios in each zone.

Zone 3

For Zone 3 all equations and even all stresses remain the same.

Zone 2

For Zone 2, for both the principal stress and the size of the fan, the rotation angle $(\theta_1 + \theta_3 = \frac{1}{2}\pi)$ reduces due to the surcharge fan reduction angle ψ_q , so the equation used in Chapter 7 is changed to (see Figure 12-2):

$$\frac{\sigma_1}{\sigma_3} = \frac{\tau_1}{\tau_3} = \frac{r_3^2}{r_R^2} = \left(e^{\left(\frac{1}{2}\pi - \psi_q\right) \tan \phi} \right)^2 = e^{(\pi - 2\psi_q) \tan \phi}. \quad (12.13)$$

Zone 1

For Zone 1, all equations stay the same.

The inclination factors are influenced by the effects of the three zones, but also by the fact that they are based on the vertical component of the inclined bearing capacity, so:

$$p_v \approx \cos \alpha \cdot p \quad (12.6)$$

Analytical solution

A combination of all these effects, results in the following analytical solution for the surcharge inclination factor, which is defined as the (vertical component) of the inclined bearing capacity divided by the non-inclined bearing capacity:

$$\begin{aligned}
 i_q &= \frac{P_{v;q(\alpha>0)}}{P_{v;q(\alpha=0)}}, \\
 &= \cos \alpha \cdot \frac{p_{q(\alpha>0)}}{p_{q(\alpha=0)}}, \\
 &= \cos \alpha \cdot i_{q,1} \cdot i_{q,2} \cdot i_{q,3}, \\
 &= \cos \alpha \cdot 1 \cdot \frac{\left(\frac{r_3}{r_R}\right)^2}{\left(\frac{r_3}{r_1}\right)^2} \cdot 1, \\
 &= \cos \alpha \cdot \frac{e^{(\pi - 2\psi_q) \tan \phi}}{e^{(\pi) \tan \phi}}, \\
 i_q &= \cos \alpha \cdot e^{-2\psi_q \tan \phi}.
 \end{aligned} \tag{12.14}$$

This solution is however limited due to Coulomb shear failure of the load at the surface interface. By also taking this into account, the inclination factor becomes:

$$\begin{aligned}
 i_q &= \cos \alpha \cdot e^{-2\psi_q \tan \phi} \quad (\alpha < \phi), \\
 &= 0 \quad (\alpha > \phi).
 \end{aligned} \tag{12.15}$$

Numerical results

This analytical solution has been compared with the results of FEM calculations.

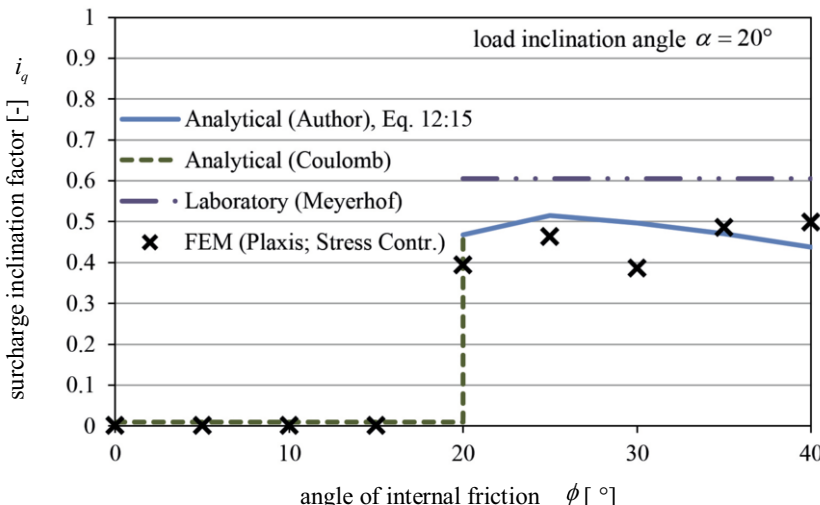


Figure 12-6. Surcharge inclination factor: Analytical, Laboratory and FEM.

In order to have zero effective stresses due to the soil-weight, the cohesion is taken zero and the saturated weight of the soil is taken equal to the weight of the water. In this way all effects due to the cohesion bearing capacity N_c and the soil-weight bearing capacity N_γ are excluded.

The analytical relationship is presented in Figure 12-6, for a load inclination angle of $\alpha = 20^\circ$, together with the relationship of the laboratory experiments of Meyerhof (Equation 12.2) and with the results of the FEM calculations.

The analytical solution is close to the FEM results and even describes them better than the empirical equation of Meyerhof, as can be seen from Figure 12-6.

12.5 Cohesion inclination factor i_c

Analytical solution

Van Baars (2014, 2018a) showed that, similarly to the analytical solution of the surcharge inclination factor, i_q , an analytical solution of the cohesion inclination factor, i_c can be found, but only at the following two boundary conditions:

$$\begin{aligned}\phi = 0: \quad i_c &= \cos \alpha \cdot \frac{2 + \pi - 2\psi_c}{2 + \pi} \\ \phi \gg 0: \quad i_c &= i_q.\end{aligned}\tag{12.16}$$

Based on these analytical boundary solutions, one can make a short equation for the variable i_c which goes gradually from the zero boundary into the infinite boundary, which is:

$$i_c = \cos \alpha \cdot \left(e^{-2\psi_c \tan \phi} - \frac{2\psi_c}{2 + \pi} \cdot e^{-\pi \tan \phi} \right)\tag{12.17}$$

This solution is only exact at the boundaries and is an approximation in between. There is also a way however, to find the exact solution.

Since the inclination factor is defined as the (vertical component) of the inclined bearing capacity divided by the non-inclined bearing capacity:

$$i_c = \frac{P_{v;c(\alpha>0)}}{P_{v;c(\alpha=0)}} = \cos \alpha \cdot \frac{P_{c(\alpha>0)}}{P_{c(\alpha=0)}},\tag{12.18}$$

the exact cohesion inclination factor is (see chapter 8):

$$i_c = \cos \alpha \cdot \frac{\left\{ \cot \theta_l + \left(\frac{\tan \theta_l}{1 - \tan \theta_l \cdot \tan \phi} \right) \cdot e^{(\pi - 2\psi_c) \tan \phi} + \cot \phi \cdot \left(e^{(\pi - 2\psi_c) \tan \phi} - 1 \right) \right\} \cdot (1 + \cot \theta_l \cdot \tan \phi)}{\left\{ \cot \theta_l + \left(\frac{\tan \theta_l}{1 - \tan \theta_l \cdot \tan \phi} \right) \cdot e^{\pi \tan \phi} + \cot \phi \cdot \left(e^{\pi \tan \phi} - 1 \right) \right\} \cdot (1 + \cot \theta_l \cdot \tan \phi)}\tag{12.19}$$

or with simplification of the denominator:

$$i_c = \cos \alpha \cdot \frac{\left\{ \cot \theta_i + \left(\frac{\tan \theta_i}{1 - \tan \theta_i \cdot \tan \phi} \right) \cdot e^{(\pi - 2\psi_c) \tan \phi} + \cot \phi \cdot \left(e^{(\pi - 2\psi_c) \tan \phi} - 1 \right) \right\} \cdot (1 + \cot \theta_i \cdot \tan \phi)}{(K_p \cdot e^{\pi \tan \phi} - 1) \cot \phi} \quad (12.20)$$

This exact solution is, just like the surcharge inclination factor, limited due to Coulomb shear failure at the surface interface:

$$\left. \begin{aligned} \sigma_h &= c + \sigma_v \cdot \tan \phi \\ \sigma_h &= \sigma_v \cdot \tan \alpha \end{aligned} \right\} \Rightarrow \sigma_v = \frac{c}{\tan \alpha - \tan \phi} = i_c N_c c \\ \Rightarrow i_c = \frac{1}{N_c (\tan \alpha - \tan \phi)}. \quad (12.21)$$

So, by taking both inclined Prandtl failure and Coulomb shear failure into account, the cohesion inclination factor simply becomes the lowest factor of both failure mechanisms, which yields for the short equation (12.17):

$$i_c = \min \left\{ \begin{aligned} &\cos \alpha \cdot \left(e^{-2\psi_c \tan \phi} - \frac{2\psi_c}{2 + \pi} \cdot e^{-\pi \tan \phi} \right), \\ &\frac{1}{N_c (\tan \alpha - \tan \phi)}. \end{aligned} \right. \quad (12.22)$$

Figure 12-7 shows the comparison of this short equation (for a load inclination angle $\alpha = 20^\circ$) with the exact equation (12.20). The solutions are (almost) the same.

Numerical results

Both analytical relationships are presented in Figure 12-7, together with the equation of Meyerhof (Equation 12.2) based on his laboratory experiments and together with the results of the finite element calculations, for a load angle of 20° .

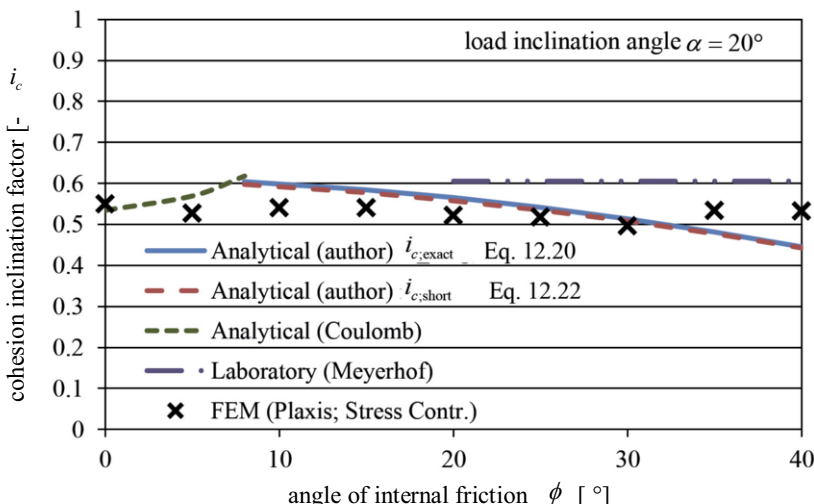


Figure 12-7. Cohesion inclination factor: Analytical, Laboratory and FEM.

Also in this case the analytical solution prescribes rather well to the FEM results and, as can be seen from this figure, is even more accurate than the Meyerhof equation for the inclination factors (Equation 12.2).

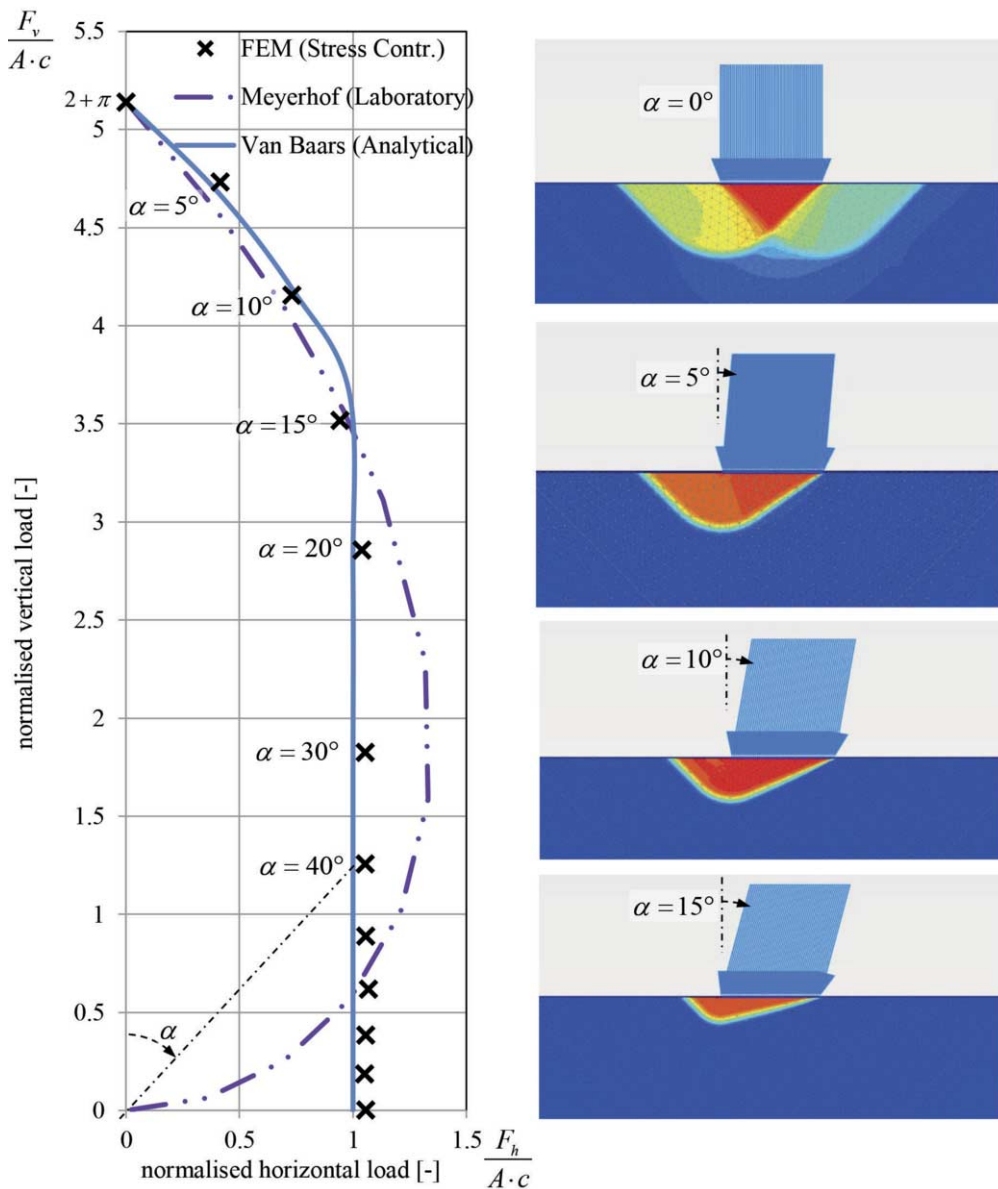


Figure 12-8. Cohesion inclination factor versus load angle.

Another interesting point is that there is a zone for the internal friction ($8^\circ < \phi < 20^\circ$, for $\alpha = 20^\circ$) in which the cohesion inclination factor depends on a Prandtl failure mechanism, while the surcharge inclination factor depends on a Coulomb shear failure mechanism. Since there are different failure mechanisms

occurring at the same time, the superposition of Meyerhof's bearing capacity equation (Equation 11.1) is, scientifically speaking, not permissible for this zone.

The accuracy of the analytical solution (Equations 12.12 and 12.22) can also be seen from a vertical load versus horizontal load plot with a variable load angle α , and a constant friction angle ($\phi = 0^\circ$), see Figure 12-8. This plot also shows how inaccurate the Meyerhof equation is for angles larger than 20 degrees.

12.6 Soil-weight inclination factor i_γ

The soil-weight inclination factor can only be obtained from numerical or laboratory tests, as Meyerhof did. Nevertheless, from the equation of Meyerhof for the soil-weight bearing capacity, it becomes clear that Meyerhof thought about a gradual reduction to zero and not about a sudden drop to zero (Coulomb shear failure) such as for the surcharge inclination factor. The empirical solution of Meyerhof (based on laboratory tests) has been plotted in Figure 12-10, together with the results from the finite element calculations. These calculations prove that the correction factors for the inclination of the load must be changed into (Van Baars, 2018a):

$$i_\gamma = \left(1 - \frac{\alpha^\circ}{90^\circ}\right)^5, \quad \text{for: } \alpha < \phi, \quad (12.23)$$

in order to fit the results of the numerical calculations.

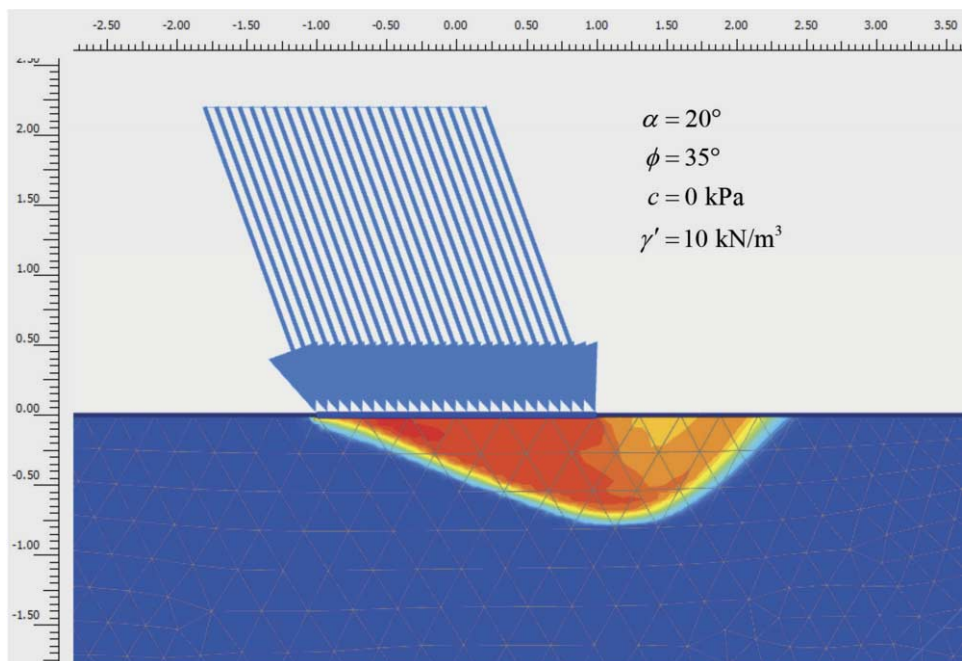


Figure 12-9. Soil-weight failure mechanism for inclined loading.

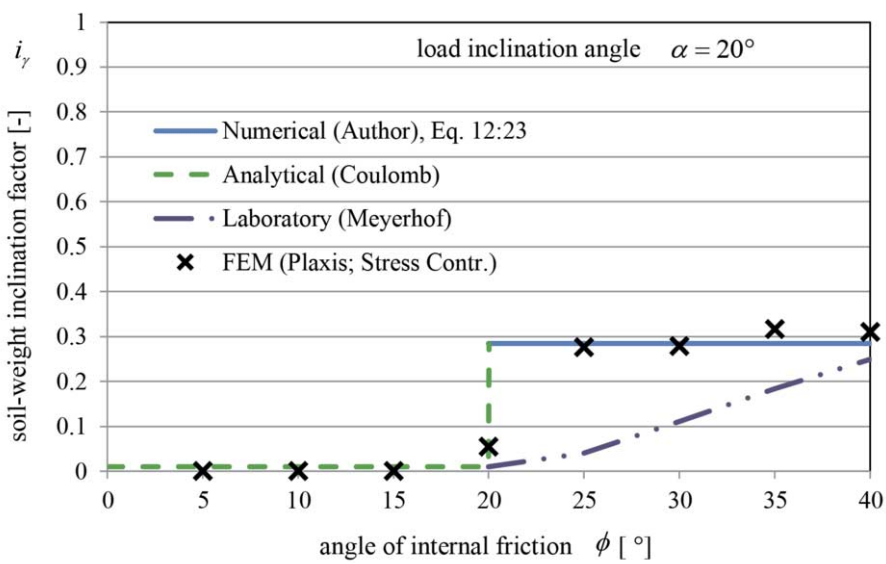


Figure 12-10. Soil-weight inclination factor: Laboratory and FEM.

13 Shape factors

13.1 Meyerhof and De Beer

If the shape of the foundation area is not an infinitely long strip, but a rectangular area, of width B and length L (where it is assumed, that the width is the shortest dimension, i.e., $L \geq B$), correction factors for the shape are used. Meyerhof (1963) was the first to publish shape factors:

$$s_q = s_\gamma = 1 + 0.1K_p \frac{B}{L} \sin \phi, \quad s_c = 1 + 0.2K_p \frac{B}{L} \quad \text{with: } K_p = \frac{1 + \sin \phi}{1 - \sin \phi} \quad (13.1)$$

A few years later De Beer (1970) published his shape factors, based on laboratory experiments. Brinch Hansen (1970) based his shape factors on the experimental results from De Beer. So the most commonly used shape factors are (for $B \leq L$):

$$s_c = 1 + 0.2 \frac{B}{L}, \quad s_q = 1 + \frac{B}{L} \sin \phi, \quad s_\gamma = 1 - 0.3 \frac{B}{L}. \quad (13.2)$$

There is still no international agreement on the precise values of these correction factors.

It may be noted that for $B/L = 0$, the formulas all give a factor 1, in agreement with the basic results for an infinite strip. It should also be remembered that $B/L \leq 1$, by definition.

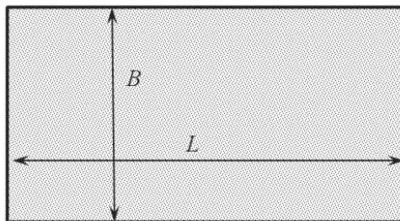


Figure 13-1. Rectangular area.

13.2 Axisymmetric failure versus plane strain failure

Knudsen and Mortensen (2016) compared for frictionless soils ($\phi = 0$), the bearing capacity for axisymmetric (2D Plaxis), circular, and square foundations (both 3D Plaxis). They found very similar results (deviation less than 3%). This means the shape factors can also be studied with axisymmetric calculations.

There is a risk in assuming an identical Prandtl-wedge shaped failure mechanism for circular or even elliptical shaped loaded areas, such as for example Figure 13-2. Van Baars (2014, 2015) showed that, for circular shallow foundations, the resulting shape factors are far too high, according to Finite Element calculations, and also according to the laboratory tests of De Beer. The reason for this is that the surface area of zone 3 of the Prandtl-wedge, the part next to the load, becomes too big, creating too much support, so before this Prandtl-wedge failure mechanism can occur, another

mechanism already occurs. For deep foundations though, this failure mechanism might still be interesting, see Chapter 18.

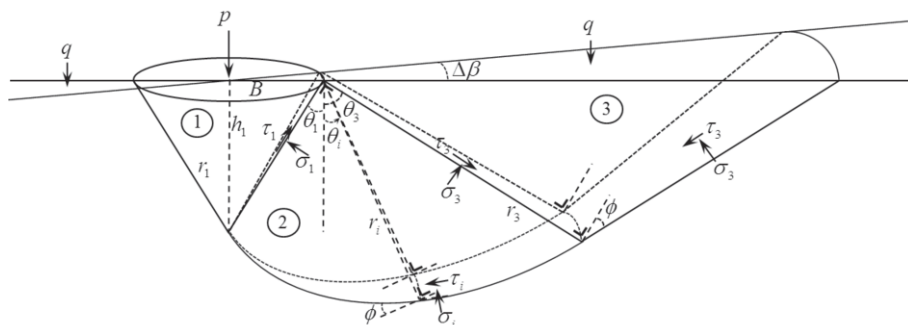


Figure 13-2. Prandtl-wedge approach for circular loaded areas.

For the strip load (plane strain solution) the minimum stress, in zone 3 of the wedge, is the vertical stress, which is zero without a surcharge, and the maximum stress is the horizontal stress (perpendicular to the load).

For the circular load (axisymmetry) however, the minimum stress, in zone 3 of the wedge, is not the vertical stress, but the tangential stress (out of the $x-y$ plane), which can be even below zero in case of a cohesion, so causing tension. Due to this cleaving failure mechanism, the bearing capacity of a circular load will be far less than of a strip load, resulting in shape factors below "1". In reality, for cohesive materials, there will be radial cracks formed, which eliminate the tangential tensile stresses and therefore increase the bearing capacity. The tangential stress is also called the hoop stress or the circumferential stress.

13.3 Cohesion shape factor s_c

Figure 13-3 shows the incremental displacements during failure for axisymmetric calculations in Plaxis 2D, for a circular loaded area ($D=4$ m) on two different cohesive soils, without a surcharge, indicating the failure mechanism.

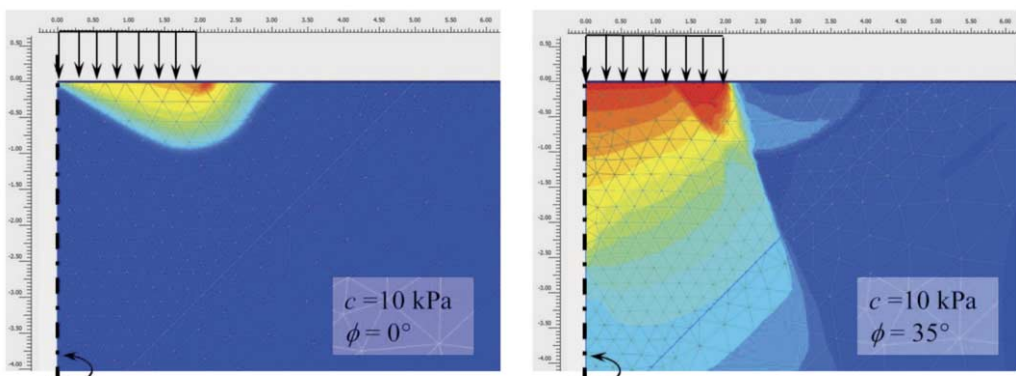


Figure 13-3. Failure mechanism for circular loaded areas (Incr. displacements).

The failure mechanism starts like the circular-wedge failure mechanism, in the middle of the loaded area, has 3 zones, like the Prandtl-wedge, and is found for all three bearing capacity cases (cohesion, surcharge and soil-weight). Due to axial symmetry, the circular wedge is pushed outwards during failure, causing a declining tangential stress.

The shape factor for circular (round) loads have been obtained from the axisymmetric calculations in Plaxis 2D. The displacement controlled calculations give a resulting load F_y for 1 rad, or half a circular load. The circular cohesion shape factor is therefore calculated by:

$$s_{c;round} = \frac{2F_y}{\left(\frac{1}{4}\pi D\right)(N_c c)} \quad \text{with:} \quad N_c = (N_q - 1)\cot\phi \\ N_q = \cos^2\phi \cdot K_p \cdot e^{\pi\tan\phi} \quad (13.3)$$

The shape factor for a circular footing (s_c for $B=L$) on cohesive soil has been plotted in Figure 13-4, for Meyerhof, De Beer and the outcome of the axisymmetric FEM calculations. The FEM results show that the currently used factors from Meyerhof in particular, but also from De Beer, are too high, so unsafe.

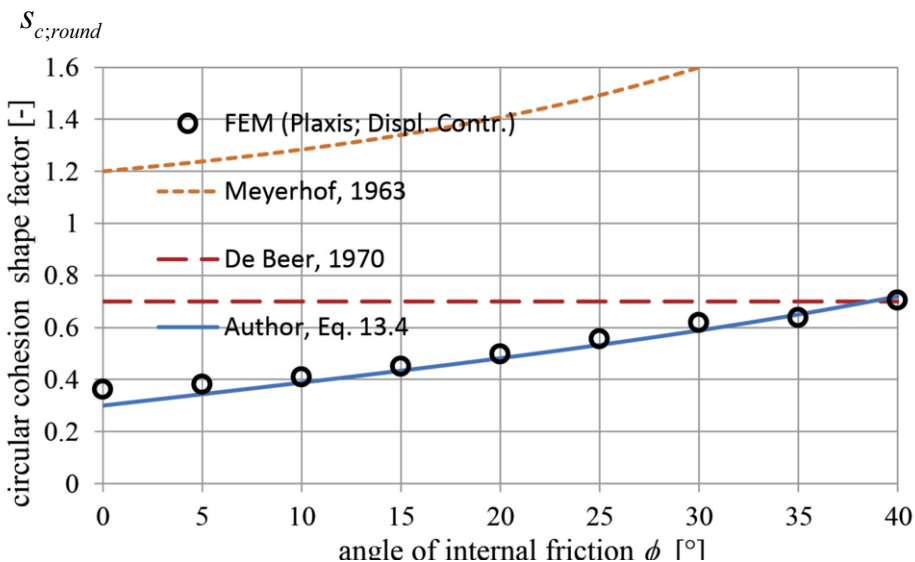


Figure 13-4. The circular cohesion shape factor.

From several publications, for example Zhu and Michalowski (2005), and Tapper et al. (2015), we can conclude that the shape factors are related to $\sqrt{\frac{B}{L}}$, and not to $\frac{B}{L}$.

This will be adopted here. The shape factor used for the straight line in the figure is (see Van Baars, 2017a, 2017b, 2018a):

$$s_c = 1 - (0.7 - 0.5 \tan\phi) \cdot \sqrt{\frac{B}{L}}. \quad (13.4)$$

13.4 Surcharge shape factor s_q

Figure 13-5 shows, for a circular shallow foundation, with surcharge q , during displacement controlled failure, the relative shear stresses for both the x - y plane, and also out of this plane, so for a plane including the tangential z -direction, or “out-of-plane” direction.

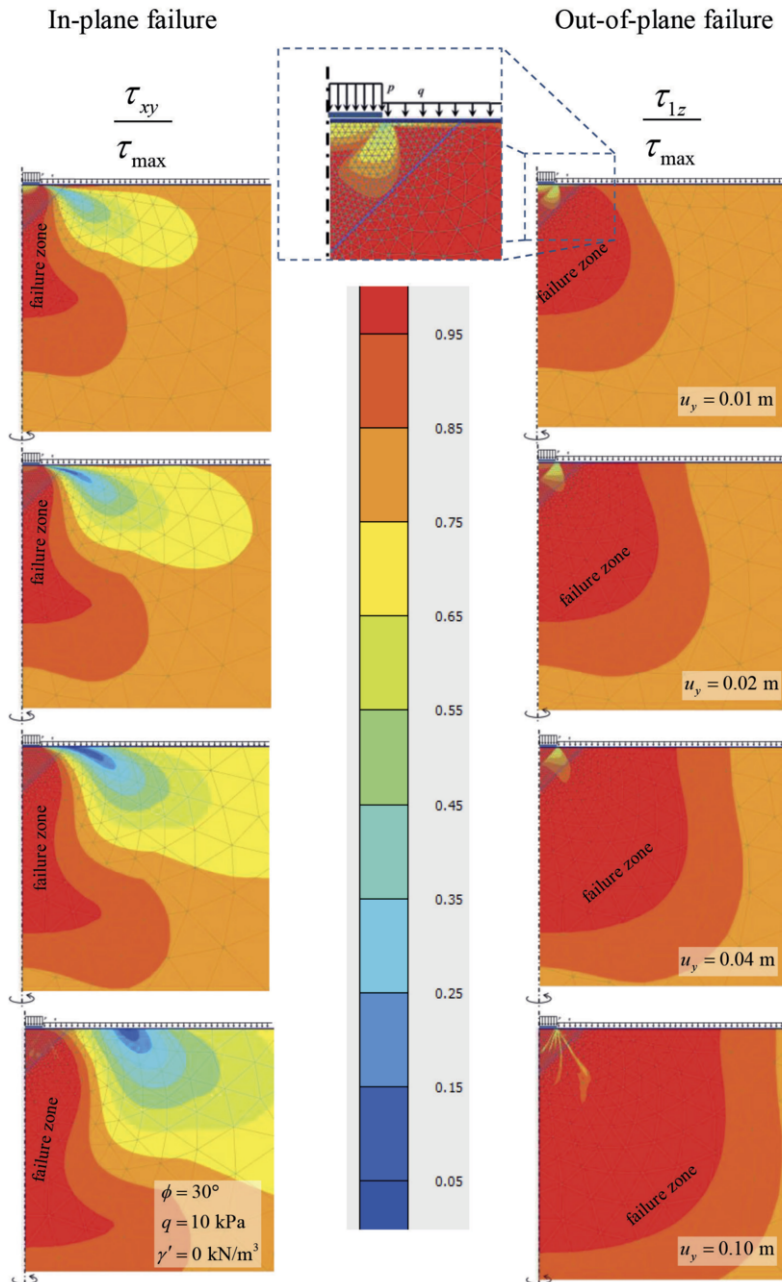


Figure 13-5. Relative shear stress (left: in-plane; right: out-of-plane).

Plaxis 2D does not distinguish between out-of-plane, and in-plane plots for relative stresses. A trick has been used to solve this; the Mohr-Coulomb soil model has been programmed again as a User Defined Soil Model and compiled as a Dynamic Link Library (this is a special tool in Plaxis), but in this case also the relative normal stress ratios and relative shear stress ratios were defined as State Parameters, independently for the out-of-plane and in-plane situations. These can easily be plotted by Plaxis.

Figure 13-5 shows on the left the relative in-plane shear stress τ_{xy} / τ_{\max} , in which τ_{xy} is the radius of the Mohr circle in the x - y plane, and in which τ_{\max} is the maximum allowable radius of a Mohr circle touching the Coulomb envelope. The figure shows on the right the relative out-of-plane shear stress τ_{1z} / τ_{\max} , in which τ_{1z} is the radius of the Mohr circle in the plain of the lowest principal stress (the tangential, circumferential or z -direction) and the highest principal stress (the 1 -direction, which lays somewhere in the x - y plane), and in which τ_{\max} is again the maximum allowable radius of a Mohr circle touching the Coulomb envelope. A value of 1.0 means failure.

This figure shows that there is failure both in and out of the standard x - y plane, but most of the failure is due to out-of-plane failure (the failure zone is much bigger). Therefore this failure mechanism is different from the Prandtl-wedge.

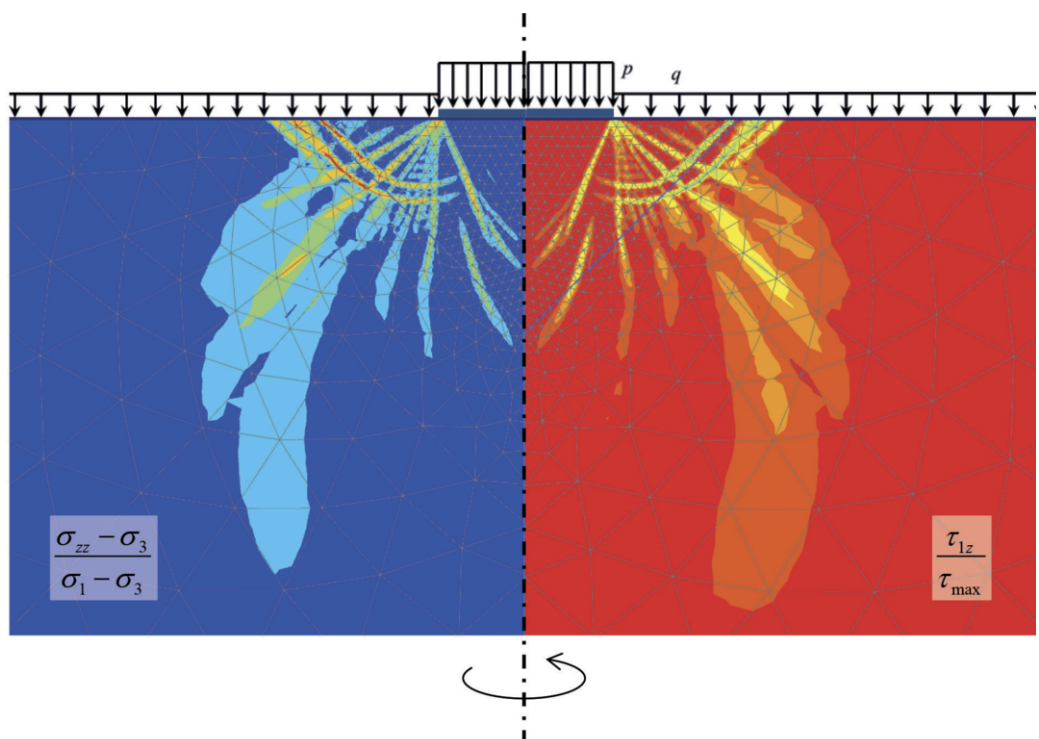


Figure 13-6. Out-of-plane failure: relative tangential stress (left) versus relative shear stress (right).

There are however some similarities between the plane strain (Prandtl-wedge) failure mechanism and the axisymmetric failure mechanism. Figure 13-6 shows on the left the relative tangential (out-of-plane) stress $(\sigma_{zz} - \sigma_3)/(\sigma_1 - \sigma_3)$, and on the right again a detail of the relative out-of-plane shear stress τ_{1z} / τ_{\max} , which indicates the failure zone. Near the loaded circular foundation plate, there are some zones which are not failing. Those are exactly the zones where the tangential stress σ_{zz} is not the same as the lowest principal stress σ_3 . These zones are formed during former internal (in plane) sliding during loading. These sliding zones also form a triangular zone 1 which goes downwards, a circular zone 2 which rotates, and a triangular zone 3 which moves upwards.

The shape factor for a circular footing (s_q for $B = L$) surrounded by a surcharge, has been plotted in Figure 13-7, for Meyerhof, De Beer and also the outcome of the axisymmetric FEM calculations.

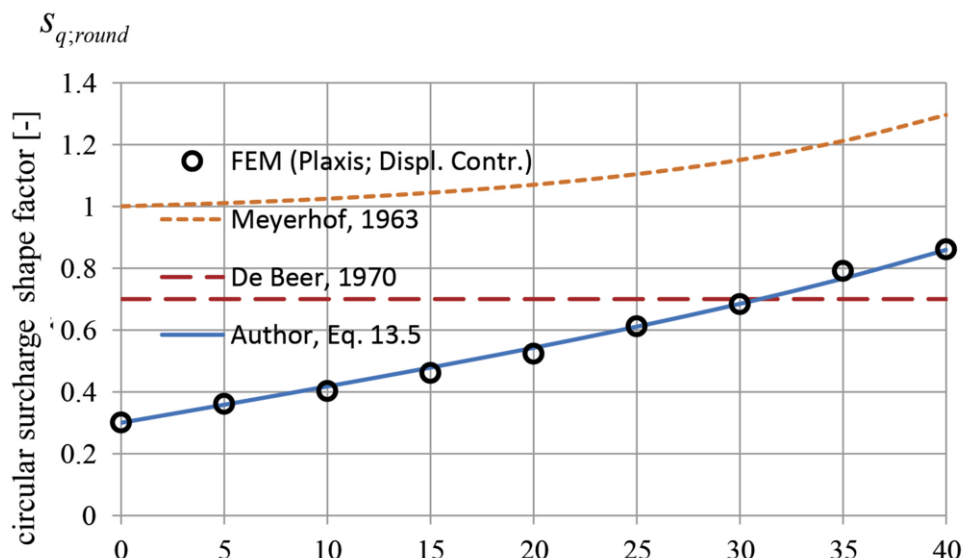


Figure 13-7. The circular surcharge shape factor.

The results show that the currently used factors from Meyerhof in particular, but also from De Beer, are too high, so unsafe. The shape factor used for the straight line is (see Van Baars, 2017a, 2017b, 2018a):

$$s_q = 1 - \left(0.7 - \frac{2}{3} \tan \phi \right) \cdot \sqrt{\frac{B}{L}}. \quad (13.5)$$

13.5 Soil-weight shape factor s_γ

The shape factor for a smooth circular footing (s_γ for $B = L$), on soil with an effective weight, has been plotted in Figure 13-8, for Meyerhof, De Beer and also the outcome of the axisymmetric FEM calculations.

The results show that the currently used factors from Meyerhof in particular, but also from De Beer, are again too high, so unsafe. The shape factor used for the straight line is (see Van Baars, 2017a, 2017b, 2018a):

$$s_\gamma = 1 - \left(0.6 - \exp\left(-\frac{\phi}{4^\circ}\right) \right) \cdot \sqrt{\frac{B}{L}}. \quad (13.6)$$

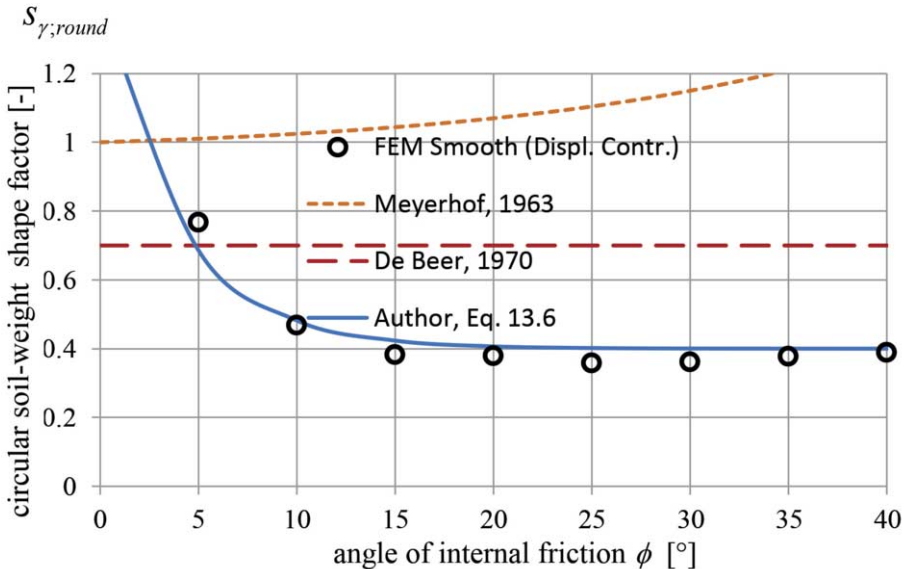


Figure 13-8. The circular soil-weight shape factor.

Figure 13-9 shows, for a circular shallow foundation, with self-weight γ , during displacement controlled failure, the relative shear stresses for both the x - y plane, and also out of this plane, so for a plane including the tangential z -direction, or “out-of-plane” direction. This figure shows, just as for the case with the surcharge q , that there is failure both in and out of the standard x - y plane, but most of the failure is due to out-of-plane failure (the failure zone is much bigger). Therefore this failure mechanism is different from the Prandtl-wedge, although the same applies as for the surcharge loading.

In-plane failure

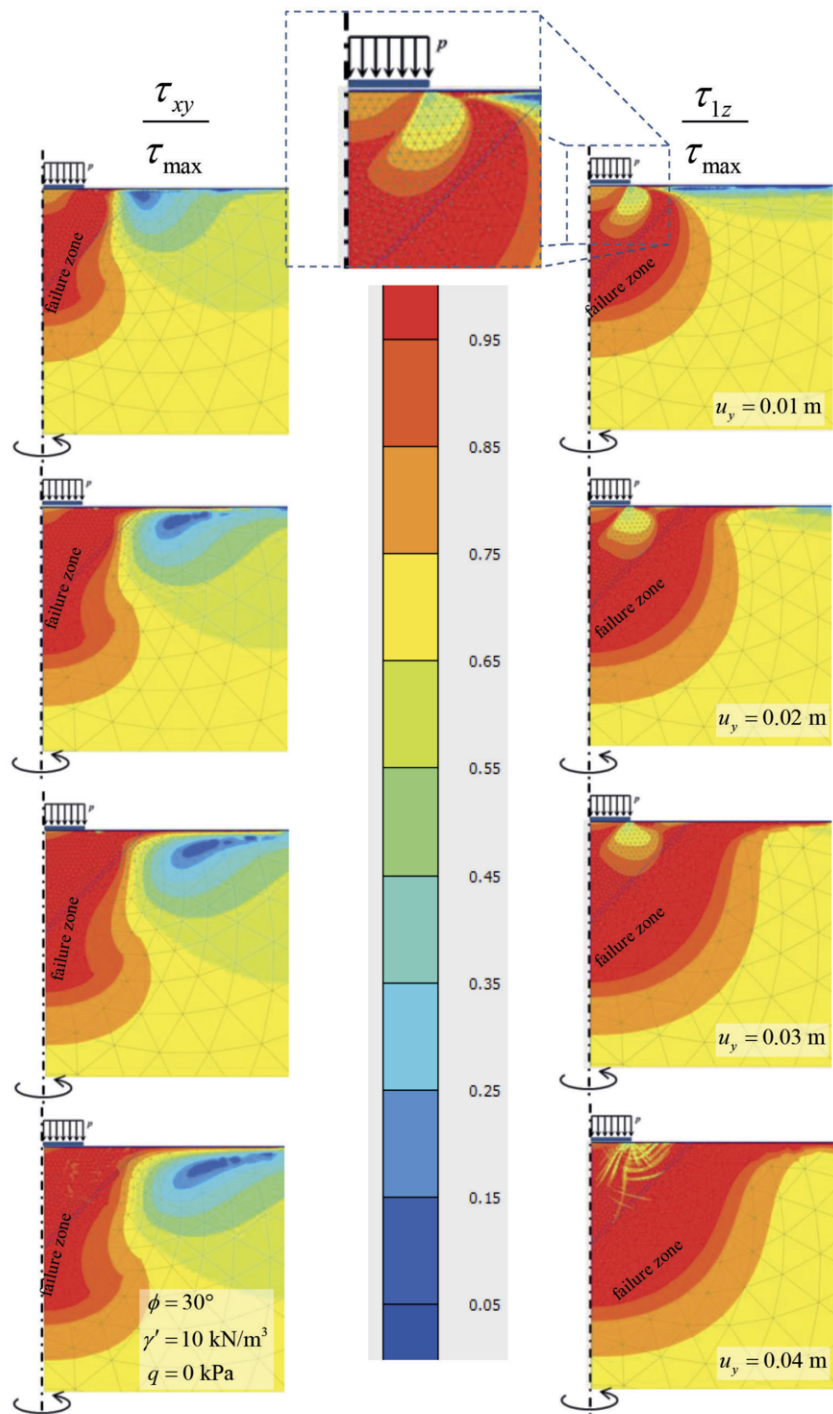


Figure 13-9. Relative shear stress (left: in-plane; right: out-of-plane).

13.6 Superposition of the shape factors

Figure 13-10 shows the results of a single combined calculation in which $c = q = \frac{1}{2}\gamma'D$. Since the failure mechanisms of the three parts (cohesion, surcharge and soil-weight) are identical, superposition is permitted. The prediction based on the shape factors presented in this chapter is good, while the classical equations overestimate the results.

$$s_c N_c + s_q N_q + s_\gamma N_\gamma$$

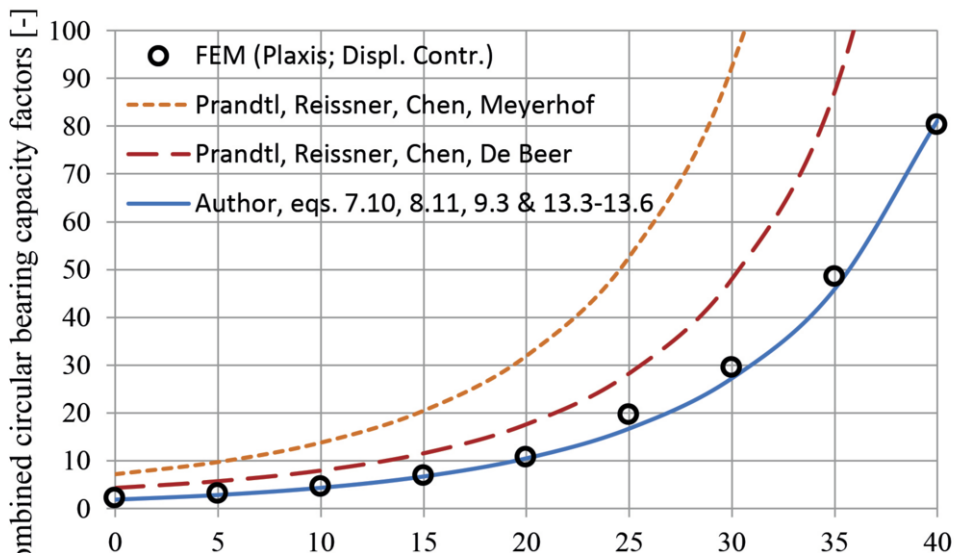


Figure 13-10. The combined circular bearing capacity factors.

14 Eccentric loading

For eccentric loading, no correction factors are used. The common practice is to reduce the contact area of the foundation such that its centroid coincides with that of the load, which means that, the area of the foundation outside the effective area, B' , is completely neglected, see Figure 14-1.

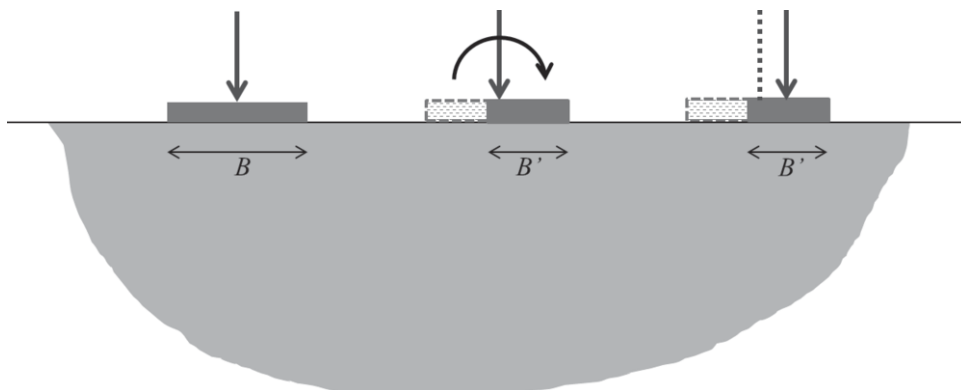


Figure 14-1. Effective or reduced foundation due to eccentric loading.

The question is, whether or not this reduction of the foundation area is an accurate method to describe the reduction of the bearing capacity due to vertical eccentric loading. Several people have performed finite element calculations of vertical and also inclined eccentric loaded strip footings. There can still be some discussion about these results, because Hjiaj et al (2004) based their results on the limit analysis, so the words “dilatancy angle” were not mentioned in their article. Knudsen and Mortensen (2016) and independently Khitas et al (2016) only found results for frictionless soils ($\phi = 0$). They found (only for frictionless soils) that the error of the simplified method, with the reduction of the foundation area, is limited to 5% percent, in case the eccentricity is limited to: $e/B < 0.30$.

In order to check this conclusion, the centric example of Chapter 10.2 (Case I in Figure 14-2) has been extended by Van Baars (2016b). The plate below the loading has been extended with 0.5 m (Case II) and 1.0 m (Case III), in order to create eccentric loading, but without changing the effective area, B' .

Calculations have been made for the three bearing components independently, but also for footings in which the three bearing components are combined such that the three bearing components for cohesion, surcharge and soil weight, are $c = q = \frac{1}{2} \gamma B' = 10 \text{ kPa}$. The friction angle is for all cases $\phi = 30^\circ$.

For the individual bearing components (Figure 14-3) the bearing capacities found for eccentric loading are found to be rather similar to the bearing capacities for centric loading ($N_c = 24.5; N_q = 14.6; N_\gamma = 12.6$). Also for the case with the combined components (Figure 14-4), the bearing capacities found for eccentric loading are almost the same as for centric loading ($N_c + N_q + N_\gamma = 61.0$).

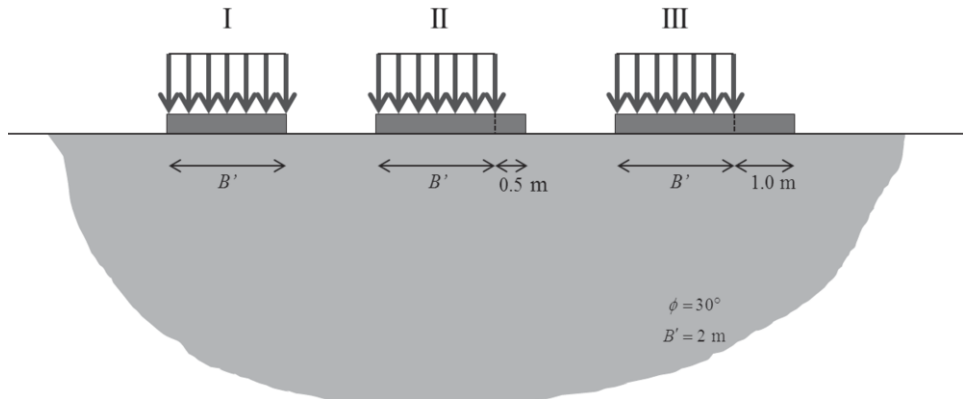


Figure 14-2. Eccentric loading: extension of the footing.

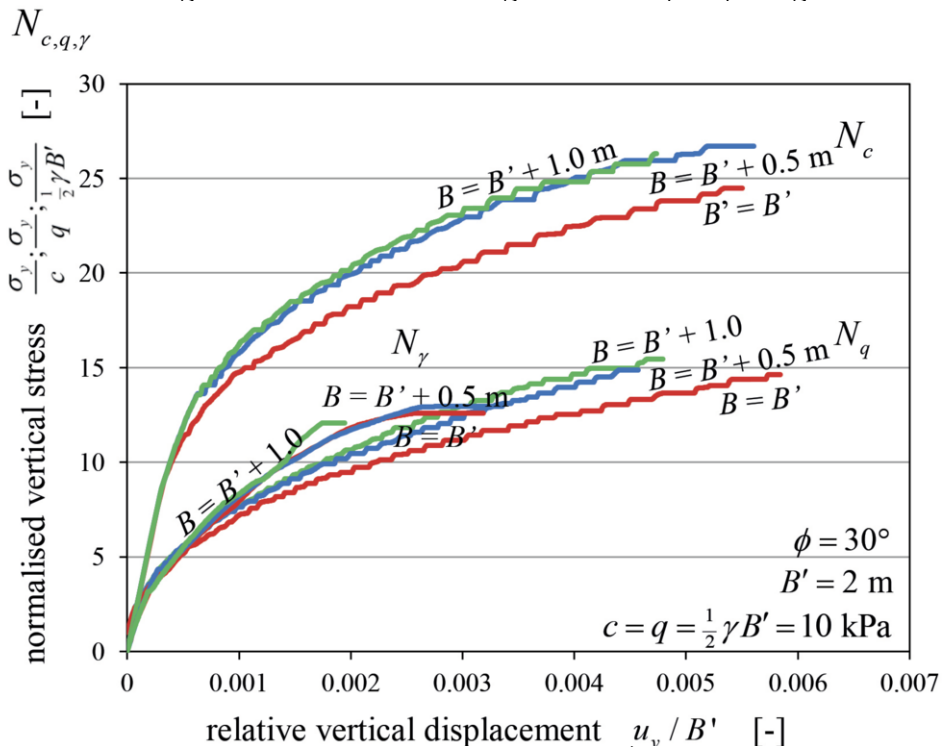


Figure 14-3. Individual components: Normalised stress versus relative displacement.

Figure 14-5 shows the failure mechanism and the plastic zone for both the centric and eccentric load cases (note the different scales and sizes of the plate). The plastic zone is much larger than the failure mechanism, and also rather similar for the three load cases, which means that a change in the failure mechanism (the additional rotation due to the eccentric loading as result of the extension of the plate), has only small consequences on the bearing capacity (i.e. the maximum normalised vertical stress).

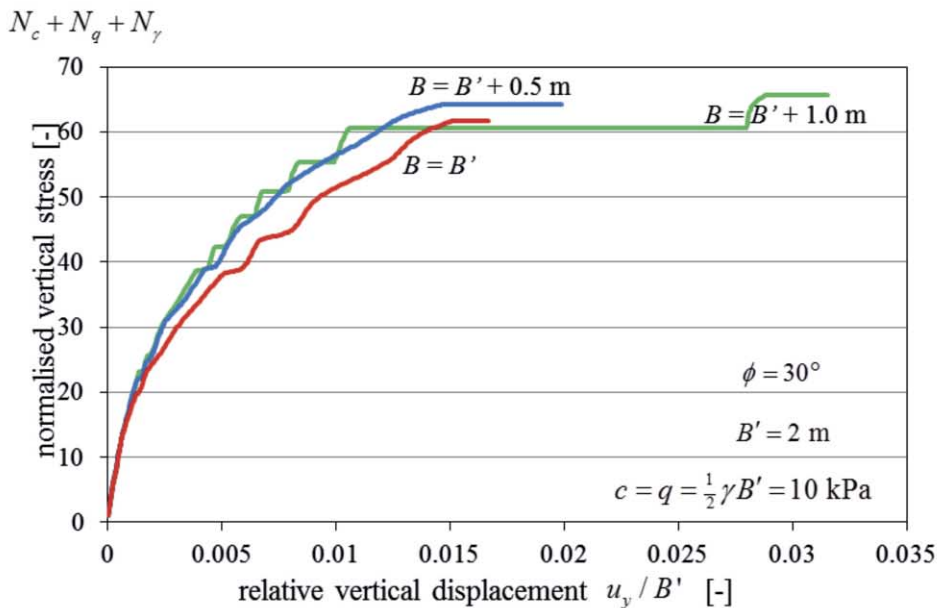


Figure 14-4. Combined components: Normalised stress versus relative displacement.

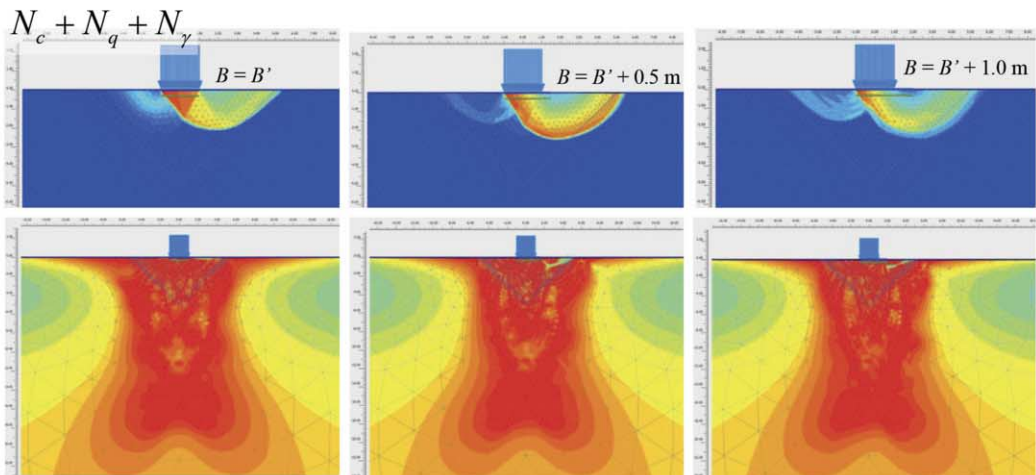


Figure 14-5. Influence of eccentric loaded footing with combined components.
Above: Total displacements at failure (indicating failure mechanism).
Below: Relative shear stress at failure (indicating plastic zone).

Many books and design codes do not only reduce the contact area of the foundation such that its centroid coincides with that of the eccentric load, which means that, the area of the foundation outside the effective area is completely neglected, they also do not allow a gap between the foundation and the soil below the foundation. Under the assumption that the behaviour of the soil below the foundation can be seen as springs with a uniform spring stiffness (which is even for homogeneous soil with a linear elastic stiffness an incorrect assumption), the admissible position of the load is determined to be within the shaded area (1st Core) of Figure 14-6 (Witt, 2018).

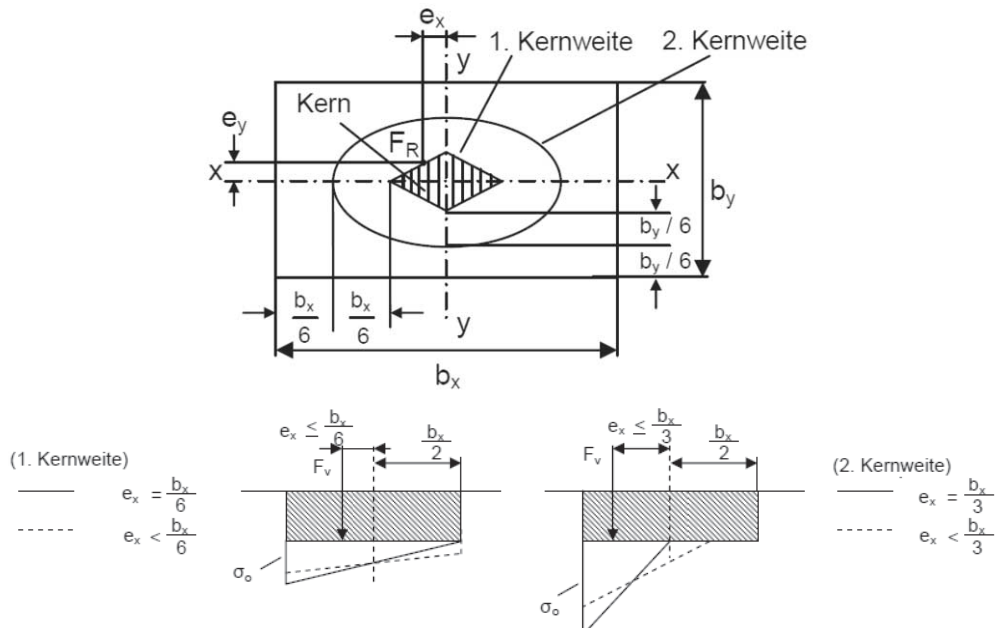


Figure 14-6. Admissible position of the load for eccentric loaded footings.

According to the German norm for shallow foundations (DIN 1054), a gap between the foundation and the soil below the foundation is allowed, as long as the gap is not passing the centre of the foundation. Since there is no good reason for this rule, this is of course rather arbitrary. This rule leads to a larger area, which is called the 2nd Core. Under the same assumption of uniform springs, the 2nd Core can be found. The following equation of an ellipse:

$$\left(\frac{e_{2^{nd}C,x}}{b_x}\right)^2 + \left(\frac{e_{2^{nd}C,y}}{b_y}\right)^2 = \left(\frac{1}{3}\right)^2, \quad (14.1)$$

describes, up to 4% accuracy, this 2nd Core for rectangular foundation.

15 Slope factors

15.1 Meyerhof and Vesic

Shallow foundations also exist in or near a slope, for example the foundation of a house or a bridge.



Figure 15-1. Footing of a house or bridge near a slope.

In 1957, Meyerhof was the first to publish an article about the bearing capacity of foundations on a slope. He wrote: “*Foundations are sometimes built on sloping sites or near the top edge of a slope.....When a foundation located on the face of a slope is loaded to failure, the zones of plastic flow in the soil on the side of the slope are smaller than those of a similar foundation on level ground and the ultimate bearing capacity is correspondingly reduced*”.

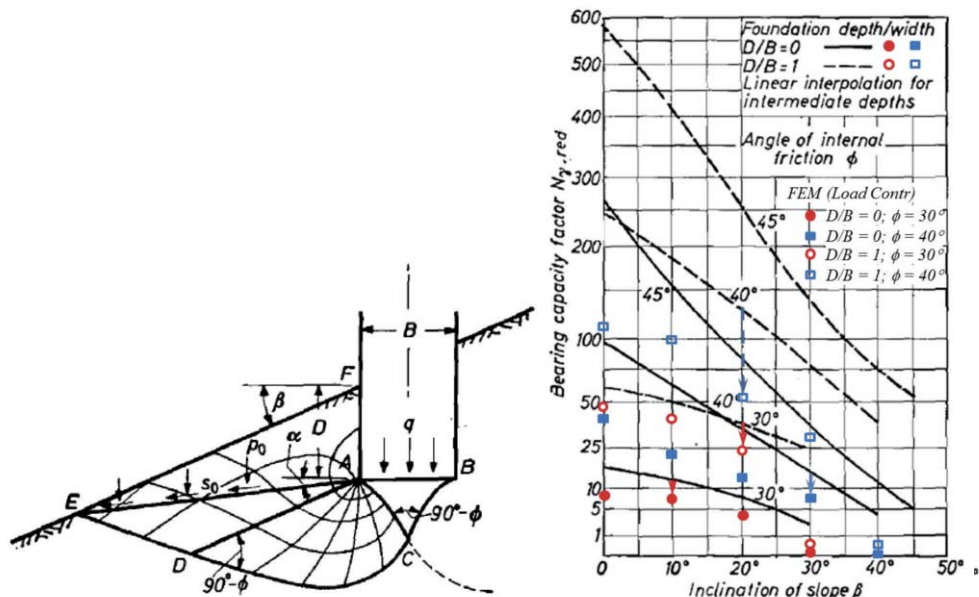


Figure 15-2. Left: failure mechanism of a footing in a slope,
Right: reduced bearing capacity factors (according Meyerhof, 1957).

Meyerhof published a failure mechanism of a footing in a slope with angle β (see Figure 15-2 on the left) and introduced figures with reduced bearing capacity factors (see Figure 15-2 on the right), but the problems with these figures are:

- it is unclear if the figures are based on non-associated flow behaviour, or not,
- the figures are not explained and cannot be verified,
- the figures are only for purely cohesive or purely frictional soil,
- the important angle α (see line EA in the figure on the left) is never solved,
- the slope bearing capacity does not go to “0” for $\beta = \phi$, and
- the reduced bearing capacity factors of Meyerhof are too high according to the results of Finite Element Model (FEM load controlled) calculations, made for this chapter (see the added points in the figure of Meyerhof).

Brinch Hansen (1970) also worked on the influence of the slope. Vesic (1975) combined the work of Meyerhof and Brinch Hansen and proposed for the following bearing capacity equation:

$$p = \lambda_c c N_c + \lambda_q q N_q + \lambda_\gamma \frac{1}{2} \gamma B N_\gamma, \quad (15.1)$$

the following slope factors:

$$\begin{aligned} \lambda_c &= \frac{N_q \lambda_q - 1}{N_q - 1} \quad (\phi > 0), \quad \text{or undrained: } \lambda_c = 1 - \frac{2\beta}{\pi + 2} \quad (\phi = 0) \\ \lambda_q &= \lambda_\gamma = (1 - \tan \beta)^2. \end{aligned} \quad (15.2)$$

The angles in these equations are in radians.

It is remarkable, if not to say impossible, that these slope factors do not depend on the friction angle, and that the surcharge slope factor and the soil-weight slope factor are identical. Another mistake is that the cohesion slope factor γ_c is solved, based on the assumption that the equation for the cohesion bearing capacity ($N_c = (N_q - 1)\cot \phi$) is also valid for inclined loading (see chapter 12.1) and for loading near a slope ($\gamma_c N_c = (\gamma_q N_q - 1)\cot \phi$). This assumption was published first by De Beer and Ladanyi (1961). Vesic (1975) calls this “*the theorem of correspondence*”, and Bolton (1979) calls this “*the usual trick*”, which is still used today (Ip, 2005). This relation between N_c and N_q is coincidentally valid for vertical ultimate loads without a slope. However, according to the results of the numerical calculations, and also according to the analytical solution given later in this chapter, the assumption that this is also the case for inclined loading and loading near a slope is not correct. This indicates that not only the inclination factors, but also the slope factors proposed by Vesic, are incorrect and should not be used.

15.2 Modern research and German norms

Over the years many people have published articles about the bearing capacity of footings on a slope. However, these articles are mostly limited to purely cohesive slopes (Azzouz and Baligh, 1983; Graham et al., 1988, Georgiadis, 2010, Shiau et al

(2011) or purely non-cohesive slopes (Grahams et al., 1988), or slopes in a geotechnical centrifuge (Shields et al. 1990), or complex slopes with reinforced soil (Alamshahi and Hataf, 2009; Choudhary et al., 2010), or slopes with seismicity (Kumar and Rao, 2003; Yamamoto, 2010), or slopes with 3D load cases (Michalowski, 1989; De Butan and Garnier, 1998). Meanwhile the simpler non-seismic, non-reinforced, 2D situation is still not fully understood.

In 2013, Chakraborty and Kumar (2013) and were one of the first to make a more general study. Unfortunately, like most researchers, they only used the lower bound finite element limit analysis in conjunction with a non-linear optimisation. In addition, they did not discuss the slope correction factors. The same applies to Leshchinsky (2015), who used an upper-bound limit state plasticity failure discretisation scheme.

The most widely used slope correction factors today, are the following slope correction factors (in German: Geländeneigungsbeiwert) mentioned in the German norm (in fact the German Annex to Eurocode 7 “Geotechnical Engineering”):

$$\begin{aligned}\lambda_c &= \frac{N_q e^{-\alpha}}{N_q - 1} \quad (\phi > 0), \quad \text{or undrained: } \lambda_c = 1 - 0.4 \tan \beta \quad (\phi = 0) \\ \lambda_q &= (1 - \tan \beta)^{1.9}, \\ \lambda_y &= (1 - 0.5 \tan \beta)^6,\end{aligned}\tag{15.3}$$

in which:

$$\alpha = 0.0349 \cdot \beta \cdot \tan \phi.$$

The angles in these equations are in degrees and to avoid slope failure: $\beta \leq \phi$.

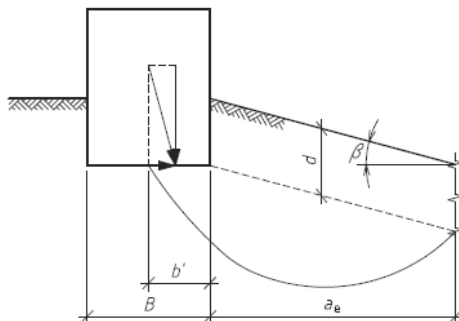


Figure 15-3. Footing near a long slope.

The fact that these factors are presented in the German design norm without references or any background information is a major problem. Nevertheless, it is clear, due to the similarities, that these factors relate to the factors of Vesic. Besides, it is remarkable, that in the German norm, neither the surcharge slope factor nor the soil-weight slope factor depend on the friction angle.

Considering these problems, the next chapters will feature a comparison between the results of Finite Element calculations and the results of the German norm, the results

of Bishop slip circle calculations (with the program “GEO5” from “Fine Civil Engineering Software”) and also, for the cohesion slope factor λ_c , the results of an analytical solution.

15.3 Cohesion slope factor λ_c

For two different friction angles ($\phi = 0^\circ, 30^\circ$) and four different slope angles ($\beta = 0^\circ, 10^\circ, 20^\circ, 30^\circ$), the failure mechanism for a cohesive ($c = 10 \text{ kPa}$), weightless ($\gamma' = 0 \text{ kN/m}^3$) soil has been calculated with FEM and compared with the Prandtl failure mechanism, see Figure 15-4.

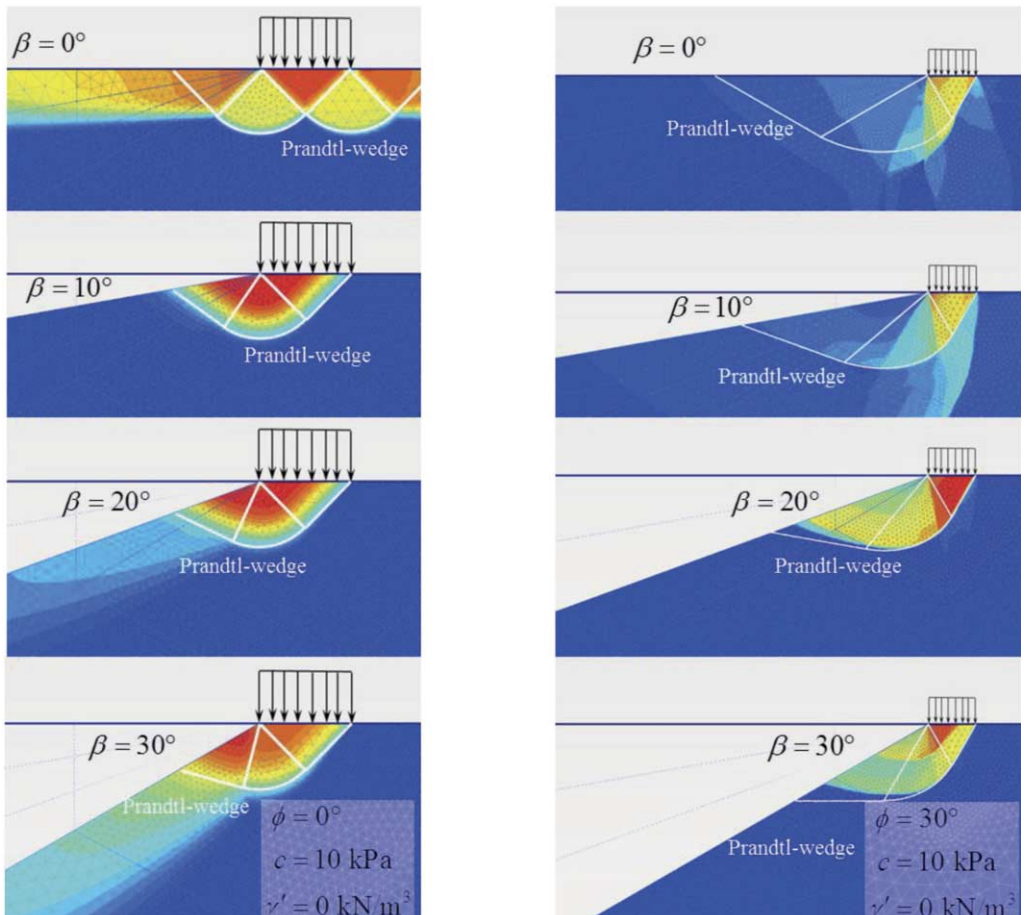


Figure 15-4. Failure mechanism: Prandtl-wedge versus FEM.
(Incremental displacement plots.)

This figure shows that in general, the failure mechanism can be well described by a Prandtl-wedge with a reduced Zone 2 (the logarithmic spiral wedge).

By reducing the effect of Zone 2 in a similar way as for the cohesion inclination factor i_c in Chapter 12.5 (Van Baars, 2014, 2018a), it is also possible to derive an analytical solution for the cohesion slope factor (Van Baars 2018a, 2018b):

$$\lambda_c = \cos \beta \cdot \left(e^{-2\beta \tan \phi} - \frac{2\beta}{2 + \pi} \cdot e^{-\pi \tan \phi} \right) \quad \beta \leq \phi. \quad (15.4)$$

The results of this analytical solution, the German norm and the Bishop's slip circle method have been plotted in Figure 15-5, together with the results from the Finite Element calculations.

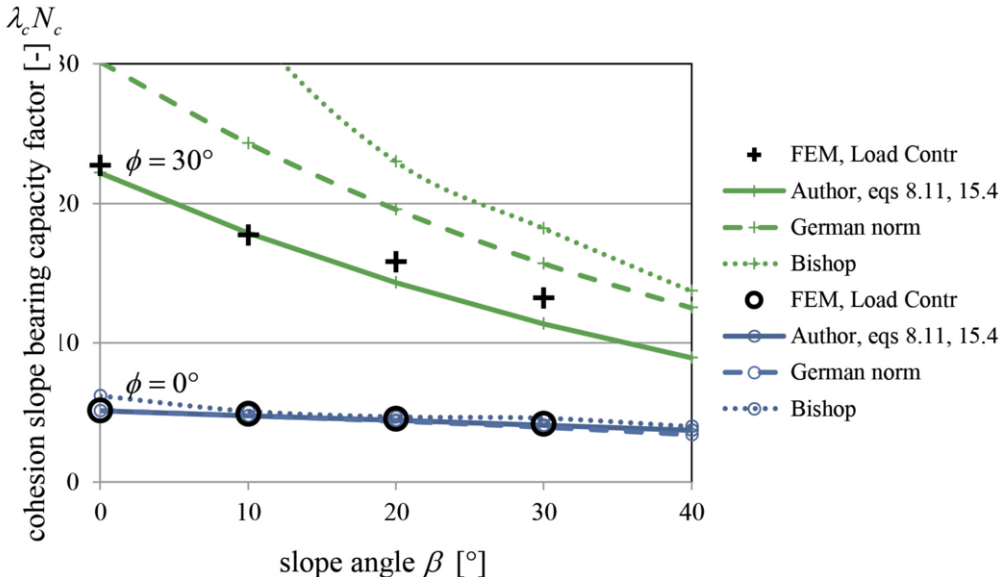


Figure 15-5. Cohesion slope factor:
Analytical solution, German norm and Bishop versus FEM.

This figure shows that the Bishop calculations are only correct for a zero friction angle. The analytical solution functions very well. The German norm would have functioned just as well, if not the Prandtl solution for large dilatancy (Equation 8.10), but the solution for zero dilatancy (Equation 8.11), would have been used. The reason for this is because:

$$\cos \beta \cdot \left(e^{-2\beta \tan \phi} - \frac{2\beta}{2 + \pi} \cdot e^{-\pi \tan \phi} \right) \approx \frac{N_q e^{-0.0349 \cdot \beta \cdot \tan \phi} - 1}{N_q - 1}. \quad (15.5)$$

15.4 Soil-weight slope factor λ_s

A mistake which can be found in the publication of Meyerhof (1957), but also in many recent publications, is the assumption that the failure mechanism in a purely frictional soil (N_s), is a (reduced) Prandtl-wedge. According to Chapter 9 however, this is not the case. As an example, Figure 15-6, which is a plot of the incremental displacements of FEM calculations, indicates the difference between the failure mechanism and the reduced Prandtl-wedge for purely frictional soil.

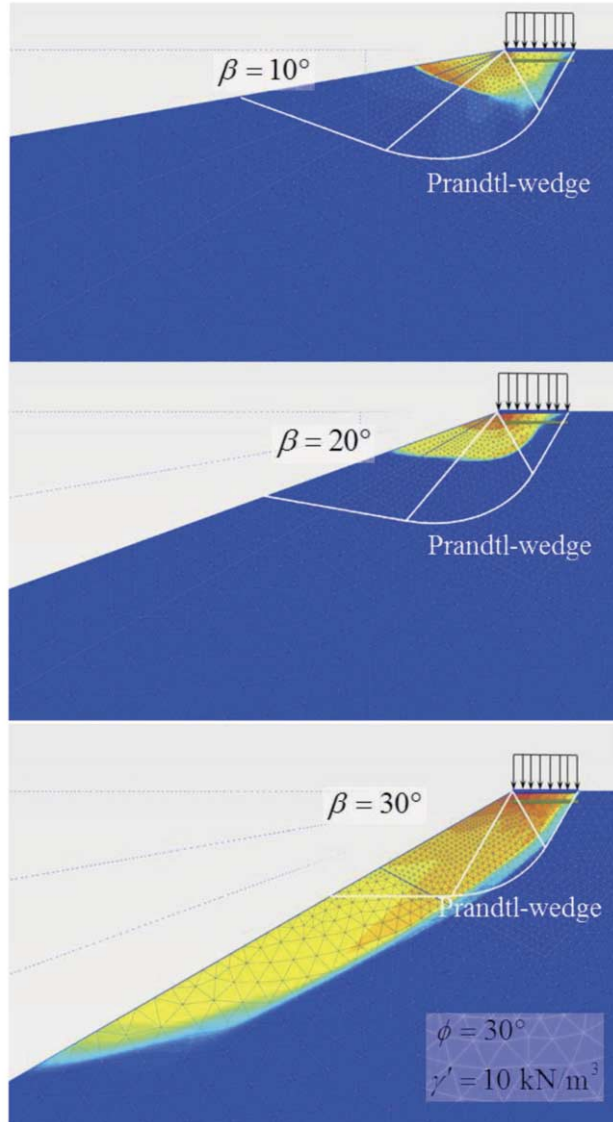


*Figure 15-6. Failure mechanism: Prandtl-wedge versus FEM.
(Incremental displacement plots.)*

As a result, it is not possible to derive the soil-weight slope factor λ_γ , in a similar way as for the cohesion slope factor λ_c . Although, a simple approximation can easily be made, for example (Van Baars 2018a, 2018b):

$$\lambda_\gamma = 1 - \left(\frac{\beta}{\phi} \right)^{2/3} \quad \beta \leq \phi. \quad (15.6)$$

The results of this equation, the German norm and the Bishop's slip circle method have been plotted in Figure 15-7, together with the results from the Finite Element calculations.

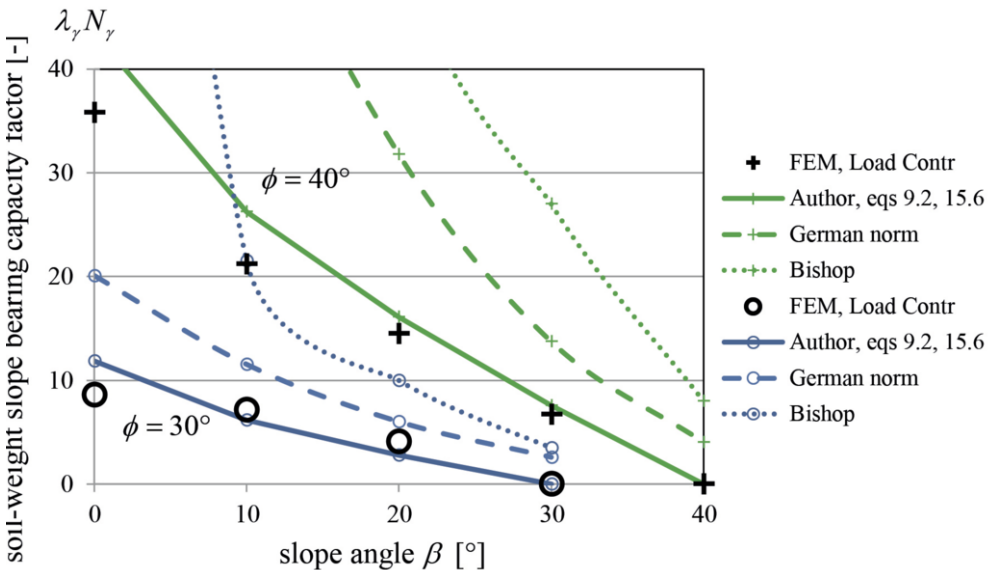


Figure 15-7. Soil-weight slope factor:
Approximation, German norm and Bishop versus FEM.

This figure shows that the analytical approximation functions reasonably well. The German norm does not fit. The Bishop calculations do not fit at all. An important reason for this is the fact that the slip circle in the Bishop calculations has been forced not to cross the foundation plate, while the FEM calculations (Figure 15-6) show that the soil slides somewhere below the plate (see especially for $\beta = 20^\circ$), which causes the plate to tumble over. This tumbling failure mechanism however, is not part of the Bishop calculation method.

15.5 Surcharge slope factor λ_q

In order to see the influence of having a shallow solid footing, additional finite element calculations have been made for a relative depth of $D/B = 1$. This relative depth creates an additional bearing capacity mostly due to the surcharge of $q = \gamma' \cdot D$, but also due to a larger slip surface, of which the influence is difficult to quantify. Plots of the incremental displacements of the FEM calculations, indicating the failure mechanism, show that the failure mechanism of a shallow foundation in a frictional soil with self-weight, is a sort of extended Prandtl-wedge, see Figure 15-8.

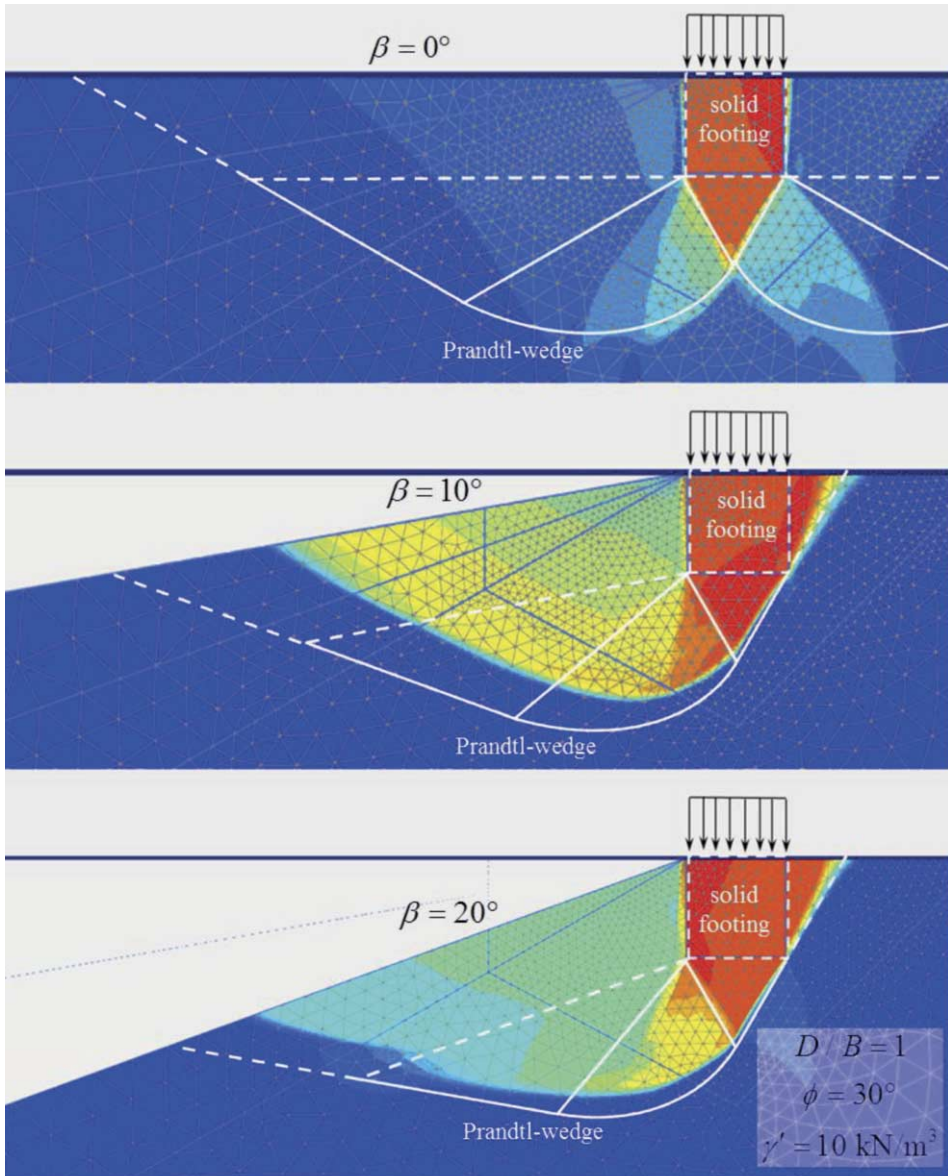


Figure 15-8. Failure mechanism: Prandtl-wedge versus FEM.
(Incremental displacement plots.)

Since Figure 15-8 shows that in this case the Prandtl-wedge aptly describes a part of the failure mechanism, one could be tempted to derive an analytical solution for the surcharge slope factor, by only reducing the logarithmic spiral, in a similar way as in Chapter 7.1. This would give the following surcharge slope factor:

$$\lambda_q = e^{-2\beta \tan \phi} \quad \beta \leq \phi, \quad (15.7)$$

which is the same equation for the surcharge slope factor as the one proposed by Ip (2005). This solution is however incorrect, since:

- it neglects the extension (dashed lines) due to the depth, and

- the surcharge slope factor is not “0” for $\beta = \phi$, which is the same problem as for the slope factors of Meyerhof in Figure 15-2.

It is therefore better to make a simple approximation for the surcharge slope factor λ_q , for example (Van Baars 2018a, 2018b):

$$\lambda_q = 1 - \left(\frac{\beta}{\phi} \right)^{3/2} \quad \beta \leq \phi. \quad (15.8)$$

The results of this equation, the German norm and the Bishop’s slip circle method have been plotted in Figure 15-9, together with the results from the Finite Element calculations.

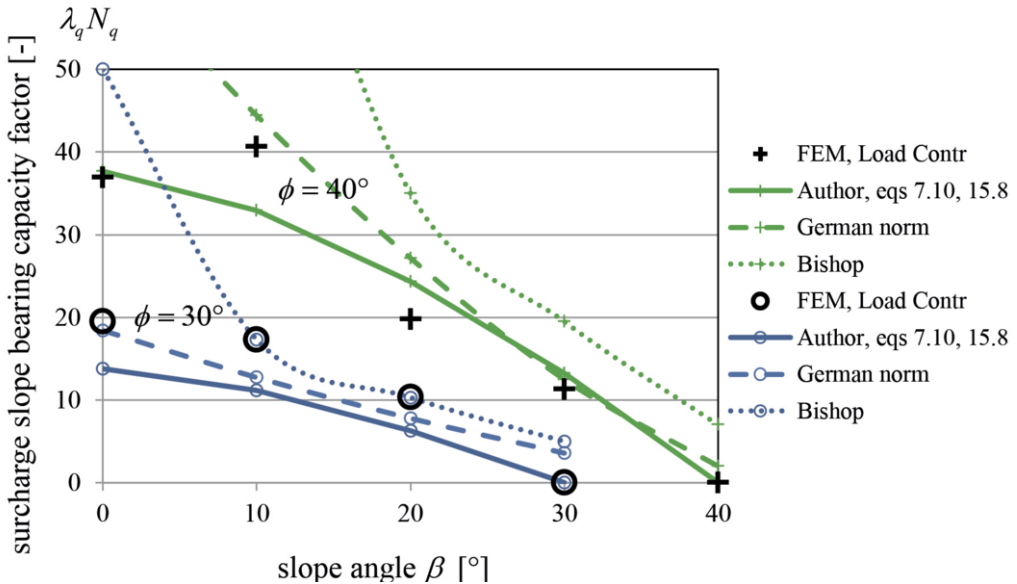


Figure 15-9. Surcharge slope factor:
Approximation, German norm and Bishop versus FEM.

This figure shows that, for the surcharge slope factor, the Bishop calculations fit steeper slopes much better, but not gentle slopes. The German design norm and especially the analytical approximation function reasonably well.

16 Inclined footing factors

In the German norms, even the reduction factor for the case of an inclination of the footing can be found (in German: Sohlneigungsbeiwert), which is a rather rare case. This relates to page 307 of the publication of Reissner.

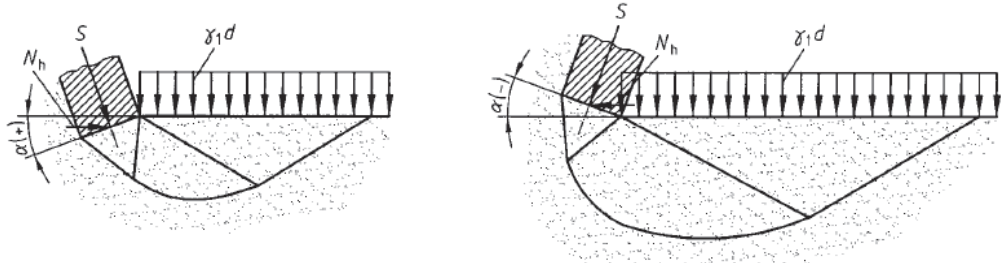


Figure 16-1. Inclined footings.

According to the German norms the reduction factors are:

$$\xi_c = \xi_q = \xi_\gamma = e^{-0.045\alpha \tan \phi} \quad (\phi > 0). \quad (16.1)$$

It is unclear where these reduction factors come from, and moreover, it is rather implausible that all three factors are the same. Therefore, if one ever has to design an inclined footing, which is unlikely, it is probably better not to use these reduction factors, but to apply the solution of the inclined loads as given in Chapter 12.

17 Special footings

17.1 Perforated footings

In their article about the “*Undrained vertical bearing capacity of perforated shallow foundations*”, Tapper et al. (2015) published something new: the perforation shape factor. They wrote:

“*Perforated shallow foundations are commonly used as mudmats to support subsea infrastructure such as pipeline end manifolds and terminations. The perforations may be included in the foundation design to allow water to escape during installation, or to reduce uplift resistance on decommissioning. Perforated geometries, often involving a single perforation, can also be efficient for larger gravity-based foundations. However, perforations decrease the available foundation bearing area, which reduces the capacity of the foundation during operation.*”

The authors studied the effect of the perforation (Figure 17-1) on the bearing capacity of a shallow foundation on cohesive material, by using centrifuge tests and numerical simulations (Figure 17-2).

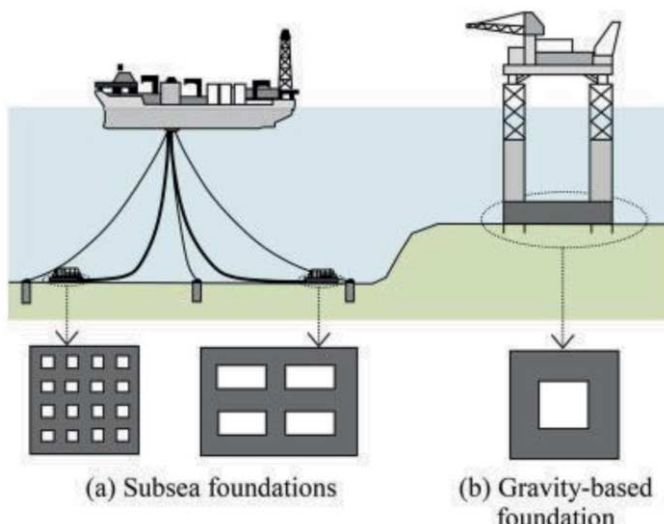


Figure 17-1. Perforated offshore foundation examples (Tapper et al., 2015).

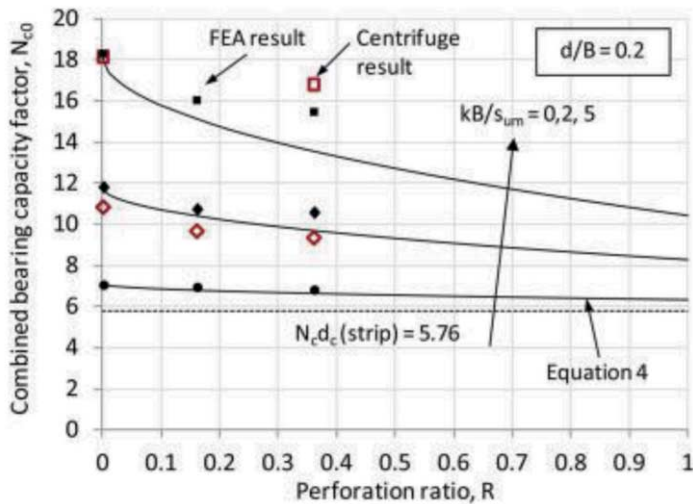


Figure 17-2. Square perforated footing capacity ($d/B=0.2$) (Tapper et al., 2015).

In their plots of the numerical simulations, one can recognise the Prandtl-wedges (Figure 17-3).

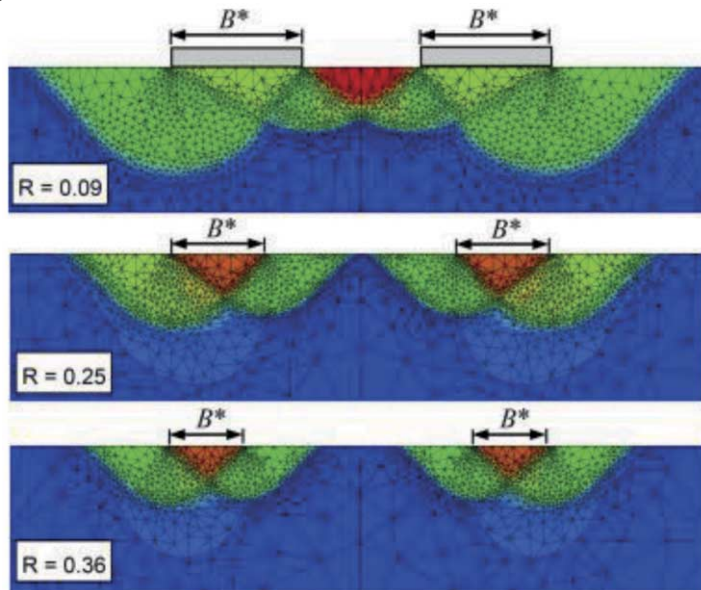


Figure 17-3. Transition of failure mechanisms (Tapper et al., 2015).

17.2 Shell footings

Instead of changing the size of the footing, changing the cross section of the footing (more hollow/shell shaped) can lead to a higher bearing capacity, and also to a higher stiffness behaviour. An interesting article on this topic comes from Rinaldi et al. (2017). They performed laboratory tests and numerical calculations on a set of different types of shell shaped footings and compared their results with the results of a flat footing (Figure 17-4).



Figure 17-4. Shell footings (Rinaldi et al., 2017).

Their laboratory tests and numerical calculations show that having a shell shaped footing strongly increases the stiffness behaviour and bearing capacity (Figure 17-5).

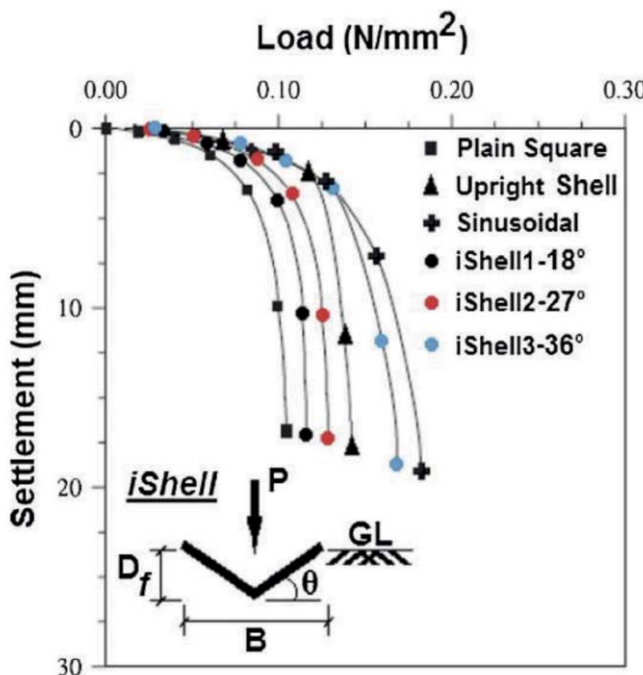


Figure 17-5. Load-settlement curves of the shell footings (Rinaldi et al., 2017).

17.3 Footings on layered soil and punching

In the previous chapters, the bearing capacity has only been studied on a homogeneous soil layer. However, in reality footings are mostly founded on a layered soil. In case of a thin soft soil layer on top of a strong soil layer, the soft soil layer can be replaced by a new strong soil layer, or the footing can be extended to the depth of the deeper strong soil layer. In case of a thick soft soil layer, mostly pile foundations are used. But the case of a strong soil layer on top of a soft soil layer is quite different. The thinner the strong soil layer on top, the lower the bearing capacity, and the higher the risk of a punching footing. This has been modelled with Plaxis. The width of the footing is as before $B = 2$ m. The results can be found in Figure 17-6 and Figure 17-7. The strength parameters of both soil layers are given in the last figure.

Figure 17-6 shows that the thicker the strong top layer, the higher the bearing capacity, but first when the thickness of the strong top layer is about $D = 6B$, the bearing capacity reaches a maximum, and the effect of the softer layer can be ignored. It seems that the bearing capacity of a footing on a thin strong soil layer can be estimated by a linear interpolation between the bearing capacity of a pure soft layer (in this case clay) and the bearing capacity of a pure strong layer (in this case sand), based on the thickness of the strong top layer D and the width of the footing B .

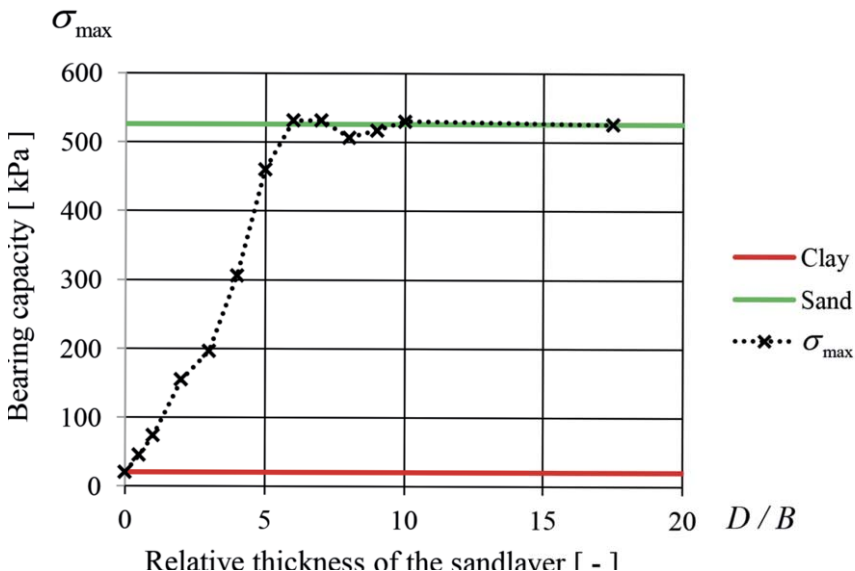


Figure 17-6. Bearing capacity versus the thickness of the top sand layer.

Figure 17-7 shows, for a thin strong top layer of $D = 1B$ (left above), until a complete homogeneous strong subsoil (right below), the incremental displacements, indicating the corresponding failure mechanisms. In the calculations, there is a surcharge next to the footing ($q = 10$ kPa), which is not shown in the figure. A large rotating and punching failure mechanism can be seen (on the left) until a thickness of the top layer of $D = 6B$, from this thickness on, a more local, Prandtl-wedge type of failure can be found (on the right).

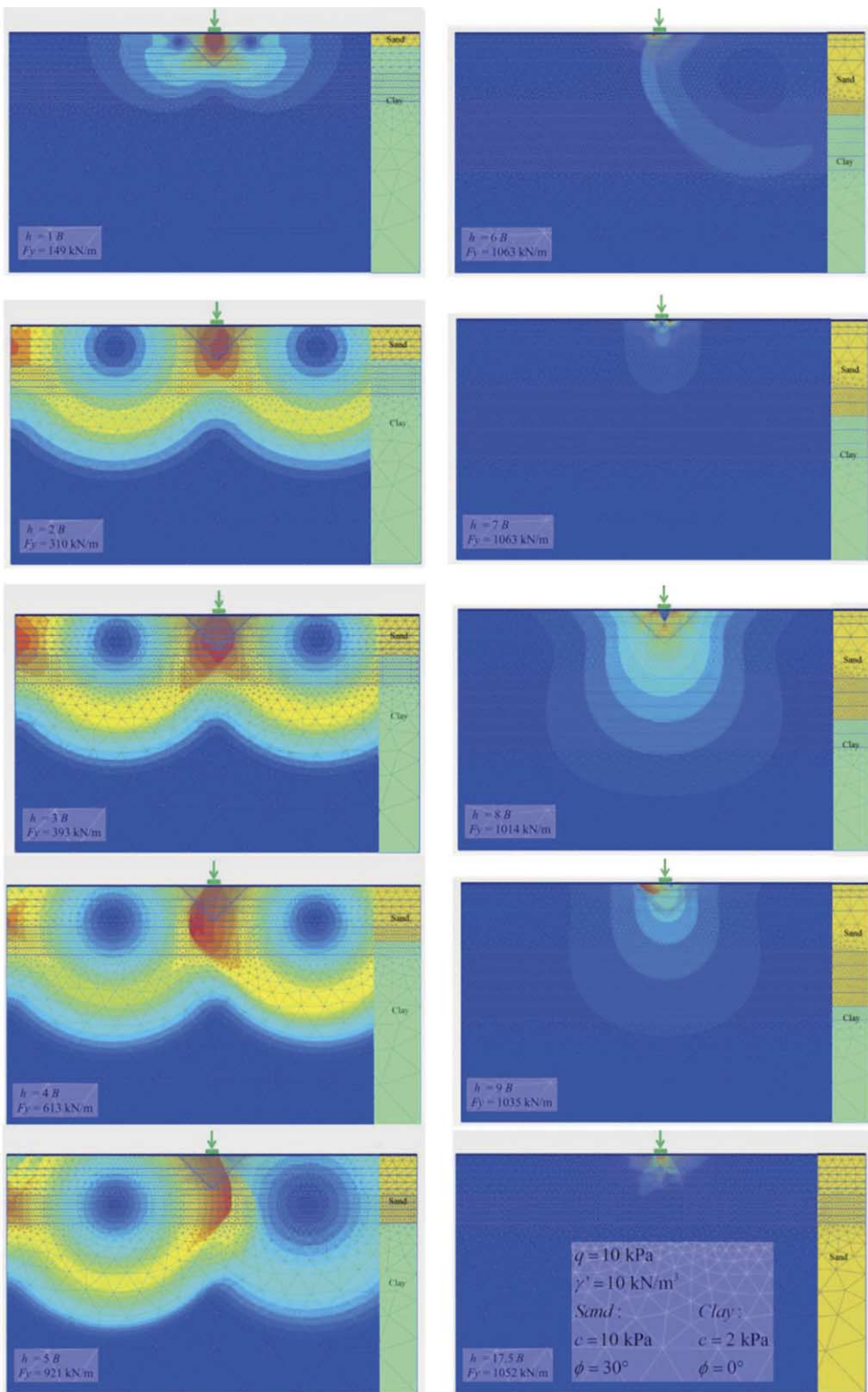


Figure 17-7. Failure mechanism in layered soil (Punching versus Prandtl-wedge).

V Pile tip bearing capacity

18 Pile tip bearing capacity using Meyerhof

The first to apply the Prandtl-wedge for pile foundations were Keverling Buisman (1935, 1940) and Meyerhof (1951), but they forgot about the shape factors, which were first published by Meyerhof in 1963.

In order to determine the bearing capacity of the tip of a foundation pile, often the general bearing capacity formula of Meyerhof is used. In this analysis the basic parameters are the shear strength of the soil below the pile tip (characterised by its cohesion c and its friction angle ϕ), and the weight of the soil surrounding the pile shaft, which is taken into account as a surcharge q .

The maximum tip bearing capacity is determined analogously to the bearing capacity of a shallow foundation, which is based on the Prandtl-wedge. This entails simply using the 2-dimensional solution of a shallow foundation, multiplied with shape factors for a 3-dimensional failure mechanism, and simply disregarding the shear strength (but not the weight) of the soil above the foundation plane, see Figure 18-1.

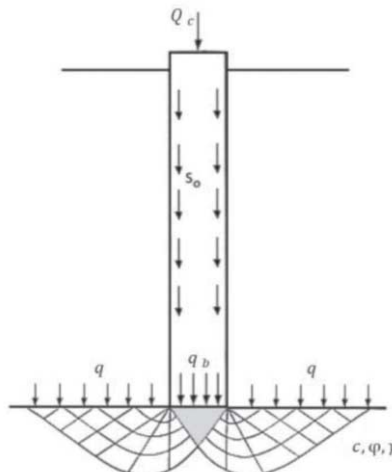


Figure 18-1. Prandtl-wedge failure under a pile tip (Meyerhof, 1951).

In this case, at a certain depth, the term of the soil-weight in the Meyerhof equation can be neglected and for sand the cohesion term is zero, so only the surcharge term remains. Figure 18-2 shows a figure published by Vesic (1967) and republished by Fang (1990). It shows the surcharge bearing capacity factor for shallow round footings $S_{q;round} \cdot N_q$ according to several researchers. The solution of the author (Van Baars, 2014), based on this 3-dimensional Prandtl-wedge failure mechanism (see Figure 13-2), is added to this figure. This solution can be approximated by:

$$S_{q;round} \cdot N_q = e^{2\pi \tan \phi} \quad (18.1)$$

This solution is somewhat in the middle of the other results. The interesting point is that this solution is close to the Berezantsev solution, because Fang (1990) writes: “Of the values shown in the figure, those of Berezantsev et al (1961), are considered to be

the most reliable (Norland, 1963; Vesic, 1965; Tomlinson, 1977; Canadian Foundation Engineering Manual (CFEM), 1978)".

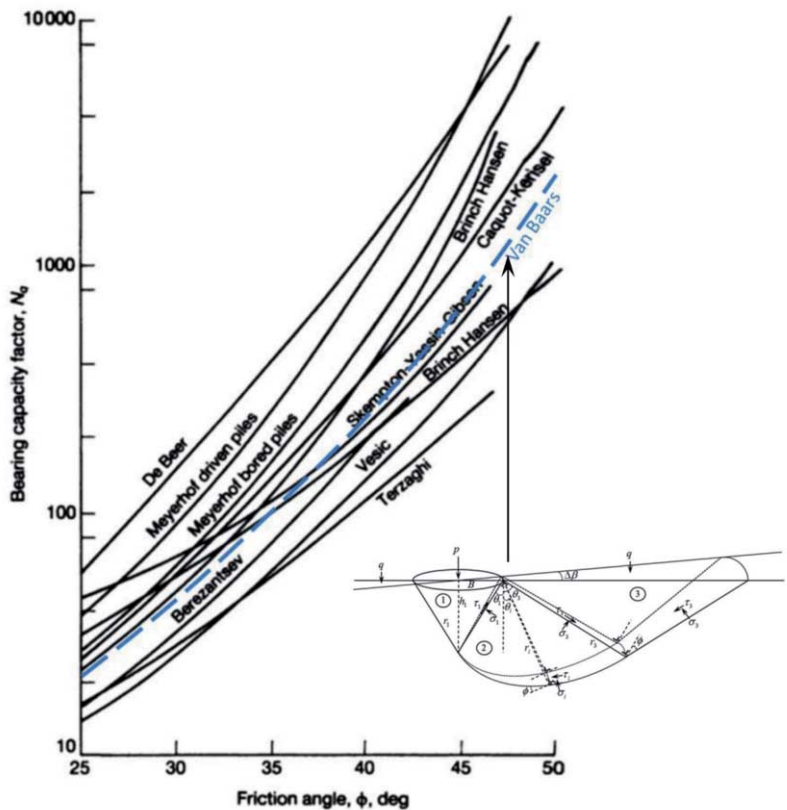


Figure 18-2. Comparison of the surcharge shape factor for round loads $S_{q,round} \cdot N_q$ (By Vesic, 1967 and Fang, 1990).

The problem with such an approach is that there is in fact no real failure mechanism possible all the way to the surface as occurs with the Prandtl-wedge failure mechanism for shallow foundations. As a consequence, the whole failure mechanism in the ground higher than the pile tip is neglected. This can make this method conservative. On the other hand this method neglects the failure mechanism occurring for the shallow foundations, which is failure due to a tangential stress, or circumferential stress, going to zero.

If one uses the Meyerhof equation for shallow foundations, with its shape factor and surcharge bearing capacity factor, for calculating the bearing capacity of a pile, and not Equation 18.1, then for certain a far too low bearing capacity will be found.

The reason why these methods are still so frequently used, is that the only better alternative; the use of Cone Penetration Test (CPT) based methods, is not always possible. CPT's cannot be made in all cases, for example when the soil is too strong, or when there are too many large stones in the soil.

19 Pile tip bearing capacity, CPT and failure mechanism

Meyerhof (1951) also proposed a failure mechanism around the pile tip, which is a sort of Prandtl-wedge type failure, but has an extended logarithmic spiral which continues all the way up to the pile shaft, see Figure 19-1 on the right.

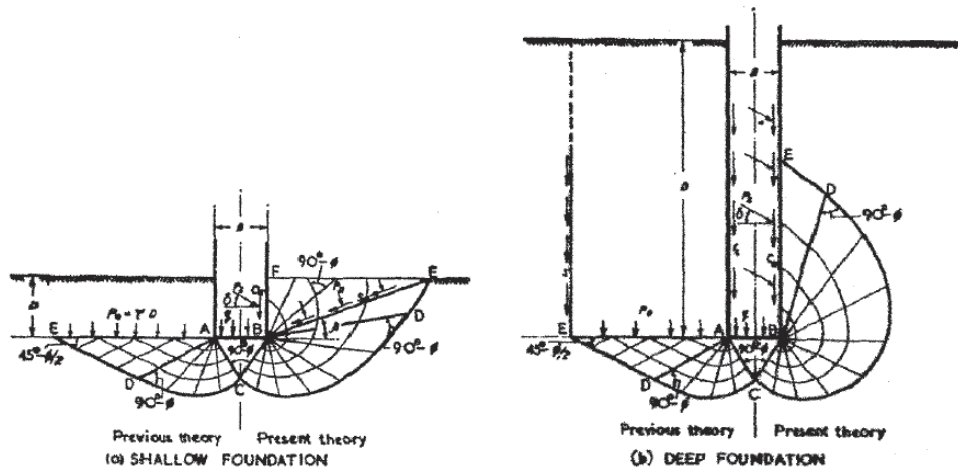


Figure 19-1. Logarithmic spiral shape failure mechanism around a pile tip I.

This extended logarithmic spiral shape failure mechanism around the pile tip has been adopted by other researchers, for example Van Mierlo & Koppejan (1952) and Caquot and Kerisel (1966).

In engineering practice a simpler, more practical and more reliable method has been developed, on the basis of a Cone Penetration Test (CPT), considering this as a model test (Boonstra, 1940).

According to field tests on real piles (White and Bolton, 2005), the bearing capacity (the average stress below the pile tip) depends on the installation method of the pile. Therefore, the bearing capacity (q_c -value) measured with the cone of the CPT (continuously installation) must be reduced before using it as bearing capacity for a driven (incremental installation) real pile tip.

Another point is that the thin CPT cone, as a model test, is unfortunately far more sensitive for the discontinuities of the subsoil than real piles. Therefore every CPT-based method needs a rule for “smoothening” the discontinuities over a certain distance. The distance over which this “smoothening” rule must be applied is, in case of the Koppejan’s method (Van Mierlo & Koppejan, 1952), based on this logarithmic spiral shape failure mechanism, see Figure 19-2. Because of this logarithmic spiral, the failure zone is, in the Koppejan’s method, assumed to reach from $0,7D$ to $4D$ below the pile tip, until $8D$ above the pile tip.

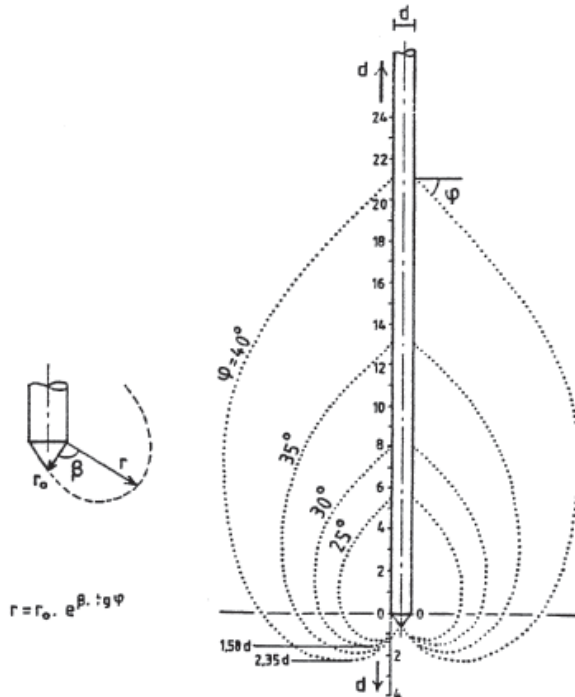


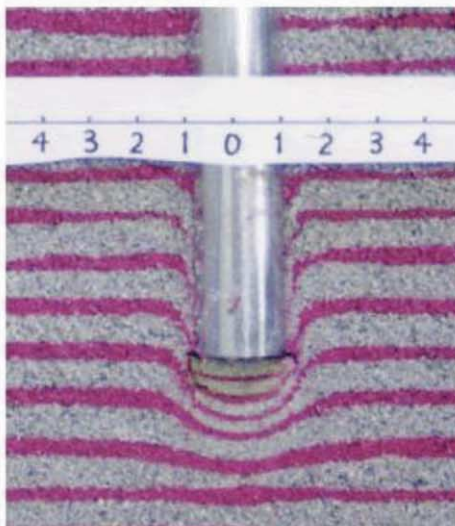
Figure 19-2. Logarithmic spiral shape failure mechanism around a pile tip II.

This failure mechanism is however incorrect. Although the soil below the level of the pile tip, can rotate away from the pile (similarly as Zone 2 of the Prandtl-wedge), shear failure or sliding along this logarithmic spiral above the level of the pile tip is however impossible, since this soil cannot rotate towards the pile and will not finally disappear in the pile.

Laboratory model tests show another failure mechanism for the pile foundations: a global, balloon shaped, failure zone, see Figure 19-3.

In order to check this failure mechanism for the pile foundations, also numerical axisymmetric simulations with Plaxis 2D have been made. Again a Mohr-Coulomb soil model has been used and a fine and wide mesh with 15-node elements. The soil has a Young's modulus of $E = 50$ MPa and a Poisson's ratio of $\nu = 0.3$. The groundwater level is at the surface. The pile has a radius of 0.20 m and is 10 m long. The pile has a high Young's modulus of $E = 30$ GPa, a Poisson's ratio of $\nu = 0.10$, and a roughness coefficient of $R = 0.70$. The pile loading has been modelled by a large vertical displacement of 20% of the pile diameter.

Plaxis 2D does not distinguish between out-of-plane, and in-plane plots for relative stresses. Therefore the same User Defined Soil Model, compiled as a Dynamic Link Library, has been used as in Chapter 13.2. for the shape factors in which the relative normal stress ratios and relative shear stress ratios were defined as State Parameters, independently for the out-of-plane and in-plane situations. These can easily be plotted by Plaxis.



Pile tip in Quiou sand

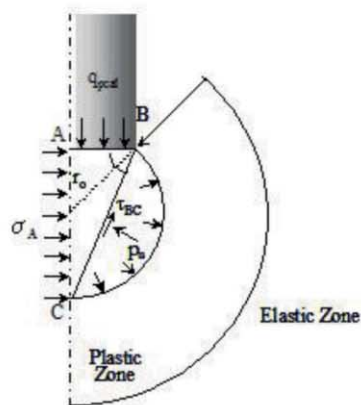


Figure 19-3. Global failure below pile tip in crushable sand.
(Picture from Kyushu University, Geotechnical Engineering Research Group)

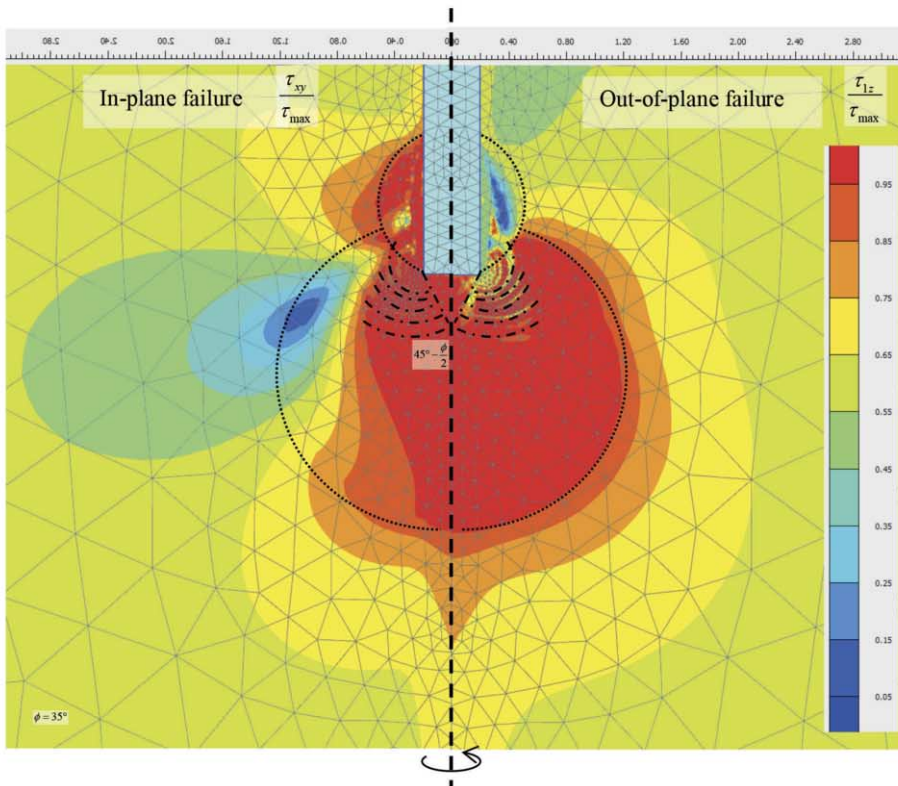


Figure 19-4. Numerical calculation of the failure zone around a pile tip.

Figure 19-4 shows, for a circular pile foundation, the relative shear stresses for both the x - y plane (in-plane), and also out of this plane (out-of-plane). This figure shows that there is failure both in and out of the standard x - y plane, but most of the failure is due to out-of-plane failure (the failure zone is much bigger). The only zone where this is the opposite, is the small zone just above and around the pile tip; here there is mostly in-plane failure. The zone with (in- or out-of-plane) failure is round as a ball, just as in Figure 19-3.

The numerical results show that the failure zone is mostly below, and not above, the level of the pile tip; from 5 to 6 D below the pile tip, until 2 or 3 D above the pile tip for a fully elasto-plastic soil, see Figure 19-4. Failure mostly occurs due to out-of-plane failure, just as for circular plates, see Chapter 13.2.

This shows that it is not correct to assume a Prandtl-wedge type of failure mechanism near the tip of a foundation pile, or to derive the smoothing zone from the shape of a logarithmic spiral (Van Baars 2017b, 2018c).

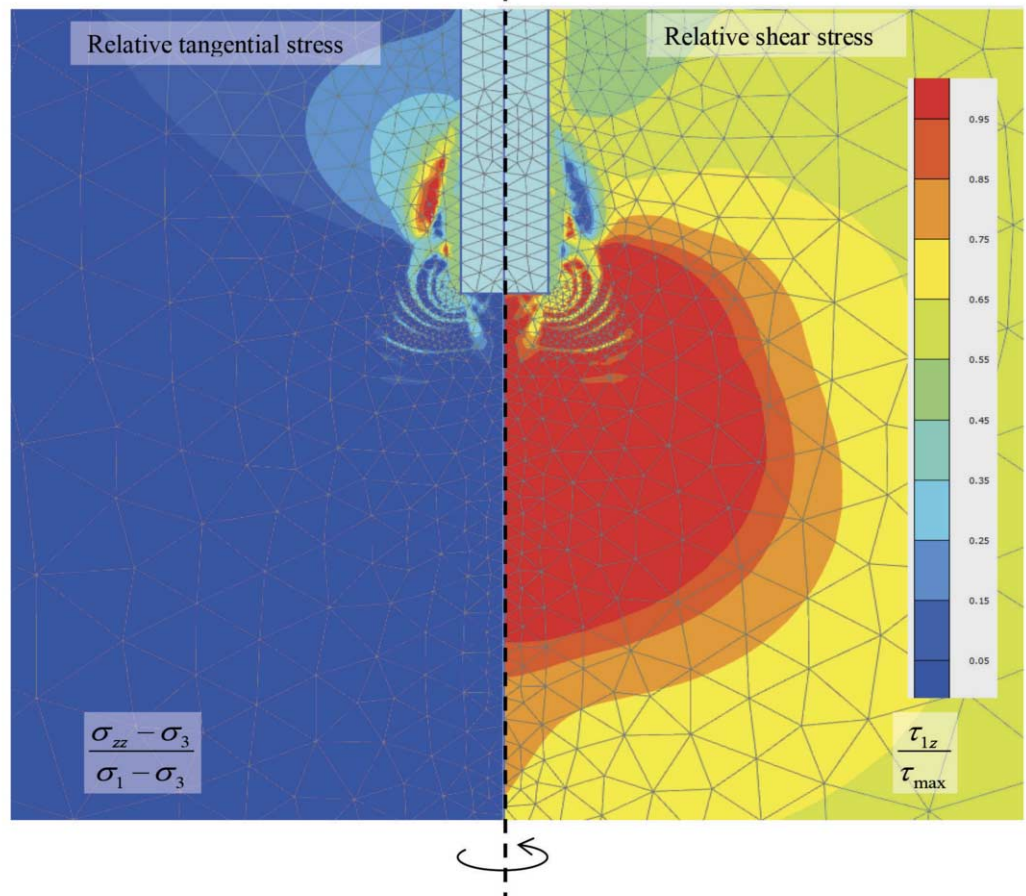


Figure 19-5. Tangential stress versus shear stress, around the pile tip.

Also interesting in Figure 19-4 are the circular thin zones around the pile tip, where there is no out-of-plane failure (but still in-plane failure!). The explanation for this follows from Figure 19-5. This figure shows the relative tangential stress ($\sigma_{zz} - \sigma_3$) / ($\sigma_1 - \sigma_3$) versus the relative out-of-plane shear stress, around the pile tip τ_{1z} / τ_{max} , in which τ_{max} is the maximum allowable radius of a Mohr circle touching the Coulomb envelope and τ_{1z} is the radius of the Mohr circle in the plain of the lowest principal stress (the tangential, circumferential or z-direction) and the highest principal stress (the 1-direction, which lays somewhere in the x-y plane). At the thin circular zones without out-of-plane failure, the tangential (out-of-plane) stresses are relatively high.

Figure 19-6 shows the reason for the relatively high tangential (out-of-plane) stresses. The zones of the relatively high tangential (out-of-plane) stresses or relatively low shear stresses (Figure 19-6 on the right), are exactly the zones of large (in plane) shear strains $\Delta\gamma_{xy}$ (Figure 19-6 on the left). These shear lines can also be found in the figures of the shallow foundations. These shear zones exist, because the inner circles rotate faster than the outside circles of the soil below the pile tip. So it seems that, this in-plane shearing or sliding allows the soil to shear partially in tangential direction (the lowest stress direction), which increases the stresses in tangential direction.

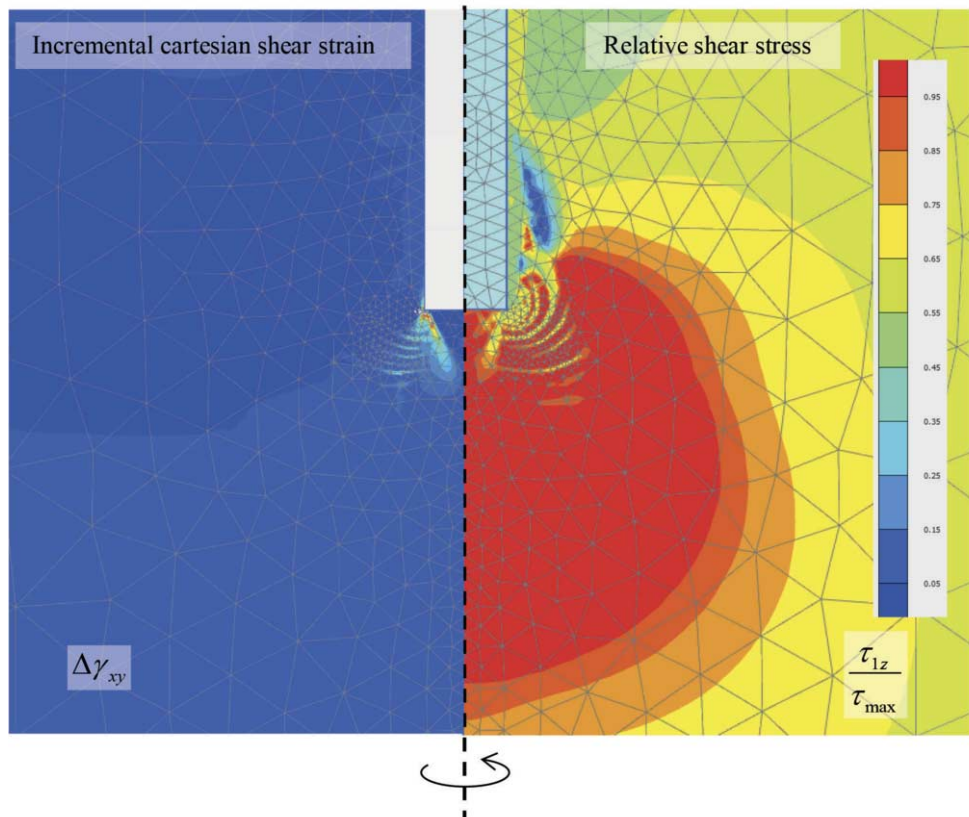


Figure 19-6. Incremental shear strain versus shear stress, around the pile tip.

20 Pile tip bearing capacity versus horizontal stress

According to Reissner, the bearing capacity of a shallow foundation depends on the vertical stresses. The assumption by Meyerhof, and others, that this also applies to pile foundations, is incorrect. In Cone Penetration Tests, the shaft friction τ and the cone resistance q_c show within a single soil layer always a similar pattern; in sand there is always a rather constant ratio or friction number of $\tau / q_c = f = 1\%$, see Figure 20-1 on the right.

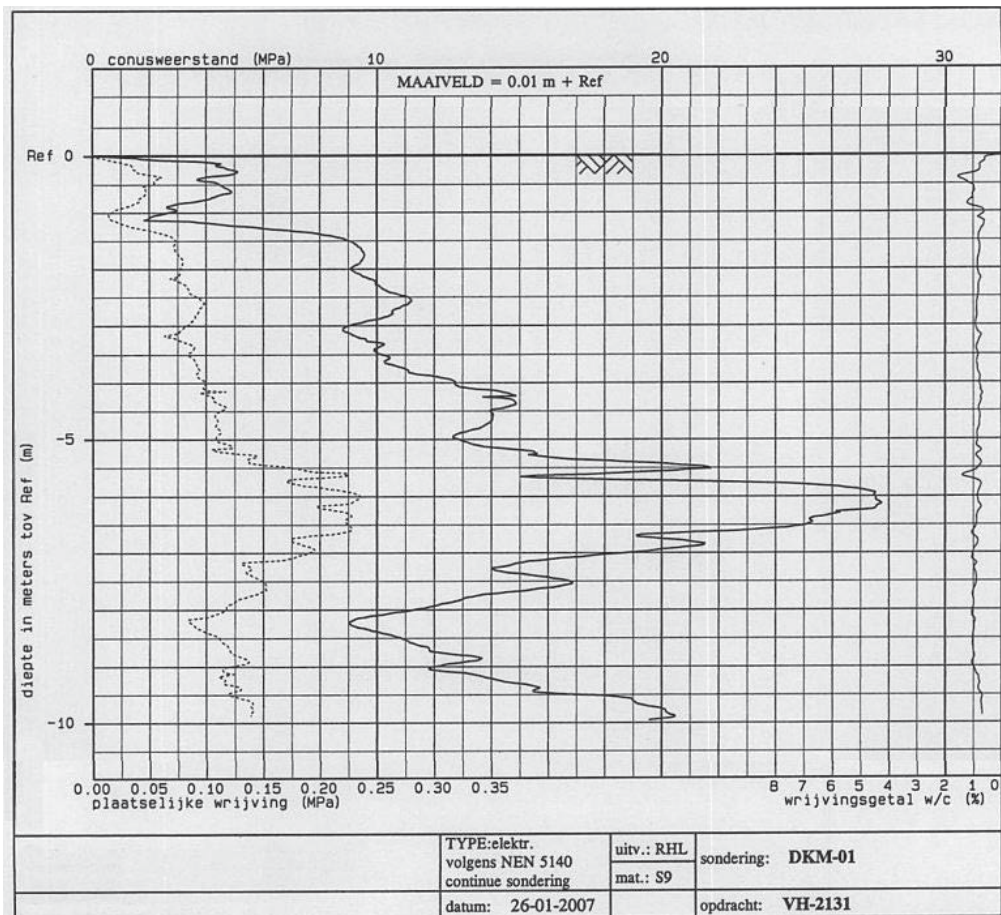


Figure 20-1. Cone penetration test in normally consolidated sand, showing shaft friction (left), cone resistance (middle) and friction number (right).

From this two conclusions can be drawn:

First, the cone resistance cannot depend on the vertical stress, since the cone resistance can decrease with depth (here between -6 and -8 m), while the vertical stress always increases with depth.

Second, since the shaft friction τ depends on the horizontal effective stress σ'_h (and the sand-shaft friction angle δ), more or less like:

$$\tau = \sigma'_h \cdot \tan \delta. \quad (20.1)$$

The ultimate load at failure p of a cone tip is by definition equal to the cone resistance q_c and does not depend on the vertical stress, but on the horizontal stress (after the installation), like:

$$p = q_c = \sigma'_h \cdot \frac{\tan \delta}{1\%}. \quad (20.2)$$

This suggests that the failure mechanism of a cone or pile tip is related to a sort of cavity expansion failure mechanism, controlled by the lowest (horizontal) stress, and is not, like shallow foundations, related to a Prandtl-wedge failure mechanism, controlled by the vertical stress or surcharge.

VI Appendices

21 Mohr-Coulomb and Rankine

The possible stresses in a soil are limited by the Mohr-Coulomb failure criterion. Following Rankine (1857) this condition will be used in this chapter to determine limiting values for the horizontal stresses, and for the lateral stress coefficient K .

The stress states in a soil can be limited, with a good approximation by the Mohr-Coulomb failure criterion. This criterion is that the shear stresses on any plane are limited by the condition:

$$\tau < \tau_f = c + \sigma \tan \phi, \quad (21.1)$$

where c is the cohesion, and ϕ is the angle of internal friction. The criterion can be illustrated using Mohr's circle, see Figure 21-1.

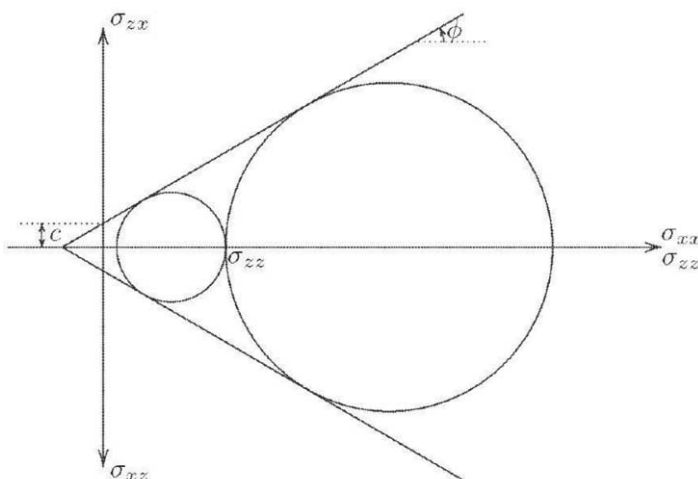


Figure 21-1. Mohr-Coulomb I.

If it is assumed that σ_{zz} and σ_{xx} are principal stresses, and that σ_{zz} is known (by the weight of the load and the soil), it follows that the value of the horizontal stress σ_{xx} cannot be smaller than indicated by the small circle, and not larger than defined by the large circle. The ratio between the minor and the major principal stress can be determined by noting, see Figure 21-2, that the radius of Mohr's circle is $\frac{1}{2}(\sigma_1 - \sigma_3)$, and that the location of the centre is at a distance $\frac{1}{2}(\sigma_1 + \sigma_3)$ from the origin. It follows that for a circle touching the envelope:

$$\sin \phi = \frac{\frac{1}{2}(\sigma_1 - \sigma_3)}{\frac{1}{2}(\sigma_1 + \sigma_3) + c \cdot \cot \phi},$$

which can also be written as:

$$\sigma_3 = \frac{1 - \sin \phi}{1 + \sin \phi} \sigma_1 - 2c \frac{\cos \phi}{1 + \sin \phi}. \quad (21.2)$$

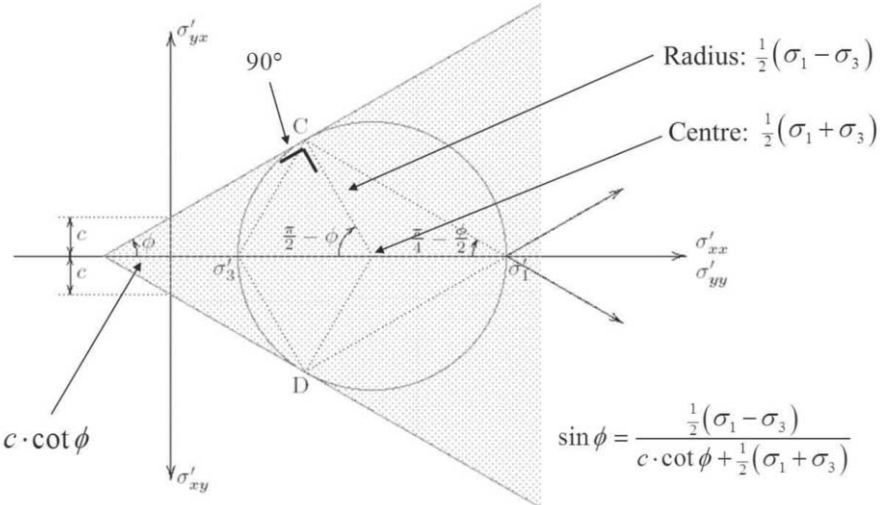


Figure 21-2. Mohr-Coulomb II.

The two coefficients in this equation can be related by noting that:

$$\frac{\cos \phi}{1 + \sin \phi} = \frac{\sqrt{1 - \sin^2 \phi}}{1 + \sin \phi} = \frac{\sqrt{(1 + \sin \phi)(1 - \sin \phi)}}{1 + \sin \phi} = \sqrt{\frac{1 - \sin \phi}{1 + \sin \phi}}.$$

This means that Equation (21.2) can be written as:

$$\sigma_3 = K_a \sigma_1 - 2c\sqrt{K_a} \quad \text{with: } K_a = \frac{1 - \sin \phi}{1 + \sin \phi}. \quad (21.3)$$

Apart from the constant term $2c\sqrt{K_a}$ there appears to be a given ratio of the minor and the major principal stress.

Equation (21.3) can be written in inverse form as:

$$\sigma_1 = K_p \sigma_3 + 2c\sqrt{K_p} \quad \text{with: } K_p = \frac{1 + \sin \phi}{1 - \sin \phi}. \quad (21.4)$$

The coefficients K_a and K_p , which give the smallest and the largest ratio of the two principal stresses (apart from a constant term), are denoted as the coefficients of active earth pressure K_a and passive earth pressure K_p , respectively.

The angle between the shear surface and the smallest principal stress is, according to Figure 21-2:

$$\theta_3 = \frac{1}{4}\pi + \frac{1}{2}\phi. \quad (21.5)$$

And the angle between the shear surface and the largest principal stress is:

$$\theta_1 = \frac{1}{4}\pi - \frac{1}{2}\phi. \quad (21.6)$$

22 N_c simplification

In order to simplify the N_c equation, the following parameters must be defined first (see Chapters 7 and 21):

$$N_q = K_p \cdot e^{\pi \tan \phi} \quad (7.9)$$

$$K_p = \frac{1 + \sin \phi}{1 - \sin \phi} = \frac{1}{\tan^2 \theta} \Rightarrow \sqrt{K_p} = \cot \theta \quad (21.4)$$

$$\theta = \frac{1}{4}\pi - \frac{1}{2}\phi \quad (217.6)$$

Also three equations (A , B and C) have to be derived from the following double angle equation, which can be found in any good Analysis book:

$$\tan 2\theta = \frac{2 \tan \theta}{1 - \tan^2 \theta}$$

This equation can be rewritten to Equation A :

$$\begin{aligned} \frac{1}{\tan \phi} &= \tan\left(\frac{1}{2}\pi - \phi\right) = \tan 2\theta = \frac{2 \tan \theta}{1 - \tan^2 \theta} \\ 1 - \tan^2 \theta &= \tan \phi \cdot 2 \tan \theta \\ 1 &= \tan^2 \theta + \tan \phi \cdot 2 \tan \theta \quad (A) \\ \frac{1}{\tan^2 \theta} &= 1 + \frac{2}{\tan \theta} \cdot \tan \phi \\ K_p &= 1 + 2\sqrt{K_p} \cdot \tan \phi \end{aligned}$$

This Equation A will be used later, but first it will be changed into Equation B :

$$\begin{aligned} 2K_p &= 1 + K_p + 2\sqrt{K_p} \cdot \tan \phi \\ 2K_p - 2\sqrt{K_p} \cdot \tan \phi &= 1 + K_p \\ 2\sqrt{K_p} (\sqrt{K_p} - \tan \phi) &= 1 + K_p \quad (B) \\ 2\sqrt{K_p} &= \frac{1 + K_p}{\sqrt{K_p} - \tan \phi} \\ 2\sqrt{K_p} \cdot \tan \phi &= \frac{\tan \phi + K_p \cdot \tan \phi}{\sqrt{K_p} - \tan \phi} \end{aligned}$$

This Equation B will be substituted in Equation A to find Equation C :

$$\begin{aligned} K_p &= 1 + \frac{\tan \phi + K_p \cdot \tan \phi}{\sqrt{K_p} - \tan \phi} \\ \frac{K_p}{\tan \phi} &= \frac{1 + K_p}{\sqrt{K_p} - \tan \phi} + \frac{1}{\tan \phi} \quad (C) \end{aligned}$$

This equation C will be needed later on.

The simplification starts from the equation of N_c (Chapter 8):

$$\begin{aligned}
 N_c &= \cot \theta + \left\{ e^{\pi \tan \phi} \cdot \left(\frac{\tan \theta}{1 - \tan \theta \cdot \tan \phi} \right) + \cot \phi (e^{\pi \tan \phi} - 1) \right\} \cdot \{1 + \cot \theta \cdot \tan \phi\} \\
 &= \sqrt{K_p} + \left\{ e^{\pi \tan \phi} \cdot \left(\frac{1}{\sqrt{K_p} - \tan \phi} \right) + \cot \phi (e^{\pi \tan \phi} - 1) \right\} \cdot \{1 + \sqrt{K_p} \cdot \tan \phi\} \\
 &= \sqrt{K_p} + e^{\pi \tan \phi} \cdot \left(\frac{1 + \sqrt{K_p} \cdot \tan \phi}{\sqrt{K_p} - \tan \phi} + \frac{1 + \sqrt{K_p} \cdot \tan \phi}{\tan \phi} \right) - \frac{1 + \sqrt{K_p} \cdot \tan \phi}{\tan \phi} \\
 &= e^{\pi \tan \phi} \cdot \left(\frac{1 + \sqrt{K_p} \cdot \tan \phi}{\sqrt{K_p} - \tan \phi} + \frac{1 + \sqrt{K_p} \cdot \tan \phi}{\tan \phi} \right) - \frac{1}{\tan \phi} \\
 &= e^{\pi \tan \phi} \cdot \left(\frac{1 + \sqrt{K_p} \cdot \tan \phi}{\sqrt{K_p} - \tan \phi} + \sqrt{K_p} + \frac{1}{\tan \phi} \right) - \frac{1}{\tan \phi} \\
 &= e^{\pi \tan \phi} \cdot \left(\frac{1 + K_p}{\sqrt{K_p} - \tan \phi} + \frac{1}{\tan \phi} \right) - \frac{1}{\tan \phi} \quad \{ \text{here equation } C \text{ is implemented} \} \\
 &= e^{\pi \tan \phi} \cdot \left(\frac{K_p}{\tan \phi} \right) - \frac{1}{\tan \phi} \\
 &= e^{\pi \tan \phi} \cdot K_p \cdot \cot \phi - \cot \phi \\
 &= (K_p \cdot e^{\pi \tan \phi} - 1) \cdot \cot \phi
 \end{aligned}$$

In this way the equation for N_c can be rewritten to:

$$\begin{aligned}
 N_q &= K_p \cdot e^{\pi \tan \phi} \\
 N_c &= (N_q - 1) \cot \phi \quad \text{with:} \quad K_p = \frac{1 + \sin \phi}{1 - \sin \phi} = \frac{1}{\tan^2 \theta} \quad (22.1)
 \end{aligned}$$

23 Prandtl's publication of 1920

Prandtl, L. (1920) Über die Härte plastischer Körper. *Nachrichten der Gesellschaft der Wissenschaften zu Göttingen, Mathematisch-physikalischen Klasse*, 74–85.

With thanks to the owner of this document, the Niedersächsische Staats- und Universitätsbibliothek Göttingen (SUB), Georg-August-Universität Göttingen, Germany.

Nachrichten

von der Königlichen Gesellschaft der Wissenschaften zu Göttingen

Mathematisch-physikalische Klasse
aus dem Jahre 1920

B E R L I N
Weidmannsche Buchhandlung
1920



Über die Härte plastischer Körper.

Von

L. Prandtl.

Vorgelegt in der Sitzung vom 18. Februar 1920.

1. Man verdankt Heinrich Hertz eine Theorie der Berührung elastischer Körper. Hertz selbst leitet aus seiner Theorie ein Maß für die Härte ab, indem er dafür diejenige Druckspannung in der Mitte der Druckfläche vorschlägt, durch die die Elastizitätsgrenze überschritten wird. Wegen der Unmöglichkeit einer sicheren Feststellung dieser Grenzbelastung bei nicht spröden Körpern hat man sich jedoch bei den praktischen Härtemessungen der Technik darauf geeinigt, bleibende Vertiefungen in das zu untersuchende Material einzudrücken und die mittlere Druckspannung in der Druckfläche als Härtemaß zu nehmen. Bei der Brinell-Probe wird z. B. eine gebärtete Stahlkugel in das Material eingedrückt. Eine Theorie des Spannungszustandes bei dieser bleibenden Formänderung ist bisher nicht bekannt geworden. Im folgenden soll gezeigt werden, daß eine solche Theorie für das entsprechende ebene Problem unter gewissen vereinfachenden Voraussetzungen möglich ist.

Der Begriff des plastischen Körpers soll hier weiter gefaßt werden, als dies nach dem Vorgang von B. de St. Venant und M. Lévy¹⁾ sonst meist üblich ist. Nach den Ansätzen dieser Beiden soll in denjenigen Gebieten des Körpers, in denen die Elastizitätsgrenze überschritten ist, die größte Schubspannung einen konstanten Wert C haben, oder, was dasselbe bedeutet, der Unterschied zwischen der größten und kleinsten Hauptspannung soll

1) B. de St. Venant, Journal de Math. 16 (1871) S. 308 und 373. M. Lévy, ebenda S. 369, vgl. auch Encycl. IV 81 (v. Kármán) Nr. 16.

konstant = $2C$ sein. Haar und v. Kármán¹⁾ unterscheiden hierbei noch den „halbplastischen“ und den „vollplastischen“ Zustand, je nach dem die dritte Hauptspannung irgend einen Wert zwischen den beiden andern Hauptspannungen hat, oder mit einer von diesen beiden übereinstimmt.

Hier soll eine etwas allgemeinere Bedingung für den plastischen Zustand formuliert werden: Dieser Zustand sei dadurch charakterisiert, daß zwischen der kleinsten und der größten Hauptspannung eine bestimmte Beziehung erfüllt ist, die wir im folgenden der Einfachheit halber als linear annehmen werden, die aber auch allgemeinerer Art sein kann. In dieser zuerst von O. Mohr²⁾ in etwas anderer äußerer Form aufgestellten Hypothese ist der „spezielle plastische Körper“ von de Saint-Venant, wie man sieht, als Sonderfall mit enthalten. Sie umfaßt aber auch solche häufig vorkommenden Fälle, in denen die Grenz-Schubspannung durch allseitigen Druck erhöht wird. Der Grenzfall, daß ohne einen allseitigen Druck diese Grenzschubspannung gleich Null ist, führt mit linearem Ansatz auf die übliche Erddrucktheorie.

Wir nehmen also an, daß überall dort, wo der Unterschied der kleinsten und der größten Hauptspannung kleiner ist, als der aus der erwähnten Beziehung folgende Wert, elastisches Verhalten vorhanden ist, und daß andererseits überall, wo die Elastizitätsgrenze überschritten ist, unabhängig von der Größe der Formänderung unsere Beziehung zwischen den äußeren Hauptspannungen erfüllt wird. Dabei müssen die Hauptachsen des Ellipsoids der Dehnungsgeschwindigkeiten mit denen des Spannungsellipsoids der Richtung nach übereinstimmen und die Vorzeichen der Differenzen der einzelnen Hauptdehnungen die gleichen sein wie die der Differenzen der entsprechenden Spannungen.

Wegen der Voraussetzung des ebenen Problems sind die Dehnungen nach der zur Ebene senkrechten Richtung gleich Null, woraus sich unmittelbar ergibt, daß hier der „halbplastische“ Zustand vorhanden ist mit der mittleren Hauptspannung senkrecht zur Ebene des Problems.

Da die elastischen Formänderungen für gedrangene Stücke aus den üblichen technischen Baustoffen sehr klein sind und die plastischen Formänderungen sie in vielen Fällen weit überwiegen, kann man sich die Aufgabe für die erste Näherung noch dadurch

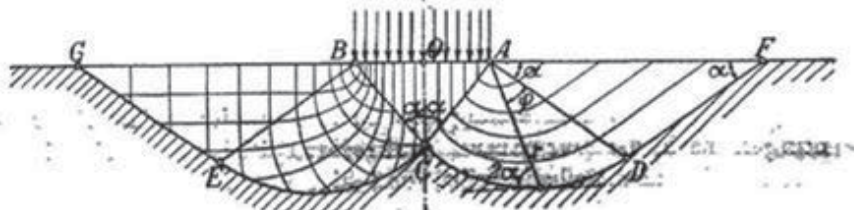
1) Göttinger Nachr. 1909 S. 204.

2) Otto Mohr, Ziviling. 1882, S. 113; Zeitschr. d. Ver. deutsch. Ing. 1900. S. 1524; Ges. Abhandl., Berlin 1906, S. 204 u. f., siehe auch Encycl. IV 31 (v. Kármán) Nr. 10.

vereinfachen, daß man die elastischen Formänderungswege überhaupt vernachlässigt. Gleichzeitig wird man dann auch das plastische Gebiet als unzusammendrückbar behandeln. Die Bewegungen im plastischen Gebiet werden dabei auch noch als klein angesehen. Man hat daher die Aufgabe zu lösen, eine solche Abgrenzung des plastischen Gebiets gegen den übrigen Körper zu finden, daß diese Grenze starr bleibt, während zugleich an den übrigen Grenzen die jeweils vorgegebenen Bedingungen erfüllt werden. Durch die Annahme der starren Begrenzung wird die Aufgabe dabei sehr wesentlich erleichtert.

Nach der Betrachtung von O. Mohr findet in einem Körper, der unserer Bedingung genügt, ein Gleiten des Materials längs zweier Scharen von Flächen statt, die um einen durch den Zustand bestimmten Winkel α gegen die Richtung der größten Druckspannung (kleinster Zugspannung) geneigt sind, und die die Richtung der mittleren Hauptspannung in sich enthalten. Im Falle der linearen Beziehung ist der Winkel α eine Materialkonstante. Eine einfache Überlegung lehrt, daß unsere starre Grenze eine Gleitfläche sein muß.

2. Es sei nun ein Gleitvorgang gesucht, bei dem durch Druck von außen ein Gebiet AB der ebenen freien Oberfläche (Fig. 1) nach innen gedrückt wird. Die Nachbargebiete links und rechts davon werden dann entsprechend aus der Oberfläche hervorquellen. Die nähere Untersuchung zeigt, daß diese Lösung durch die in Fig. 1 dargestellte Gebietsteilung gefunden ist: In dem Dreieck



Figur 1.

AB = belastetes Gebiet, $FDCEG$ Grenze des plastischen Gebiets gegen das elastische; in der linken Hälfte des plastischen Gebiets sind die Spannungsprojektionen, in der rechten Hälfte die „Stromlinien“ der plastischen Verschiebung angegeben.

ABC herrscht gleichförmiger Spannungszustand, senkrecht der gegebene große Druck, wagerecht ein etwas geringerer Gegendruck. Gleichförmiger Spannungszustand herrscht auch in den Dreiecken ADF und BEG . Hier ist der senkrechte Druck gleich

Null, der wagerechte, wie leicht ersichtlich, gleich der gewöhnlichen Druckfestigkeit. Zwischen den ersten und den beiden letzten Dreiecken liegen die sektorartigen Stücke ACD und BCE . Wenn der Nachweis gelingt, daß ein Zustand, in dem auf jeden von A bzw. B ausstrahlenden Radius ein homogener Spannungszustand herrscht, zu einem mit der Bedingung des plastischen Zustandes verträglichen Gleichgewicht führt, dann lassen sich die „Sektoren“ ACD und BCE mit stetigem Übergang der Spannungen an die Dreiecke anschließen und dadurch die Bedingungen der Aufgabe vollständig erfüllen. Die nachfolgenden Rechnungen werden diesen Nachweis erbringen. Zugleich ergibt sich, daß in den beiden Sektoren die Radien Gleitlinien sind, woraus unmittelbar folgt, daß — im Fall der linearen Beziehung — die Kurven CD und CE , die das andere System von Gleitlinien darstellen, das das erste unter dem Winkel 2α schneidet, logarithmische Spiralen sind. Die Spannung in der Druckfläche wird sich in Übereinstimmung mit der Erfahrung als wesentlich größer als die Druckfestigkeit ergeben.

3. Die Durchführung der Rechnung gestaltet sich folgendermaßen:

Die Beziehung zwischen der größten Hauptspannung σ_1 und der kleinsten Hauptspannung (größten Druckspannung) σ_2 , mag im Fall der Linearität in der Form geschrieben werden

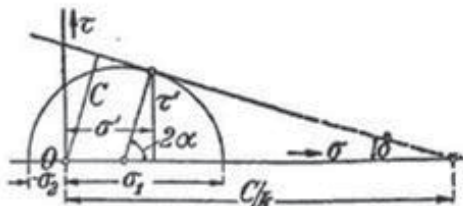
$$\frac{\sigma_1 - \sigma_2}{2} = C - k \frac{\sigma_1 + \sigma_2}{2}. \quad (1)$$

Hierbei stellt die linke Seite die größte Schubspannung dar, die zum Spannungszustand σ_1 , σ_2 gehört; diese zeigt sich hier also als lineare Funktion des Mittelwerts von σ_1 und σ_2 .

Trägt man nach dem Vorschlag von O. Mohr die auf den in den verschiedensten Orientierungen gezogenen Schnittflächen wirkenden Schubspannungen τ als Ordinaten zu den zugehörigen Normalspannungen σ als Abszissen auf, so sind alle Spannungszustände durch Punkte eines Gebietes dargestellt, daß nach außen durch einen Kreis vom Durchmesser $\sigma_1 - \sigma_2$ mit dem Mittelpunkt auf der σ -Achse begrenzt ist. Die Gleichung (1) liefert als Enveloppe der Spannungskreise eine Gerade, die den Abstand C vom Nullpunkt hat und die Achse bei $\sigma = C/k$ trifft, vgl. Fig. 2. Im allgemeinen Fall einer nichtlinearen Beziehung anstelle von Gl. (1) ist die Enveloppe eine Kurve.

Die Schnittflächen, deren Spannungszustände durch Punkte des Grenzkreises dargestellt werden, enthalten sämtlich die Richtung

der mittleren Hauptspannung in sich. Der Berührpunkt zwischen Kreis und Enveloppe ist dabei den Gleitflächen zugeordnet (O. Mohr a. a. O.). Das Lot aus dem Punkte $\frac{\sigma_1 + \sigma_2}{2}$ auf die Enveloppe liefert hiermit den doppelten Gleitflächenwinkel α , da allgemein die Radien



Figur 2.

des Spannungskreises den doppelten Winkel mit der σ -Achse einschließen, wie die entsprechenden Schnittflächen mit der σ_z -Achse. Gemäß Fig. 2 ist im linearen Fall

$$k = \sin \delta = \cos 2\alpha. \quad (2)$$

Die Spannungskomponenten auf der Gleitfläche werden nach Fig. 2:

$$\sigma' = \frac{\sigma_1 + \sigma_2}{2} + \frac{\sigma_1 - \sigma_2}{2} \sin \delta, \quad (3a)$$

$$\tau' = \frac{\sigma_1 - \sigma_2}{2} \cos \delta. \quad (3b)$$

Sind nicht die Hauptspannungen σ_1 und σ_2 unmittelbar gegeben, sondern ein allgemeiner ebener Spannungszustand, so hat man die Gleichungen

$$\frac{\sigma_1 + \sigma_2}{2} = \frac{\sigma_x + \sigma_y}{2}; \quad \frac{\sigma_1 - \sigma_2}{2} = \sqrt{\left(\frac{\sigma_x - \sigma_y}{2}\right)^2 + \tau^2} \quad (4)$$

Aus Gl. (1) wird somit jetzt die Gleichung

$$\sqrt{\left(\frac{\sigma_x - \sigma_y}{2}\right)^2 + \tau^2} + k \cdot \frac{\sigma_x + \sigma_y}{2} = C \quad (5)$$

als Bedingung für den plastischen Zustand erhalten.

Führt man durch die Beziehungen

$$\sigma_x = \frac{\partial^2 F}{\partial y^2}, \quad \sigma_y = \frac{\partial^2 F}{\partial x^2}, \quad \tau = -\frac{\partial^2 F}{\partial x \partial y}$$

eine Spannungsfunktion F („Airysche Funktion“) ein, so entsteht aus Gl. (5) eine Differentialgleichung 2. Ordnung, die, da immer $k < 1$ ist, vom hyperbolischen Typus ist. Durch diesen Umstand ist die Möglichkeit, die Lösung aus einzelnen Flicken zusammen-

zusetzen, mathematisch begründet. Die Charakteristiken der Differentialgleichung sind unsere Gleitlinien; die einzelnen Flicken sind daher immer von Gleitlinien begrenzt.

4. Für die sektorartigen Gebiete ACD und BCE ist nun ein der Gl. (5) genügender Spannungszustand zu finden, der auf den Grenzradien konstante aber verschiedene Spannung ergibt. Es liegt nahe, diese Eigenschaft von allen Radien zu verlangen. Führt man zur Feststellung des inneren Gleichgewichtes eine Spannungsfunktion F ein, so muß diese in Polarkoordinaten somit die Gestalt

$$F = \frac{r^2}{2} f(\varphi) \quad (6)$$

haben. Die Spannungen σ_r (radial), σ_θ (tangential) und τ werden hiermit

$$\left. \begin{aligned} \sigma_r &= \frac{1}{r^2} \frac{\partial^2 F}{\partial \varphi^2} + \frac{1}{r} \frac{\partial F}{\partial r} = \frac{1}{4} f'' + f, \\ \sigma_\theta &= \frac{\partial^2 F}{\partial r^2} = f; \quad \tau = -\frac{\partial}{\partial r} \left(\frac{1}{r} \frac{\partial F}{\partial \varphi} \right) = -\frac{1}{2} f'. \end{aligned} \right\} \quad (7)$$

Gl. (5) liefert also für f die Differentialgleichung:

$$\frac{1}{2} \sqrt{\frac{1}{4} f''^2 + f'^2} + k(\frac{1}{4} f'' + f) = C. \quad (8)$$

Eine Lösung von Gl. (8) ist

$$f = C/k + A e^{\beta \varphi}, \quad (9)$$

wobei β der Gleichung

$$\frac{\beta^2}{4} \left(\frac{\beta^2}{4} + 1 \right) + k^2 \left(\frac{\beta^2}{4} + 1 \right)^2 = 0 \quad (10)$$

genügen muß. Ein Wertepaar dieser Gleichung vierten Grades ist $\beta = \pm 2i$; die zugehörige Lösung $f(\varphi) = C_1 \cos 2\varphi + C_2 \sin 2\varphi$ stellt einen gewöhnlichen homogenen Spannungszustand dar und nicht den hier gesuchten. Nach Division von Gl. 10 durch $\frac{\beta^2}{4} + 1$ ergibt sich das zweite Wertepaar zu

$$\beta = \pm \frac{2k}{\sqrt{1-k^2}} = \pm 2 \operatorname{tg} \delta. \quad (11)$$

Für den Sonderfall $k = 0$ (spezieller plastischer Körper) wird $\beta = 0$, wodurch Gl. (9) die unbestimmte Form $\infty - \infty$ annimmt. Ein sehr einfacher Grenzübergang ergibt hier die Lösung

$$f = \pm 2C\varphi + \text{const.} \quad (9a)$$

Bildet man nun — für den allgemeinen Fall — mittels der Gleichungen (7) die Ausdrücke für σ_r , σ_t und τ , so lassen sich daraus mittels der Beziehungen (4) die Hauptspannungen ermitteln. Es wird für das +Zeichen in Gl. (11)

$$\sigma_1 = \frac{C}{k} + \frac{A \cdot e^{2\varphi \operatorname{tg} \delta}}{1 \pm k}, \quad (12)$$

wobei zu beachten ist, daß A immer negativ ist. Für den speziellen plastischen Körper wird

$$\sigma_1 = C(2\varphi \pm 1) + \text{const.}$$

Durch die Übereinstimmung der Werte von σ_t und τ mit den aus (12) und (8a) bzw. 8b) berechneten Werten von σ' und τ' ergibt sich, daß die radialen Flächen des Sektors in der Tat Gleitflächen sind. Hiermit ergibt sich sofort aus den in den Dreiecksgebieten herrschenden Spannungszuständen (Hauptspannungen senkrecht und parallel zur Oberfläche), daß die Winkel FAD und ACO , und die zu ihnen symmetrischen, Gleitwinkel, also $= \alpha$ sind. Damit folgt somit auch, daß $\angle CAD$ und $\angle CBE$ rechte Winkel sind.

Setzt man nun an, daß in dem Dreieck ADF , und damit also auch auf den Radius AD des Sektors ADC $\sigma_1 = 0$ und hiermit gemäß Gl. (1) $\sigma_r = -\frac{2C}{1-k}$ (= gew. Druckfestigkeit) ist, so wird nach leichter Rechnung für den um $\frac{\pi}{2}$ gegen AD verdrehten Radius AC :

$$\sigma_1 = -\frac{C}{k}(e^{\pi \operatorname{tg} \delta} - 1) \quad (13a)$$

und

$$\sigma_2 = -\frac{C}{k} \left(\frac{1+k}{1-k} e^{\pi \operatorname{tg} \delta} - 1 \right). \quad (13b)$$

Diese Spannungen herrschen aber gleichmäßig in dem ganzen Dreieck ABC . Der Ausdruck (13b) gibt also die Druckspannung der Oberfläche zwischen A und B an, ist daher das gesuchte Härtemaß.

Führt man in (13b) die gewöhnliche Druckfestigkeit $= \sigma_d = \frac{2C}{1-k}$ ein, so ergibt sich für die „plastische Härte“ die Formel:

$$\sigma_h = \frac{\sigma_d}{2k} \left((1+k) e^{\frac{\pi k}{1-k}} - (1-k) \right). \quad (14)$$

Für den speziellen plastischen Körper erhält man durch dieselben Überlegungen im Anschluß an Gl. (9a) oder auch durch Grenzübergang aus Gl. (14):

$$\sigma_h = \sigma_d \left(1 + \frac{\pi}{2}\right). \quad (14a)$$

Ist k von Null verschieden, wie es z. B. bei Gemengen von harten Körnern mit einem plastischen Bindemittel vorkommt, bei denen neben den plastischen Bewegungen des Bindemittels auch die Reibung der harten Körner an einander eine Rolle spielt, so steigt das Verhältnis $\sigma_h : \sigma_d$ mit wachsendem k stark an (vgl. die Tabelle am Schluß der Arbeit).

Anmerkungen:

1) Die vorstehenden Überlegungen lassen sich unmittelbar auch auf die Festigkeit einer abgestumpften Schneide vom Keilwinkel ϑ anwenden (anstelle von Fig. 1 ist eine Figur zu setzen, bei der der Linienzug $FABG$ an den Stellen A und B geknickt ist, und bei dem die Linien FA und BG den Winkel ϑ mit einander bilden). Die Schneidenfestigkeit wird, wie unschwer zu erkennen ist, gewonnen, wenn in Gl. (14) ϑ an die Stelle von π gesetzt wird.

2) Wirkt der Stempeldruck nicht senkrecht zur Oberfläche bzw. bei der abgestumpften Schneide von Anm. 1) nicht in der Winkelhalbierenden, sondern irgendwie schräg, so wird das Dreieck ABC (Fig. 1) ebenfalls schräg, und zwar so, daß die Winkelhalbierende des Winkels ACB in der Kraftrichtung verbleibt. Dadurch würden die beiden Sektoren verschiedene Winkel aufweisen, also auch verschiedene Spannungen σ_1 und σ_2 für die Linien AC und BC ergeben. Das ist wegen des Gleichgewichts in ABC nicht möglich, vielmehr ergibt sich, daß nur in dem Sektor mit dem kleineren Winkel und dem anschließenden Dreieck der plastische Zustand eintritt, auf der andern Seite von ABC dagegen die Elastizitätsgrenze nicht überschritten wird. Die Formänderung vollzieht sich hier ganz einseitig.

3) Wenn die Bedingung des plastischen Zustandes nicht die Form von Gl. (1) hat, sondern die Enveloppe der Figur 2 gekrümmmt ist, so gelten die Entwicklungen des vorstehenden Absatzes immer noch für Sektoren von infinitesimalem Winkel, denn auf jedem Radius ist ja der Spannungszustand und daher auch die Größe k konstant. Man erhält z. B. durch Differenzieren von (12):

$$\frac{d\sigma_1}{d\vartheta} = 2(\sigma_1 - C/k) \operatorname{tg} \vartheta = 2 \cdot \frac{k\sigma_1 - C}{\sqrt{1-k^2}}.$$

Nun läßt sich aber jederzeit für ein bestimmtes Plastizitätsgesetz k als Funktion von σ_1 darstellen, so daß sich der Winkel des Sektors, der jetzt $= \frac{\pi}{2} + \alpha_h - \alpha_d$ ist (α_h Gleitwinkel für die Härte-

spannung, α_d Gleitwinkel für die Druckfestigkeit) durch eine Quadratur ergibt. Anstelle von (14) tritt also jetzt die Beziehung

$$\int_{\sigma_d}^{\sigma_1} \frac{\sqrt{1-k^2}}{k\sigma_i - C} \cdot d\sigma_i = \pi + 2(\alpha_k - \alpha_d). \quad (14b)$$

5. Es bleiben noch die Bewegungen des plastischen Körpers unter der Wirkung des Stempels zu klären. Nimmt man den Stempel als starr an, und seine Oberfläche als genügend rauh, um Gleitung zu verhindern, dann werden beim Tieferdringen des Stempels die einmal mit ihm in Berührung gelangten Oberflächenteile des plastischen Körpers sich parallel und gleichförmig nach unten weiter bewegen, was zur Folge hat, daß das Gebiet ABC in Fig. 1 sich wie ein starrer Körper bewegt. Eine infinitesimale Bewegung dieser Art erzeugt, wie eine nähere Betrachtung lehrt, in den Sektoren Verschiebungen in der Richtung der Tangente an die logarithmischen Spiralen, wobei die Verschiebungen auf jedem einzelnen Radius konstant und, wegen der Volumbeständigkeit, der Länge des Radius umgekehrt proportional ist. Die Außendreiecke werden dadurch wie starre Körper längs der Linien DF und EG hinaus geschoben. Die zur Oberfläche lotrechte Komponente dv dieser Verschiebung verhält sich wegen der Kontinuität zu der Stempelverschiebung ds umgekehrt wie \overline{AF} zu \overline{OA} .

Da $\overline{OA} : \overline{AC} = \sin \alpha$, $\overline{AD} : \overline{AF} = 1/2 \cos \alpha$ und $\overline{AC} : \overline{AD} = e^{-\frac{\pi}{2} \operatorname{tg} \delta}$
ist (logarithmische Spirale mit dem Neigungswinkel $\frac{\pi}{2} - 2\alpha = \delta$, vgl. Fig. 2), so wird

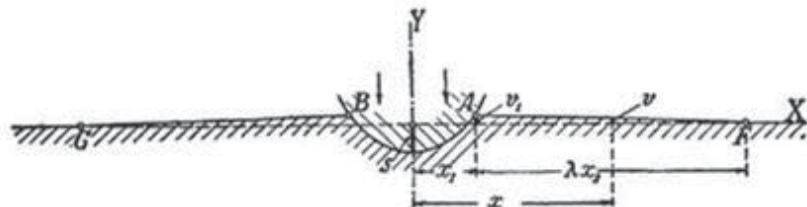
$$\frac{\partial v}{\partial s} = \frac{1}{2} \operatorname{tg} \alpha e^{-\frac{\pi}{2} \operatorname{tg} \delta} = \frac{1}{2} \sqrt{\frac{1-k}{1+k}} e^{-\frac{\pi}{2} \cdot \frac{k}{\sqrt{1-k^2}}} \quad (15)$$

(wegen $\cos 2\alpha = \sin \delta = k$, Gl. (2)).

Für endliche Bewegungen ist wohl zu beachten, daß während des Weiterdringens des Stempels die Breite AB des gepreßten Streifens fortwährend zunimmt und somit die Feldergrenzen der Figur 1 sich dauernd verschieben. Dabei stellt sich dem Eindringen das vorher herausgequollene Material entgegen, so daß die Breite AB für einen bestimmten Weg s größer ausfällt, als sich aus der elementaren geometrischen Betrachtung ergeben würde. Die Gestalt der durch einen Stempelweg s bei einem Abrundungsradius r des Stempels eintretenden Verlagerung der Oberfläche läßt sich wie folgt berechnen.

Da alle Formänderungswege als klein gegen den Radius r angesehen werden, und also auch nur kleine Neigungen gegen die ursprüngliche Oberfläche vorkommen, können die Wirkungen der tangentiaalen Verschiebungen u auf die Oberflächengestalt gegen die der Verschiebungen v (senkrecht zur Oberfläche) vernachlässigt werden. Es wird daher hier nur v berechnet. Die Gleichung der Stempeloberfläche sei $y = x^3/2r$, woraus sich (vgl. Fig. 3) für die Verschiebung der Oberfläche des plastischen Körpers innerhalb der Strecke \overline{AB} mit $s = \text{Stempelweg}$ ergibt

$$(16) \quad v = x^3/2r - s.$$



Figur 3 (Zeichnung stark überhöht!)

Wird mit x_i die derzeitige Länge der Strecke \overline{OA} bezeichnet, so ist $\overline{AF} = \lambda x$ mit

$$(17) \quad \lambda = \frac{1}{\frac{\partial v}{\partial s}} = 2 \sqrt{\frac{1+k}{1-k}} e^{\frac{\pi}{2} \cdot \frac{k}{\sqrt{1-k^2}}}.$$

Dann ist für $x > (\lambda + 1)x_i$: $v = 0$.

Für $x_i < x < (\lambda + 1)x_i$ ist daher unter Berücksichtigung von Gl. (15)

$$(18) \quad v = \frac{\partial v}{\partial s} (s - s') = (s - s')/\lambda$$

zu setzen, wobei s' die Stempelverschiebung ist, bei der die Hebung der Stelle x gerade begann, bei der somit die Druckfläche den Halbmesser $x' = \frac{x}{\lambda + 1}$ hatte.

Aus Gl. (16) folgt für die zu $x = x_i$ gehörige Verschiebung v_i (vgl. Fig. 8)

$$(19) \quad s + v_i = x_i^3/2r.$$

Wir vermuten, daß das Zahlenverhältnis von s und v_i unveränderlich ist und setzen

$$(20) \quad s = \mu x_i^3/2r,$$

ebenso

$$(21) \quad s' = \mu x^3/2r(\lambda + 1)^3.$$

Die Gleichungen (19) und (20) und die auf $x = x_1$ angewandten Gleichungen (18) und (21) reichen nur gerade aus, um nach Fortschaffung von s , s' und $x_1^*/2r$ eine Beziehung zwischen μ und λ allein herzustellen, womit unsere Annahme, die zu Gl. (20) führte, bewiesen ist. Es wird

$$(22) \quad \mu = \frac{\lambda(\lambda+1)^2}{(\lambda+1)^2 - 1}$$

und hiermit unter Benützung von (18) und (21):

$$(23) \quad v = \frac{s}{\lambda} - \frac{x^*}{2r} \cdot \frac{1}{(\lambda+1)^2 - 1}$$

für $x_1 < x < (\lambda+1)x_1$, wobei gemäß (20) $x_1 = \sqrt{2rs/\mu}$ ist.

Die Verschiebung der freien Oberfläche liefert hier in erster Annäherung also ein affines Abbild der Stempelform mit im Verhältnis $(\lambda+1):1$ vergrößerter Abszisse und im Verhältnis $1:\lambda$ verkleinerter Ordinate. Diese Beziehung scheint für symmetrische Stempelprofile mit flacher und mit Ausnahme der Stelle $x = 0$ nirgends das Vorzeichen wechselnder Neigung allgemein zu gelten.

Die höchste Erhebung am Rand des Eindruckes wird in unserem Beispiel wegen Gl. (19) und (20)

$$(24) \quad v_1 = (1-\mu) \frac{x_1^*}{2r} = s \cdot \frac{1-\mu}{\mu} = s \cdot \frac{\lambda+2}{(\lambda+1)^2}.$$

Anmerkung:

Erfolgt die Stempelbewegung nicht senkrecht, sondern schräg, so wird die Erhebung zu beiden Seiten des Stempels ungleich hoch, während die Kraft in erster Ordnung ungeändert ihre senkrechte Richtung beibehält; erst wenn die Schrägen der Verschiebung den Gleitwinkel α überschreitet und die Erhebung auf der einen Seite völlig ausbleibt, ergeben sich schräge Kraftrichtungen, vgl. Anm. 2 zu Nr. 4.

Tabelle.

δ	α	k	σ_k/σ_d	λ	μ	v_1/s
0°	45°	0	2,571	2,000	0,6923	0,4445
10°	40°	0,1786	3,499	3,144	0,7695	0,2995
20°	35°	0,3420	5,194	5,059	0,8887	0,1923
30°	30°	0,5000	8,701	8,579	0,8966	0,1153
40°	25°	0,6428	17,558	16,924	0,9413	0,0624

Zusammenfassung.

Für Stoffe, die bei Überschreitung der Elastizitätsgrenze ein plastisches Verhalten aufweisen, das durch eine lineare Beziehung zwischen der größten und kleinsten Hauptspannung gekennzeichnet wird, wird der Spannungszustand beim Eindringen eines harten Körpers im ebenen Problem angegeben, ebenso der zugehörige Formänderungszustand. Einige Erweiterungen werden in Anmerkungen zugefügt.

24 Reissner's publication of 1924

Reissner, H. (1924) Zum Erddruckproblem, *Proceedings of the 1st International Congress for Applied Mechanics*, Biezeno, C. B. and Burgers, J. M. eds., Delft, the Netherlands, 295–311.

Zum Erddruckproblem

von H. REISSNER, Charlottenburg-Berlin.

Die erste Grundaufgabe der Erddrucktheorie besteht in der Ermittlung der Spannungszustände des Grenzgleichgewichts im kohäsionslosen, schweren Erdkörper. Diese Grundaufgabe ist bisher nur in zwei Fällen gelöst worden, nämlich von RANKINE für den Spannungszustand des seitlich unbegrenzten, parallel zur Oberfläche gleichmässigen Erdkörpers und von KÖTTER für den unendlich langen und den kreisförmigen Spalt. Der im allgemeinen wesentliche Einfluss des Eigengewichts erschwert die Auffindung der Spannungszustände ganz außerordentlich, dagegen ist die Ermittlung von Spannungszuständen infolge von Oberflächenkräften allein einfacher und von BOUSSINESQ für verschiedene Oberflächenbedingungen durchgeführt worden. Auch die PRANDTL'schen, HENCKY'schen und E. SCHMIDT'schen Lösungen für den allgemein und speziell plastischen, gewichtslosen Körper gehören in die Kategorie dieser letzteren Aufgabenstellung.

In den folgenden Betrachtungen soll die oben gestellte Aufgabe für das *ebene* Problem auf mehrere Arten vollständig formuliert und die bisherigen nebst einigen neuen Lösungen im Zusammenhang diskutiert werden.

Der *Grenzzustand des Reibungsgleichgewichts* an einem Punkte eines Erdkörpers wird erreicht, wenn in einem Flächenelement die resultierende Spannung ρ grade den Reibungswinkel φ mit der Flächennormalen, in allen andern Flächenelementen aber einen kleineren Winkel einschliesst. Mit Hilfe der Hauptspannungen $\sigma_I > \sigma_{II} > 0$ drückt sich diese Bedingung so aus:

$$\sigma_I = \sigma_{II} \frac{1 + \sin \varphi}{1 - \sin \varphi} \quad \dots \dots \dots \dots \dots \quad (1)$$

oder mit Hilfe der gewöhnlichen Spannungskomponenten σ_x, σ_y, τ :

$$\left(\frac{\sigma_I - \sigma_{II}}{\sigma_I + \sigma_{II}} \right)^2 = \frac{(\sigma_x - \sigma_y)^2 + 4\tau^2}{(\sigma_x + \sigma_y)^2} = \sin^2 \varphi \quad \dots \dots \dots \quad (1a)$$

wo alle Spannungen Druckspannungen sein müssen, und die dritte Hauptspannung σ_{III} ihrer Grösse nach zwischen den beiden massgebenden Hauptspannungen liegen soll.

An zwei Flächenelementen, den sogenannten *Gleitflächenelementen*, wird grade der Reibungswinkel φ zwischen resultierender Spannung ρ und Flächennormale eingeschlossen und sie bilden mit den Flächenelementen der Hauptspannungsrichtungen die Winkel $\frac{\pi}{4} - \frac{\varphi}{2}$ bzw.

$\frac{\pi}{4} + \frac{\varphi}{2}$, sodass die Hauptspannungsrichtungen die Winkel zwischen den Gleitflächen halbieren (Abb. 1).

Die resultierende Spannung ρ an den Gleitflächen hat den Wert:

$$\rho = \sigma_I \operatorname{tg} \left(\frac{\pi}{4} - \frac{\varphi}{2} \right) = \sigma_I \frac{\cos \varphi}{1 + \sin \varphi}. \quad \dots \dots \dots \quad (2)$$

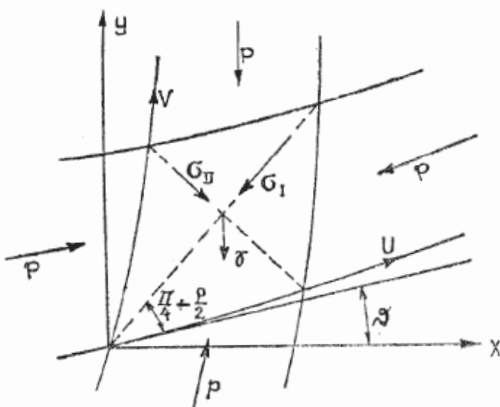


Abb. 1.

Der Winkel α der Hauptspannungstrajektorien mit der X - bzw. Y -Achse, ist gegeben durch:

$$\operatorname{tg} 2\alpha = \frac{2\tau}{\sigma_x - \sigma_y} \quad \dots \dots \dots \dots \dots \dots \quad (3)$$

und der Winkel ϑ der einen Schaar von Gleitlinien mit der X -Achse nach Abb. 1 durch:

$$\operatorname{tg} 2\vartheta = \frac{\operatorname{tg} 2\alpha - \cot \rho}{1 + \operatorname{tg} 2\alpha \cos \rho} \quad \dots \dots \dots \dots \dots \dots \quad (3a)$$

I. Die Airy'sche Funktion als Ausgangspunkt.

Allgemeines.

Es möge zunächst der Grenzzustand bezogen auf kartesische Koordinaten mit Hilfe der AIRY'schen Spannungsfunktion untersucht werden. Die Gleichgewichtsbedingungen (vergl. Abb. 2):

$$\frac{\partial \sigma_x}{\partial x} + \frac{\partial \tau}{\partial y} = 0, \quad \frac{\partial \tau}{\partial x} + \frac{\partial \sigma_y}{\partial y} = -\gamma. \quad (4)$$

(γ = spezifisches Gewicht des Erdkörpers), werden von einer Spannungsfunktion z befriedigt, wenn man — mit den in der Theorie der partiellen Differentialgleichungen üblichen Bezeichnungen ρ , r , s , t , für die Ableitungen erster und zweiter Ordnung von z — ansetzt:

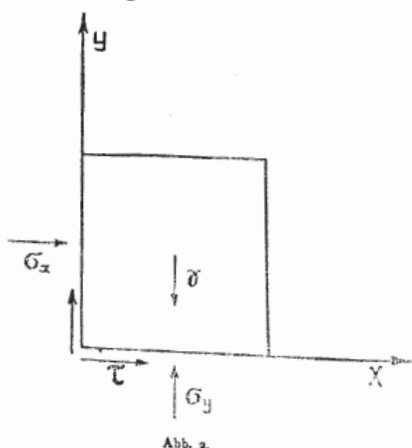


Abb. 2.

$$\sigma_x = t, \quad \sigma_y = r - \gamma y, \quad \tau = -s.$$

Die Funktion z selbst genügt nach Gleichung (1a) die partielle Differentialgleichung:

$$F \equiv (r - \gamma y - t)^2 - (r - \gamma y + t)^2 \sin^2 \rho + 4s^2 = 0 \quad \dots \dots \dots \quad (5)$$

Die Theorie der partiellen Differentialgleichungen zweiter Ordnung legt es nahe nach den sogenannten *Charakteristiken zweiter Art* und ihrer Beziehung zu den Gleitlinien zu

bedeuten. Diese Oberflächenspannungen pflanzen sich längs der beiden Scharen von Gleitlinien, d. h. unter den Winkeln $\pm \left(\frac{\pi}{4} - \frac{\rho}{2} \right)$ zur Y-Achse nach vorwärts und rückwärts unverändert und sich überlagernd fort.

Die fingierte Belastung der ideellen Fortsetzung der Geländeoberfläche.

Die Oberfläche sollte nun allerdings unbelastet sein, sodass also für ein seitlich unbegrenztes Gelände der RANKINE'sche Spannungszustand keine Nachbarlösungen zulässt. Ist jedoch eine z. B. senkrechte Wand angenommen, so gilt diese Grenzbedingung nur für den wirklich vorhandenen Teil des Erdreichs, während hinter der Wand eine Fortsetzung des Erdreichs fingiert werden kann, und die Oberfläche dieses fingierten Bereiches beliebig belastet gedacht werden darf, und zwar so, dass sogar die im Erdreich sonst unzulässigen Zugspannungen auftreten dürfen, wenn nur in dem als wirklich vorausgesetzten Bereich keine Zugspannungen vorkommen. Ferner müssen sich längs der Gleitlinie, welche sich von der Mauerkrone aus in das Innere des wirklichen Erdkörpers erstreckt, die Spannungen stetig an diejenigen des ungestörten Erdkörpers anschliessen, d. h. die Belastungsfläche muss an der Mauerkrone mit der Oberflächenbelastung Null beginnen.

Nachbarzustände können also nur in dem Bereich zwischen der von der Wandoberkante ausgehenden, fallenden Gleitlinie (Linie 3 in Abb. 3) und der Wand auftreten; wie wir später sehen werden, krimmen sich dort die Gleitlinien derart, dass sie mit stetiger Tangente und Krümmung in die graden Gleitlinien ausserhalb des Störungsbereichs übergehen.

Beschränkt man sich auf genügend nahe zum ursprünglichen Zustand benachbarte Spannungszustände, dann besteht die durch die Lösung der Gleichung (8) gegebene Variation des Spannungszustandes in einer Ueberlagerung einer beliebigen Zusatzspannung $\tau'_{,x}$, $\sigma'_{,y} = \frac{1}{a^2} \tau'_{,x}$ und $\tau' = \frac{1}{a} \sigma'_{,x}$, welche nur die Bedingungen zu erfüllen hat, dass sie sich erstens längs jeder der Gleitlinien, welche von der fingierten Oberfläche durch die Wand in das Innere des wirklichen Erdkörpers laufen, ungeändert fortpflanzt und zweitens auf der höchsten von der Mauerkrone ausgehenden Gleitlinie Null wird.

Man erkennt nun leicht, dass wenn die Wand als vollkommen glatt betrachtet wird, die Schubspannung τ' Null bleiben muss, und dass deshalb auch die mit ihr zwangsläufig verknüpften Normalspannungen $\sigma'_{,x}$ und $\sigma'_{,y}$ Null bleiben, sodass man den Satz aussprechen darf:

Für seitlich unbegrenztes wagerechtes Gelände und für wagerechtes Gelände und senkrechte glatte Wand gibt es in der Nachbarschaft des RANKINE'schen Spannungszustandes der ebenen Gleitflächen keinen anderen widerspruchsfreien Spannungszustand.

Schreibt man dagegen der Wand Rauhigkeit zu, dann ergibt die obige Lösung unendlich viele benachbarte, widerspruchsfreie, im Grenzgleichgewicht befindliche Spannungszustände. Zu Widersprüchen gelangt man bei Vernachlässigung der quadratischen Glieder nur, wenn man gemäss einem wichtigen Untersuchungsziel der Erddrucktheorie nach dem kleinsten für rauhe Wand möglichen Erddruck fragt, weil dieses Minimum Zusatzspannungen verlangt, die in dem oben angegebenen Sinne nicht mehr klein sind.

Diese Frage nach dem Minimum verlangt also die Berücksichtigung der in r , t und s quadratischen Glieder.

Man kann diese Glieder als Störungsfunktion ansehen und kann — nach dem RIEMANN'schen Integrationsverfahren für die durch äussere Kräfte belastete Saite — die Gleichung (5a) in eine Integralgleichung verwandeln.

Die Gesamtdruckspannung normal zur Wand ergibt sich also im Falle des Wanddruckminimums der ersten Näherung zu:

$$\sigma_x = \sigma_{x0} + \sigma_{x1} = \sigma_{x0} \frac{1 + \sin \rho}{1 + 2 \sin \rho}.$$

Für den gesamten Wanddruck bis zur Tiefe h findet man:

$$E = E_0 \frac{1 + \sin \rho}{1 + 2 \sin \rho} = 0,750 E_0 \text{ für } \rho = 30^\circ,$$

wo: $E_0 = \gamma \frac{h^2}{2} \frac{\cos \rho}{(1 + \sin \rho)^2}$ den RANKINE'schen Erddruck bedeutet.

Man beachte, dass hierbei gekrümmte Gleitflächen innerhalb des früher definierten Störungsprismas entstehen und dass die COULOMB'sche Theorie, welche bei rauher Wand falschlich grade Gleitflächen beibehält, bekanntlich den Wert: *)

$$E_{Coulomb} = \gamma \frac{h^2}{2} \frac{\cos^2 \rho}{(1 + \sqrt{2} \sin \rho)^2} = E_0 \left(\frac{1 + \sin \rho}{1 + \sqrt{2} \sin \rho} \right)^2,$$

und für $\rho = 30^\circ$, $E_{Coulomb} = 0,778 \cdot E_0$ liefert.

Allerdings darf nicht übersehen werden, dass die Bedingung des Grenzgleichgewichts an allen Punkten mit Ausnahme der Oberfläche nur bis auf lineare Glieder erfüllt ist.

Um den Fehler der Vernachlässigung der quadratischen Glieder zu verkleinern, werde nun die zweite Näherung wie folgt eingeführt:

In den durch Gleichung (5d) gegebenen Wert von χ werde der aus der oben berechneten Zusatzspannung σ_{x1} entnommene Wert von r_{y1}^0 eingesetzt. Es wird:

$$r_{y1}^0 = \sigma_{x1} \frac{2}{a^2} = -2 \gamma y_1 \frac{\sin \rho}{1 + 2 \sin \rho} = +2 \gamma \frac{x}{a} \frac{\sin \rho}{1 + 2 \sin \rho}.$$

Das in der zweiten Näherungslösung auftretende Flächenintegral $\frac{a}{2} \iint_{A_0 B_0 C_0} \chi \, df$ (Abb. 3) kann jetzt berechnet werden und ergibt sich zu:

$$\frac{a}{2} \iint_{A_0 B_0 C_0} \chi \, df = \frac{a}{2} \iint_{FD A_0 C_0} \chi \, df = \frac{5}{24} \gamma \frac{\sin \rho \cos^2 \rho}{(1 + \sin \rho)^2 (1 + 2 \sin \rho)^2} y_1^3.$$

Die zusätzliche Normalspannung an der Wand σ_{x2} wird:

$$\sigma_{x2} = -\frac{5}{4} \gamma \frac{\sin \rho \cos^2 \rho}{(1 + \sin \rho)^2 (1 + 2 \sin \rho)^2} y_1,$$

wobei es sehr bemerkenswert ist, dass sich das Gesetz der linearen Zunahme nach der Tiefe nicht ändert, sodass die gesamte Normalspannung bis zur zweiten Näherung den Wert erhält:

$$\sigma_x = \sigma_{x0} + \sigma_{x1} + \sigma_{x2} = \gamma y_1 a^2 \left(1 - \frac{\sin \rho}{1 + 2 \sin \rho} + \frac{5}{4} \frac{\sin \rho}{(1 + 2 \sin \rho)^2} \right).$$

Wählt man wiederum als Zahlenbeispiel $\rho = 30^\circ$ so wird:

$$\sigma_x = \gamma y_1 a^2 \left(1 - \frac{1}{4} + \frac{5}{32} \right) = 0,907 \gamma y_1 a^2.$$

*) Siehe z. B. MÜLLER-BRESLAU, Erddruck auf Stützmauern, 1906, S. 14.

In demselben Verhältnis steht dann auch der gesamte Erddruck:

$$E = 0,907 \cdot E_0.$$

Während die erste Näherung bei vollkommen rauher Wand einen etwas kleineren Wert ergibt als die COULOMB'sche in sich bekanntlich nicht widerspruchsfreie Theorie, nämlich $0,750 E_0$ gegen $E_{Coulomb} = 0,775 E_0$, liefert die zweite zuverlässigere Näherung erheblich mehr, nämlich $0,907 E_0$. Daher erklärt es sich wohl auch, wenn alle Experimentatoren das Auftreten des grösseren Wanddruckes unter Beibehaltung der COULOMB'schen Theorie durch eine unvollkommene Rauhigkeit der Wand erklärt haben.

In Wirklichkeit ist das Auftreten grösserer als der COULOMB'schen Drucke im unteren Grenzzustande nicht auf die mangelnde Rauhigkeit der Wand, sondern auf die in sich folgeunrichtige Beibehaltung ebener Gleitflächen beim nicht RANKINE'schen Spannungszustand zurückzuführen.

Die erste Näherungslösung ging von derjenigen fingierten Oberflächenbelastung aus, welche den kleinsten Wanddruck liefert.

Die zweite Näherung und auch die etwa folgenden zeigen, dass der kleinste Wanddruck erster Näherung in zweiter Näherung nicht auf den kleinsten Wanddruck zweiter Näherung führt.

Man müsste also die Frage formulieren, welche fingierte Oberflächenbelastung auf dem ideellen Gelände hinter der Wand bei der ersten Näherung anzusetzen ist, um in zweiter oder höherer Näherung einen unteren Grenzwert des Erddruckes zu erhalten. Die Lösung dieses COULOMB-KÖTTER'schen Variationsproblems erfordert offenbar eine besondere Untersuchung.

II. Die Gleitfläche als Ausgangspunkt.

In der oben gezeigten Weise müssten weiter gewonnen werden: die Spannungszustände der höheren Näherungen, die Zusatzspannungen für andere Wand- und Geländeanordnungen und die diesen Zusatzspannungen entsprechenden Gleitflächen im gestörten Gebiet zwischen Wand und fallender RANKINE'scher Fläche.

Eine solche Weiterführung der Integration auf dem bisher eingeschlagenen Wege erscheint zwar durchaus nicht aussichtslos, ist aber immerhin doch so mühevoll, dass man versuchen wird, auch auf anderen Wegen an das Ziel heranzukommen. Dazu leitet ausserdem noch der Umstand, dass die in dem Vorhergehenden befolgte und weiter geführte RANKINE'sche Methode die sich der kartesischen Koordinaten bedient, bisher weniger Aufschluss über die wichtigen Fragen des Erddrucks gegeben hat, als die COULOMB-KÖTTER'sche Methode, welche von den Gleitlinien als der Wurzel der Erscheinungen ausgeht. So wird man dazu geführt, statt der kartesischen Koordinaten die Gleitlinienschaaren selbst als krummlinige Koordinaten einzuführen, ein Kunstgriff, der aus der Theorie der partiellen Differentialgleichungen bekannt und neuerdings mit grossem Erfolge in den Untersuchungen von PRANDTL, HENCKY und E. SCHMIDT und CARATHÉODORY über den speziell plastischen Körper angewandt worden ist.

Die Massau-Kötterschen Gleichungen.

Die Einführung dieser Gleitlinien als Koordinatenlinien kann nun auf folgende Weise vor sich gehen: Bezeichnet man die Gleitlinien durch die Funktionen $u(x, y)$ und $v(x, y)$ derart, dass $u = \text{const.}$ und $v = \text{const.}$ je eine Gleitlinie darstellen, so kann das Längenelement irgend einer Kurve in der Ebene der u und v bekanntlich in der Form geschrieben werden:

$$ds^2 = U^2 du^2 + V^2 dv^2 + 2 F du dv.$$

Sollen sich, wie in der Einleitung nachgewiesen, die Linien $u = \text{const.}$ und $v = \text{const.}$ überall unter den Winkeln $\frac{\pi}{2} - \rho$ bzw. $\frac{\pi}{2} + \rho$ schneiden, so nimmt das Linienelement die besondere Form an:

$$ds^2 = U^2 du^2 + V^2 dv^2 + 2 UV \sin \rho du dv. \dots \dots \dots \quad (9)$$

Nach Abb. 1 werde nun noch der Winkel $\tilde{\alpha}$ der Gleitlinie $u = \text{const.}$ mit der X -Achse eingeführt und zwar positiv gerechnet, wenn die X -Achse durch den positiven Quadranten in die Richtung der wachsenden u gedreht wird.

Beachtet man nämlich, dass $U du$ und $V dv$ die Längenelemente in Richtung der wachsenden u und v sind, so kann man aus Abb. 1 ablesen:

$$\frac{\partial x}{\partial u} = U \cos \tilde{\alpha}, \quad \frac{\partial x}{\partial v} = -V \sin (\tilde{\alpha} - \rho), \quad \frac{\partial y}{\partial u} = U \sin \tilde{\alpha}, \quad \frac{\partial y}{\partial v} = +V \cos (\tilde{\alpha} - \rho). \quad (9a)$$

Eine einfache Umformung ergibt:

$$\frac{\partial \tilde{\alpha}}{\partial u} V \cos \rho = \frac{\partial V}{\partial u} \sin \rho - \frac{\partial U}{\partial v}, \quad \frac{\partial \tilde{\alpha}}{\partial v} U \cos \rho = -\frac{\partial U}{\partial v} \sin \rho + \frac{\partial V}{\partial u}. \dots \dots \quad (10)$$

Ebenfalls nach Abb. 1 können nun die Gleichgewichtsbedingungen in Richtung der wachsenden u und v abgelesen werden in der Form:

$$\left. \begin{aligned} \frac{\partial p}{\partial v} U + \frac{\partial p}{\partial u} V \sin \rho + p V \cos \rho \frac{\partial \tilde{\alpha}}{\partial u} &= -\gamma UV \cos \rho \cos (\rho - \tilde{\alpha}) \\ \frac{\partial p}{\partial u} V + \frac{\partial p}{\partial v} U \sin \rho - p U \cos \rho \frac{\partial \tilde{\alpha}}{\partial v} &= -\gamma UV \cos \rho \sin \tilde{\alpha} \end{aligned} \right\} \dots \dots \quad (11)$$

Führt man nun die geometrischen Gleichungen (10) in diese Gleichgewichtsbedingungen ein, so ergeben sich Beziehungen, die man wohl mit Recht als die MASSAU-KÖTTER'schen Gleichungen*) bezeichnen kann, nämlich:

$$\frac{1}{U} \left[\frac{\partial p}{\partial u} - 2p \operatorname{tg} \rho \frac{\partial \tilde{\alpha}}{\partial u} \right] = -\gamma \sin (\tilde{\alpha} - \rho), \quad \frac{1}{V} \left[\frac{\partial p}{\partial v} + 2p \operatorname{tg} \rho \frac{\partial \tilde{\alpha}}{\partial v} \right] = -\gamma \cos \tilde{\alpha}. \quad (12)$$

Gerade Gleitlinien und der Rankine'sche Spannungszustand.

Der RANKINE'sche Zustand der in Richtung der Oberfläche gleichförmigen Spannung wird erhalten, wenn man beide Scharen von Gleitlinien gradlinig annimmt, also setzt:

$$\frac{\partial \tilde{\alpha}}{\partial u} = \frac{\partial \tilde{\alpha}}{\partial v} = 0, \quad U = V = 1.$$

Die Gleichungen (12) geben dann:

$$p = p_0 - \gamma [u \sin (\tilde{\alpha} - \rho) + v \cos \tilde{\alpha}] \dots \dots \dots \dots \quad (13)$$

wo p_0 der Druck in der Tiefe $u = 0, v = 0$ bezeichnet.

Soll an der Oberfläche $p = p_a$ sein, so gilt dort:

$$u \sin (\tilde{\alpha} - \rho) + v \cos \tilde{\alpha} = \frac{p_0 - p_a}{\gamma}.$$

Diese Oberfläche schneidet die v -Achse für $u = 0$ und die u -Achse für $v = 0$ in den Punkten:

*) Vergl. F. KÖTTER, Berl. Akad. Ber. 1903, S. 229—233; MASSAU, loc. cit., p. 151.

$$v_a = - \frac{p_a - p_0}{\gamma \cos \vartheta}, \quad u_a = - \frac{p_a - p_0}{\gamma \sin(\vartheta - \rho)}.$$

Aus der Abb. 4 liest man für den Winkel φ zwischen Geländeoberfläche und der einen Gleitlinienschaar ab:

$$\frac{u_a}{\sin \varphi} = \frac{v_a}{\cos(\rho - \varphi)} \quad \text{oder: } \cot \varphi = \operatorname{tg} \vartheta - 2 \operatorname{tg} \rho,$$

und damit für den Winkel ψ zwischen der Vertikalen und der Geländeoberfläche:

$$\psi = \varphi + \vartheta - \rho.$$

v_a bzw. u_a kann man als Mass der Mauerhöhe ansehen und durch v_a bzw. u_a den Druck p_0 am Mauerruss ausdrücken, nämlich:

$$p_0 = p_a + \gamma v_a \cos \vartheta = p_a + \gamma u_a \sin(\vartheta - \rho).$$

Die Neigung der Geländeoberfläche ergibt sich, wie man sieht, unabhängig vom Oberflächendruck p_a und längs den Parallelen zur Oberfläche ist ρ konstant.

Im Uebrigem gestatten die abgeleiteten Formeln natürlich auch alle andere bekannten, bei dem RANKINE'schen Spannungszustand auftretenden Tatsachen zu verifizieren.

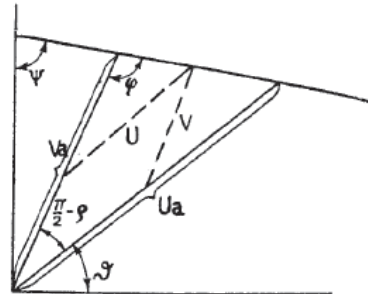


Abb. 4.

Der gewichtslose Sandkörper.

Für den Sandkörper mit vernachlässigbarem Eigengewicht, bei welchem also die Oberflächendrücke den überwiegenden Einfluss haben, ist es nicht schwierig Spannungszustände und Gleitlinien des Grenzgleichgewichts anzugeben, wie dies in besonderen Fällen schon BOUSSINESQ gezeigt hat. Auch die PRANDTL'schen Gleitlinien der Schneidenwirkung des allgemein plastischen Körpers sind von derselben Art.

Allgemein kann man über den gewichtslosen Sandkörper folgendes zeigen:

Die KÖTTER'schen Gleichungen (12) vereinfachen sich zu den Beziehungen:

$$\frac{\partial (\ln p - 2 \vartheta \operatorname{tg} \rho)}{\partial u} = 0, \quad \frac{\partial (\ln p + 2 \vartheta \operatorname{tg} \rho)}{\partial v} = 0,$$

oder:

$$\ln p - 2 \vartheta \operatorname{tg} \rho = \frac{\Phi}{2}, \quad \ln p + 2 \vartheta \operatorname{tg} \rho = \frac{\Omega}{2},$$

wenn Φ eine reine Funktion von v und Ω eine solche von u bedeuten.

Die Trennung der Unbekannten p und ϑ ergibt:

$$\ln p = \Omega + \Phi, \quad 2 \vartheta \operatorname{tg} \rho = \Omega - \Phi,$$

wonach:

$$p = e^{\Omega + \Phi} = \Omega_1 \Phi_1 \quad \text{und} \quad \frac{\partial^2 \vartheta}{\partial u \partial v} = 0.$$

Die letzte Gleichung stimmt überein mit der von HENCKY *) für das orthogonale Gleitliniensystem eines rein plastischen Körpers aufgestellten Gleichung.

*) Zeitschr. f. angew. Math. u. Mech. Bd. 3, 1923, S. 241—251.

Die geometrischen Beziehungen (10) liefern dann die Bestimmung der Koeffizienten U und V des Linienelements, nämlich:

$$\frac{1}{2} \Omega' V \cot \rho \cos \rho = \frac{\partial V}{\partial u} \sin \rho - \frac{\partial U}{\partial v}, \quad - \frac{1}{2} \Phi' U \cot \rho \cos \rho = \frac{\partial V}{\partial u} - \frac{\partial U}{\partial v} \sin \rho,$$

oder wenn man $\frac{1}{2} \Omega' \cot \rho \cos \rho = \Omega_2$, $-\frac{1}{2} \Phi' \cot \rho \cos \rho = \Phi_2$ setzt:

$$\frac{\partial V}{\partial u} \sin \rho - \frac{\partial U}{\partial v} = V \Omega_2, \quad \frac{\partial V}{\partial u} - \frac{\partial U}{\partial v} \sin \rho = U \Phi_2.$$

Gradliniges Gleitlinienbüschel des gewichtslosen Sandkörpers. Das Fundamentalsproblem.

Die Lösung dieses Gleichungssystems wird besonders einfach, wenn man die eine Gleitlinienschaar, etwa $v = \text{const.}$ gradlinig vorschreibt, also mit $\frac{\partial \vartheta}{\partial u} = 0$, $\Omega_2 = 0$ setzt, wodurch übrigens der Druck $p = c\Phi_1$, also eine reine Funktion von v wird, demnach auf den graden Gleitlinien $v = \text{const.}$ konstant ist.

Die Gleichungen (10) ergeben damit weiter:

$$U = \Omega'_3 e^{\Phi_2 v \frac{\sin \rho}{\cos^2 \rho}}, \quad V = \frac{\Omega_3}{\cos^2 \rho} \frac{d\Phi_2}{dv} e^{\Phi_2 v \frac{\sin \rho}{\cos^2 \rho}} + \Phi_3,$$

wo Ω_3 und Φ_3 wiederum willkürliche Funktionen von u bzw. v allein sind.

Man kommt zu einer besonders anschaulichen Lösung, wenn man als Koordinaten einführt den Winkel $\varphi = v$ der gradlinigen Gleitlinien mit der Horizontalen und die Abstände der Schnittpunkte der anderen Gleitlinienschaar von einem festen Punkte auf der horizontalen Gleitlinie $r_0 = u$. Damit ist:

$$\frac{\partial \vartheta}{\partial v} = 1, \quad \vartheta = \varphi, \quad \Phi_2 = \cos \rho \frac{\partial \vartheta}{\partial v} = \cos \rho, \quad \Omega'_3 = 1, \quad \Omega_3 = r_0,$$

$$U = e^{\varphi \tan \rho}, \quad V = \frac{r_0}{\cos \rho} e^{\varphi \tan \rho} + \Phi_3.$$

Sollen sich alle Gleitlinien der gradlinigen Schaar in einem Punkte schneiden, so ist $\Phi_3 = 0$ zu setzen und man gelangt zu dem BOUSSINESQ'schen Fall des gewichtslosen Sandkörpers zwischen starren Ebenen und zu dem Analogfall der PRANDTL'schen *) Gleitlinien des plastischen Körpers. Die zweite Schaar besteht dann offenbar aus logarithmischen Spiralen.

Die oben abgeleitete Gleichung für den Druck ergibt schliesslich:

$$p = \text{const. } e^{-2\varphi \tan \rho}.$$

Die Abb. 5 und 6 zeigen, welchen verschiedenen Anordnungen man durch den obigen Ansatz entsprechen kann. (Die Erweiterung des obigen Ansatzes durch Wahl einer Funktion Φ_3 in V würde schliesslich ein Büschel von graden Gleitlinien, die sich nicht in einem Punkte schneiden, sondern eine gewisse Kurve umhüllen, ergeben).

Die Gleitlinien dieser Fälle haben auffallende Uebereinstimmung mit den Gleitlinienphotographien, die KURDJUMOFF **) bei dem Hereindrücken von Stempeln in Sand

*) Zeitschr. f. angew. Math. u. Mech. Bd. 1, 1921, S. 15—28.
**) Zivilingenieur, 1892.

erhalten hat und die das Fundamentproblem beleuchten sollten. Die Anwendbarkeit auf das Fundamentproblem ist freilich beschränkt wegen der im allgemeinen nicht zulässigen Vernachlässigung des Eigengewichts.

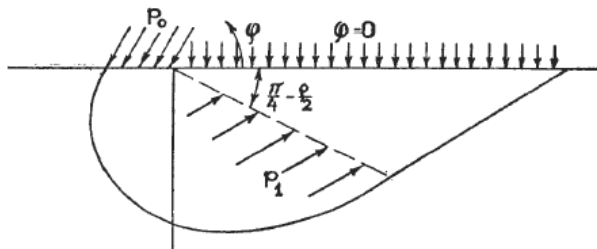


Abb. 5.

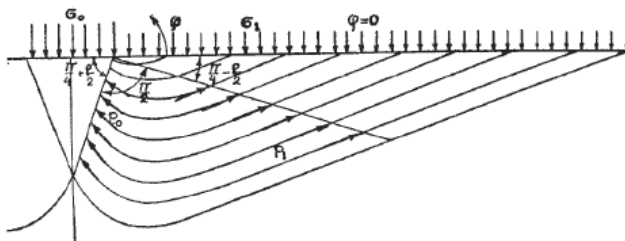


Abb. 6.

Die Abb. 5 und 6 zeigen die beiden auch von KURDJUMOFF experimentell gefundenen Möglichkeiten des unsymmetrischen und des symmetrischen Ausweichens des gewichtslosen Erdkörpers unter einem Stempel (Fundament). Dort wo auf die Oberfläche lotrechte Drücke wirken, müssen die büschelförmigspiraligen Gleitlinien durch einen sich stetig anschliessenden RANKINE'schen Spannungszustand mit zweifach gradlinigen Gleitlinien in einem halbrhomischen Gebiet abgelöst werden.

Die Rechnung nach den oben abgeleiteten Formeln ergibt für die beiden Fälle des unsymmetrischen und des symmetrischen Nachgebens folgendes:

Unsymmetrischer Fall:

$$\sigma_1 = p_1 \operatorname{tg} \left(\frac{\pi}{4} - \frac{\rho}{2} \right), \quad p_1 = c e^{\varphi \left(\frac{\pi}{4} - \frac{\rho}{2} \right) \operatorname{tg} \varphi}, \quad p_0 = c e^{2 \pi \operatorname{tg} \varphi}, \quad \sigma_0 = p_0 \sin \left(\frac{\pi}{2} - \rho \right),$$

also:

$$\sigma_0 = \sigma_1 (1 + \sin \rho) e^{\varphi \left(\frac{3}{4} \pi + \frac{\rho}{2} \right) \operatorname{tg} \varphi}.$$

Symmetrischer Fall:

$$\sigma_1 = p_1 \operatorname{tg} \left(\frac{\pi}{4} - \frac{\rho}{2} \right), \quad p_1 = c e^{\varphi \left(\frac{\pi}{4} - \frac{\rho}{2} \right) \operatorname{tg} \varphi}, \quad p_0 = c e^{\varphi \left(\frac{3}{4} \pi + \frac{\rho}{2} \right) \operatorname{tg} \varphi}, \quad \sigma_0 = p_0 \operatorname{tg} \left(\frac{\pi}{4} + \frac{\rho}{2} \right),$$

also:

$$\sigma_0 = \sigma_1 \frac{1 + \sin \rho}{1 - \sin \rho} e^{\varphi \operatorname{tg} \varphi}.$$

Für $\rho = 30^\circ$ ergibt der unsymmetrische Fall:

$$\sigma_0 = \sigma_1 \cdot 1,5 \cdot e^{\frac{10}{6} \frac{\pi}{V^3}} = 30,8 \cdot \sigma_1.$$

Für denselben Reibungswinkel ergibt der symmetrische Fall:

$$\sigma_0 = \sigma_1 \cdot 3 \cdot e^{\frac{\pi}{V^3}} = 18,4 \cdot \sigma_1.$$

Man wird nun allerdings diese Ergebnisse auf den wirklichen, immer mit Eigengewicht behafteten Sandkörper nur anwenden dürfen, wenn die Stempel- bzw. Fundamentbreite erheblich kleiner ist als die Gründungstiefe, damit die Veränderlichkeit der Eigengewichtsspannungen innerhalb des Gleitlinienbildes nicht merklich ist. RANKINE setzt bekanntlich für diesen Fall zwei nebeneinander befindliche mit einander im Gleichgewicht stehende Grenzzustände voraus und erhält:

$$\sigma_0 = \sigma_1 \left(\frac{1 + \sin \rho}{1 - \sin \rho} \right)^2,$$

also für $\rho = 30^\circ$: $\sigma_0 = 9 \cdot \sigma_1$.

Das RANKINE'sche Gleitlinienbild der Abb. 7 mit gebrochenen Gleitlinien stellt einen widerspruchsfreien Spannungszustand mit oder ohne Eigengewicht dar, ergibt aber erheblich kleinere mögliche Fundamentpressungen als die stetigen Gleitlinien der Abb. 5 und 6. Es ist übrigens bekannt, dass die RANKINE'sche Berechnung zu ungünstig ist, und die obigen Spannungszustände mit stetig gekrümmten Gleitlinien ergeben erheblich grössere zulässige Fundamentpressungen und bedeuten eine bessere Annäherung an die Wirklichkeit. Insbesondere ist das unsymmetrische Gleitlinienbild geeignet die Fundamentpressung einer seitlich belasteten Futtermauer oder eines Gewölbekämpfers wiederzugeben, da es sich hier um einen passiven Erddruck handelt und bei einem solchen der grösste mögliche Wert der massgebende ist. Auch hier ist allerdings für die theoretische Tragfähigkeit des Bodens eine gewisse Gegenbelastung etwa durch die Gründungstiefe erforderlich.

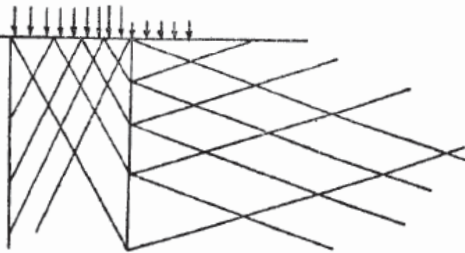


Abb. 7.

Unmöglichkeit des gradlinigen Gleitlinienbüschels bei Eigengewicht.

Versucht man nun das *gradlinig-büsselförmige System* auf den Fall des *mit Eigengewicht behafteten Erdkörpers* auszudehnen, so zeigt es sich, dass das nicht möglich ist, da die Gleigewichtsbedingungen verlangen, dass *entweder beide Gleitlinienschaaren gradlinig oder beide gekrümmmt* sind, was allerdings nicht ausschliesst, dass einzelne Gleitlinien einer gekrümmten Schaar gradlinig sind.

Aus den Gleichungen (12) folgt nämlich:

$$\frac{\partial^2 \vartheta}{\partial u \partial v} p = \gamma \left[\frac{\partial \vartheta}{\partial u} V \cos \vartheta + \frac{\partial \vartheta}{\partial v} U \sin (\vartheta - \rho) \right] \dots \quad (14)$$

Diese Gleichung lässt ohne weiteres erkennen, dass das Verschwinden der Krümmung der einen Schaar, z. B. von $\frac{1}{U} \frac{\partial \vartheta}{\partial u}$, auch das Verschwinden der anderen Krümmung $\frac{1}{V} \frac{\partial \vartheta}{\partial u}$ nach sich zieht.

Wenn es nun auch nicht möglich ist, bei Eigengewicht die eine Gleitlinienschaar büschelförmig gradlinig zu machen, so müsste es wenigstens möglich sein, zwei Individuen einer büschelförmig krummlinigen Schaar gradlinig zu machen, um auf diese Weise nach Art der Abb. 6 einen möglichen Grenzspannungszustand zwischen zwei RANKINE'schen Zuständen einspannen zu können, und dadurch Aufgaben wie die oben behandelte Fundamentaufgabe, und auch andere Wanddruckaufgaben, bei Eigengewicht durchführen zu können.

Beispiel für einen allgemeineren möglichen Grenzzustand.

Die Lösung dieser Aufgabe ist mir nicht gelungen. Ueberhaupt ist es schwierig, ausser dem RANKINE'schen weitere widerspruchsfreie Grenzzustände bei Berücksichtigung des Eigengewichts aufzufinden.

Bisher habe ich nur einen weiteren Fall aufbauen können, nämlich denjenigen, bei dem die geometrischen Gleichungen (10) dadurch linear werden, dass $\frac{\partial \vartheta}{\partial u}$ und $\frac{\partial \vartheta}{\partial v}$ konstant gesetzt werden.

Man setze also:

$$\begin{aligned}\frac{\partial \vartheta}{\partial u} &= a, \quad \frac{\partial \vartheta}{\partial v} = b, \\ \vartheta &= au + bv + c.\end{aligned}$$

Die Gleichungen (10) haben dann als lineare Differentialgleichungen das Integral:

$$U = A e^{c_1 u + c_2 v}, \quad V = B e^{c_1 u + c_2 v},$$

mit:

$$\frac{A}{B} = \frac{c_1 \sin \rho - a \cos \rho}{c_2}, \quad \frac{c_1 c_2 + ab}{c_1 b - c_2 a} = \operatorname{tg} \rho \quad \dots \dots \dots \quad (15)$$

Die Ansätze für ϑ , U und V müssen nun aber nicht nur die geometrischen Gleichungen (10), sondern auch die Gleichgewichtsbedingungen (12) erfüllen, wodurch weitere notwendige Beziehungen zwischen den Grössen a , b , A , B , c_1 und c_2 entstehen, welche folgende Gestalt erhalten:

$$\left. \begin{aligned}\frac{B(c_2 + 2b \operatorname{tg} \rho)}{b[b^2 + (c_2 + 2b \operatorname{tg} \rho)^2]} &= \frac{A[(c_1 - 2a \operatorname{tg} \rho) \sin \rho + a \cos \rho]}{a[a^2 + (c_1 - 2a \operatorname{tg} \rho)^2]} \\ \frac{B}{b^2 + (c_2 + 2b \operatorname{tg} \rho)^2} &= \frac{A[a \sin \rho - (c_1 - 2a \operatorname{tg} \rho) \cos \rho]}{a[a^2 + (c_1 - 2a \operatorname{tg} \rho)^2]}\end{aligned} \right\} \dots \dots \quad (16)$$

Aus (15) und (16) erhält man mit den Abkürzungen $\frac{c_1}{a} = \operatorname{tg} \rho_1$, $\frac{c_2}{a} = \operatorname{tg} \rho_2$:

$$\begin{aligned}\frac{8 \operatorname{tg}^2 \rho - 1}{8 \operatorname{tg} \rho} \pm \sqrt{\left(\frac{8 \operatorname{tg}^2 \rho - 1}{8 \operatorname{tg} \rho}\right)^2 + 2 \operatorname{tg}^2 \rho - 1} &= \operatorname{tg} \rho_1, \quad \frac{b}{c_2} = -\operatorname{tg}(\rho + \rho_1), \\ \frac{1 + (\operatorname{tg} \rho_1 - 2 \operatorname{tg} \rho)^2}{(\operatorname{tg} \rho_1 \operatorname{tg} \rho - 1)(3 \operatorname{tg} \rho - \operatorname{tg} \rho_1)[\operatorname{tg}^2(\rho + \rho_1) + \{1 - 2 \operatorname{tg} \rho \operatorname{tg}(\rho + \rho_1)\}^2] \cos^2 \rho} &= \operatorname{tg} \rho_2.\end{aligned}$$

Es gibt also für einen gegebenen Wert a zwei partikuläre Integrale, da $\operatorname{tg} \rho_1$ zwei Werte besitzt. Die Lösung hat offenbar nur einen Sinn, wenn b reell ist. Die entsprechende Bedingung zeigt, dass es einen Bereich von Reibungswinkeln ρ gibt, für welche die Lösung imaginär wird, nämlich der Bereich zwischen den beiden Wurzeln für $\operatorname{tg}^2 \rho_1$, der Gleichung:

$$(8 \operatorname{tg}^2 \rho - 1)^2 + 64 \operatorname{tg}^2 \rho (2 \operatorname{tg}^2 \rho - 1) = 0.$$

Soll die Lösung reell sein, so muss der absolute Wert von $\operatorname{tg} \rho$ entweder kleiner als 0,1138 oder grösser als 0,635 sein.

Der obere Wert entspricht etwa dem Böschungswinkel normalen Erdreichs. Nimmt man diesen oberen Wert, so ergibt sich:

$$\operatorname{tg} \rho_1 = 0,438, \quad \operatorname{tg} \rho_2 = 0,760,$$

demnach:

$$c_1 = 0,438\alpha, \quad c_2 = 0,760\alpha, \quad b = -1,12\alpha, \quad B = -1,25 A.$$

Die Darstellung der Gleitkurven $u = \text{const.}$ und $v = \text{const.}$ in kartesischen Koordinaten hätte etwa nach den Gleichungen (9a) zu erfolgen, scheint aber keine einfachen Kurvengleichungen zu ergeben. Man sieht jedenfalls, dass die Krümmungen $\frac{I}{U} \frac{\partial^2}{\partial u^2}$ und $\frac{I}{V} \frac{\partial^2}{\partial v^2}$ mit wachsendem u und v , d. h. nach oben abnehmen, wenn α positiv angenommen wird, und im Unendlichen in den RANKINE'schen Zustand gradliniger Gleitlinien übergehen.

Die Gleitlinie des aktiven und passiven Erddrucks.

Der andere von der Gleitlinienbeziehung (10) ausgehende Weg bietet mehr Aussicht das Ziel zu erreichen.

KÖTTER hat nämlich einsteils gezeigt, dass nach Gleichung (12) die Form der vom Mauerfuss ausgehenden Gleitlinie allein schon die Druckverteilung an ihr bestimmt und hat andererseits zuerst erkannt, dass diejenige Gleitlinie die massgebende ist, welcher der untere (aktive) bzw. der obere (passive) Grenzwert des Wanddrucks entspricht. Es kommt also darauf an, von allen, den Oberflächenbedingungen nicht widersprechenden Gleitlinien, diese massgebende zu finden. In dieser Weise kann man das KÖTTER'sche Variationsproblem des Erddrucks formulieren, wobei die Schwierigkeit darin besteht, die Mannigfaltigkeit der möglichen vom Mauerfuss aus ansteigenden Gleitlinien zu bilden. Für den Fall des horizontal begrenzten, schweren Erdkörpers, auf den wir uns hier, um eine bestimmte Vorstellung zu haben, beschränkt haben, war im ersten Abschnitt wahrscheinlich gemacht worden, dass die gesuchte Gleitlinie mit der Richtung der RANKINE'schen graden Linie ausserhalb des Winkelraums zwischen der Wand und der von der Mauerkrone aus fallenden RANKINE'schen Gleitlinie zusammenfallen muss, dass dagegen das Gleitlinienstück innerhalb jenes Winkelraums in einem gewissen Bereich willkürlich ist, je nachdem, welche fingierten Zug- oder Druckspannungen man auf der hinter der Wand liegenden fingierten Oberflächenfortsetzung annimmt.

Freilich ist die Aufgabestellung so lange nicht genügend bestimmt, als nicht über die Beweglichkeit der Wandstützung eine weitere Aussage gemacht wird.

Man kann eine solche Stützung mit eindeutigem Grenzwert des Erddrucks entweder so anordnen, dass die genannte Stützkraft nach Richtung und Angriffspunkt festgelegt ist und so lange abnimmt bzw. zunimmt, bis der Grenzwert erreicht ist (Abb. 8) oder man kann die Stützung zwar mit unbestimmter Lage und Richtung der Gesamtstützkraft einrichten, aber nur eine von den Komponenten variabel, d. h. die Wand nur in einer bestimmten Richtung beweglich machen und nach dem unteren bzw. oberen Grenzwert dieser Komponente fragen (Abb. 9).

Aus diesen Grundaufgaben lässt sich dann auch die allgemeinere, unmittelbar der Anwendung entsprechende erledigen, wann der aktive Wanddruck zusammen mit dem Eigengewicht der Mauer den passiven Fundamentdruck grade überwindet.

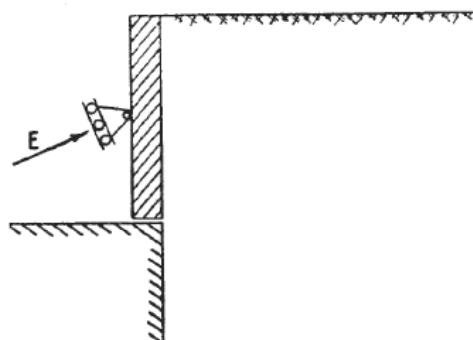


Abb. 8.

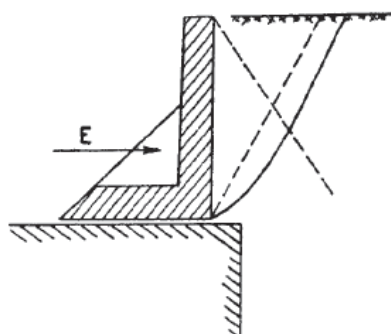


Abb. 9.

Im Anschluss an das durchgerechnete Beispiel des ersten Teils müsste hier die zweite Anordnung zugrunde gelegt und in dem obigen Zusammenhang die folgende bestimmte Frage gestellt werden:

Für waggerrechte, unbelastete Geländeoberfläche und senkrechte Wand soll diejenige Gleitlinie gefunden werden, welche nach der KÖTTER'schen Gleitlinienbeziehung (10) die kleinste Horizontalkomponente des Wanddrucks liefert. Die Mannigfaltigkeit der mit der Oberflächenbedingung verträglichen Gleitlinien ist willkürlich innerhalb des Rahmens der Lösung der AIRY'schen Spannungsgleichung (5) in dem Winkelraum zwischen der Wand und der von der Wandoberkante fallenden RANKINE'schen Gleitlinie und muss sich mit stetiger Tangente und stetigem Druck an die RANKINE'sche Gleitlinie ausserhalb des genannten Winkelraums anschliessen.

Die genauere Betrachtung dieser Aufgabenstellung scheint zu ergeben, dass sie auch wieder zurückführt auf die im ersten Teil gestellte, aber nur in den beiden ersten Näherungen beantwortete Frage nach derjenigen fingierten Oberflächenbelastung hinter der Wand, welche unter Berücksichtigung der höheren Näherungen den kleinsten Wanddruck vorgeschriebener Richtung liefert.

25 Literature

- Alamshahi, S. and Hataf, N. (2009) Bearing capacity of strip footings on sand slopes reinforced with geogrid and grid-anchor, *Geotextiles and Geomembranes*, Volume 27, Issue 3, June 2009, pp. 217-226
- Azzouz, A. S. and Baligh, M. M. (1983) Loaded areas on cohesive slopes, *Journal of Geotechnical Engineering*, vol. 109, pp. 724-729
- Bolton, M. D. (1979) *Guide to soil mechanics*, Macmillan Press, London, p. 330
- Boonstra, G. C. (1940) Eenige beschouwingen over den puntweerstand van paalen. (Some considerations of the base resistance of piles). *De Ingenieur*, 55, Febr., pp. 33-45
- Boussinesq, M. J. (1885) *Application des potentiels à l'étude de l'équilibre et du mouvement des solides élastiques, avec des notes étendues sur divers points de physique mathématique et d'analyse*, Gauthier-Villard, Paris
- Brinch Hansen, J. A. (1970) Revised and extended formula for bearing capacity, *Bulletin No 28*, Danish Geotechnical Institute Copenhagen, pp. 5-11
- Caquot, A. I. (1934) *Équilibre des massifs à frottement interne, Stabilité des terres pulvérulentes et cohérentes*, Gauthier-Villars, Paris
- Caquot, A., and Kerisel, J. (1953) Sur le terme de surface dans le calcul des fondations en milieu pulvérulent. *Proceedings 3rd International Conference on Soil Mechanics and Foundation Engineering*, Zurich, Switzerland, 16–27 August 1953, Vol. 1, pp. 336-337
- Caquot, A., and Kerisel, J. (1966) *Traité de méchanique des sols*, Gauthier-Villars, Paris, pp. 349, 353, 391
- Chakraborty, D. And Kumar, J (2013) Bearing capacity of foundations on slopes. *Geomechanics and Geoengineering, An International Journal*, 8(4), pp 274-285
- Chen, W. F. (1975) *Limit analysis and soil plasticity*, Elsevier, Amsterdam.
- Choudhary, A.K., Jha, J.N., Gill, K.S. (2010) Laboratory investigation of bearing capacity behaviour of strip footing on reinforced fly-ash slope, *Geotextiles and Geomembranes*, Volume 28, Issue 4, August 2010, pp. 393-402
- Das, B. M. (1999) *Shallow foundations, bearing capacity and settlement*, CRC Press, New York , p. 89
- De Beer, E. E. and Ladany, B. (1961) Etude expérimentale de la capacité portante du sable sous des fondations circulaire établies en surface, *Proceedings 5th International Conference on Soil Mechanics and Foundation Engineering*, Paris, Vol 1, pp. 577-581
- De Beer, E. E. (1967) Proefondervindelijke bijdrage tot de studie van het grensdraagvermogen van zand onder funderingen op staal; Bepaling van de vormfactor s_b , *Annales des Travaux Publics de Belgique*, 68, No.6, pp.481-506; 69, No.1, pp.41-88; No.4, pp.321-360; No.5, pp.395-442; No.6, pp. 495-522
- De Beer, E. E. (1970) Experimental determination of the shape factors and the bearing capacity factors of sand. *Géotechnique*, 20, N°4, pp. 387-411
- De Buhan, P. and Garnier, D. (1998) Three Dimensional Bearing Capacity Analysis of a Foundation near a Slope, *Soils and Foundations*, 38(3), pp. 153-163
- De Josselin De Jong, G. (1959) *Statics and kinematics in the failable zone of a granular material*, PhD-thesis, Delft University of Technology, pp. 36-37
- Eurocode 7 (2004) *Geotechnical design - Part 1: General rules*, EN 1997-1, 159
- Fang, Hsai-Yang (1990) *Foundation Engineering Handbook*, Kluwer, Norwell, USA / Dordrecht, the Netherlands
- Flamant, A. (1892) Sur la répartition des pressions dans un solide rectangulaire chargé transversalement. *Comptes Rendus*, Acad. Sci. Paris, vol. 114, p. 1465
- Georgiadis, K. (2010) Undrained Bearing Capacity of Strip Footings on Slopes, *J. Geotechnical and Geoenvironmental Engineering*, 136(5), pp. 677-685

- Graham, J., Andrews, M. and Shields, D.H. (1988) Stress Characteristics for Shallow Footings in Cohesionless Slope, *Canadian Geotechnical Journal*, 25(2), pp. 238-249
- Hertz, H. (1881) Ueber die Berührungen fester elastischer Körper, *Journal für die reine und angewandte Mathematik* 92, 1956, pp. 156-171
- Hjiaj, M., Lyamin, A. V., and Sloan, S. W. (2004) Bearing capacity of a cohesive-frictional soil under non-eccentric inclined loading, *Computers and Geotechnics* 31, pp. 491–516
- Ip, K. W. (2005) *Bearing capacity for foundation near slope*, Master-thesis, Concordia University, Montreal, Quebec, Canada. pp. 61-64
- Jumikis, A. R. (1956) Rupture surfaces in sand under oblique loads, *Journal of Soil Mechanics and Foundation Design*, ASCE, Vol. 82, No. 1, pp 1-26
- Keverling Buisman, A. S. (1935). De Weerstand van Paalpunten in Zand. *De Ingenieur*, 50 (Bt. 25–28), pp. 31-35
- Keverling Buisman, A. S. (1940). *Grondmechanica*, Waltman, Delft, the Netherlands, p. 227, 243
- Khitas, N. E. H., Mellas, M., Benmeddour, D. and Mabrouki, A. (2016) Bearing capacity of strip footings resting on purely cohesive soil subjected to eccentric and inclined loading, *Proc. 4th Int. Conf. on New Development in Soil Mech. and Geotechn. Eng.*, Nicosia, TRNC, pp.181-186
- Knudsen, B. S. and Mortensen, N. (2016) Bearing capacity comparison of results from FEM and DS/EN 1997-1 DK NA 2013, *Northern Geotechnical Meeting 2016*, Reykjavik, pp 577-586
- Kumar, J. and Rao, V.B.K.M. (2003) Seismic bearing capacity of foundations on slopes, *Geotechnique*, 53(3), pp. 347-361
- Lambe, T. W. and Whitman, R.V. (1969) *Soil Mechanics*, John Wiley and Sons Inc., New York.
- Leshchinsky, B. (2015) Bearing capacity of footings placed adjacent to $c'-\phi'$ slopes. *Journal of Geotechnical and Geoenvironmental Engineering*, 141 (6)
- Loukidis, D., Chakraborty, T., and Salgado, R. (2008) Bearing capacity of strip footings on purely frictional soil under eccentric and inclined loads, *Canadian Geotechnical Journal* 45, pp 768-787
- Lundgren, H. and Mortensen, K. (1953) Determination by the theory of Plasticity of the bearing capacity of Continuous Footings on Sand, *Proc. 3rd International Conference in Soil Mechanics*, Volume 1, Zürich, p. 409
- Meyerhof, G. G. (1951) The ultimate bearing capacity of foundations, *Géotechnique*, 2, pp. 301-332
- Meyerhof, G. G. (1953) The bearing capacity of foundations under eccentric and inclined loads, in *Proc. 3rd International Conference on Soil Mechanics and Foundation Engineering*, Zürich, Switzerland, 1, pp. 440-445
- Meyerhof, G. G. (1957) The ultimate bearing capacity of foundations on slopes, *Proc. of the 4th Int. Conf. on Soil Mechanics and Foundation Engineering*, London, August 1957, pp. 384-386
- Meyerhof, G. G. (1963) Some recent research on the bearing capacity of foundations, *Canadian Geotechnical Journal*, 1(1), pp. 16-26
- Meyerhof, G. G. (1965) Shallow foundations, *Journal of the Soil Mechanics and Foundations Division ASCE*, Vol. 91, No. 2, March/April 1965, pp. 21-32
- Michałowski, R. L. (1989) Three-dimensional analysis of locally loaded slopes. *Geotechnique*, 39(1), pp. 27-38
- Michałowski, R. L. (1997) An estimate of the influence of soil weight on bearing capacity using limit analysis. *Soils and Foundations*, 37(4), pp. 57–64
- Muhs, H. and Weiβ, K. (1972) Versuche über die Standsicherheit flach gegründeter Einzelfundamente in nichtbindigem Boden, *Mitteilungen der Deutschen*

Forschungsgesellschaft für Bodenmechanik (Degebo) an der Technischen Universität Berlin, Heft 28, p. 122

- Muhs, H. and Weiß, K. (1973) Inclined load tests on shallow strip footings, *Proceedings of the eight international conference on soil mechanics and foundation engineering, Moskva*, pp. 173-179
- NEN 9997-1 (NL) (Eurocode) *Geotechnical design of structures - Part 1: General rules*, pp. 107-113
- Prandtl, L. (1920) Über die Härte plastischer Körper, *Nachrichten Gesellschaft der Wissenschaften zu Göttingen, Mathematisch-Physikalische Klasse*, pp. 74-85
- Reissner, H. (1924) Zum Erddruckproblem, *Proceedings of the 1st International Congress for Applied Mechanics*, Biezeno, C. B. and Burgers, J. M. eds., Delft, the Netherlands, 295–311.
- Rinaldi, R., Abdel-Rahman, M. and Hanna, A. (2017) Experimental Investigation on Shell Footing Models Employing High-Performance Concrete, *Proceedings of the 1st GeoMEast International Congress and Exhibition on Sustainable Civil Infrastructures, Vol. Facing the Challenges in Structural Engineering*, Sharm El-Sheikh, Egypt, pp. 373-390
- Selig, E.T. and McKee, K.E. (1961) Static behavior of small footings, *Journal of Soil Mechanics and Foundation Design*, ASCE, Vol.87, pp. 29-47
- Shiau, J., Merifield, R., Lyamin, A., and Sloan, S. (2011) Undrained stability of footings on slopes. *International Journal of Geomechanics*, 11(5), pp. 381-390
- Shields, D., Chandler, N., Garnier, J. (1990) Bearing Capacity of Foundations in Slopes, *Journal of Geotechnical Engineering*, Vol 116, No 3, pp. 528-537
- Sokolovski, V. V. (1960) *Statics of soil media*, Butterworths Scientific Publications
- Tapper, L., Martin, C. M. , Byrne, B. W. Lehane, B. M. (2015) Undrained vertical bearing capacity of perforated shallow foundations, *Frontiers in Offshore Geotechnics*, Fig. 7, p. 816
- Terzaghi, K. (1943) *Theoretical soil mechanics*, John Wiley & Sons, Inc, New York.
- Tschebotarioff, G. P. (1951) *Soil mechanics, foundations, and earth structures: an introduction to the theory and practice of design and construction*, McGraw-Hill
- Türedi, Y. and Örnek, M. (2016) Investigation of stress distributions under circular footings, *Proceedings 4th International Conference on New Development in Soil Mechanics and Geotechnical Engineering*, Nicosia, TRNC, pp. 231-238
- Van Baars, S. (2014) The inclination and shape factors for the bearing capacity of footings, *Soils and Foundations*, Vol.54, No.5, October 2014, pp. 985-992
- Van Baars, S. (2015) The bearing capacity of footings on cohesionless soils, *The Electronic Journal of Geotechnical Engineering*, ISSN 1089-3032, Vol 20
- Van Baars, S. (2016a) Failure mechanisms and corresponding shape factors of shallow foundations, *Proceedings 4th International Conference on New Development in Soil Mechanics and Geotechnical Engineering*, Nicosia, TRNC, pp. 551-558
- Van Baars, S. (2016b) The influence of superposition and eccentric loading on the bearing capacity of shallow foundations, *Journal of Computations and Materials in Civil Engineering*, Volume 1, No. 3, ISSN 2371-2325, pp. 121-131
- Van Baars, S. (2017a) Numerical Check of the Meyerhof Bearing Capacity Equation for Shallow Foundations, *Proceedings of the 1st GeoMEast International Congress and Exhibition on Sustainable Civil Infrastructures, Vol. Numerical Analysis of Nonlinear Coupled Problems*, Sharm El-Sheikh, Egypt, pp. 214-226
- Van Baars, S. (2017b) The axisymmetric failure mechanism of circular shallow foundations and pile foundations in non-cohesive soils, *Journal of Computations and Materials in Civil Engineering*, ISSN 2371-2325, Vol 2, No 1, pp. 1-15

- Van Baars, S. (2017c) 100 Jaar Prandtl-Wig: De draagkrachtfaktoren, Geotechniek, Educom, Rotterdam, Dec. 2017, pp. 8-13
- Van Baars, S. (2018a) Numerical check of the Meyerhof bearing capacity equation for shallow foundations, *Journal of Innovative Infrastructure Solutions*, Springer, Berlin
- Van Baars, S. (2018b) The bearing capacity of shallow foundations on slopes, *9th European Conference on Numerical Methods in Geotechnical Engineering*, Porto
- Van Baars, S. (2018c) The failure mechanism of pile foundations in non-cohesive soils, *9th European Conference on Numerical Methods in Geotechnical Engineering*, Porto
- Van Mierlo, J.C. and Koppejan, A.W. (1952) Lengte en draagvermogen van heipalen, *Bouw*, No. 3
- Verruijt, A and Van Baars, S. (2007) *Soil mechanics*, VSSD, Delft
- Vesic, A. S. (1967) *A study of bearing capacity of deep foundations*, Final Report Project B-189, Georgia Institute of Technology, Atlanta, pp. 231-236
- Vesic, A. S. (1973) Analysis of ultimate loads of shallow foundations. *Journal of Soil Mechanics and Foundation Division*, 99(1), pp. 45-76
- Vesic, A.S. (1975) Bearing capacity of shallow foundations, H.F. Winterkorn, H.Y. Fang (Eds.), *Foundation Engineering Handbook*, Van Nostrand Reinhold, New York (1975), pp. 121-147
- White, D.J. and Bolton M.D. (2005) Comparing CPT and Pile base resistance in sand, *Geotechnical Engineering*, 158, Jan. 2005, pp. 3-14
- Witt, Karl Josef (ed) (2018) *Grundbau-Taschenbuch*, Teil 3: Geotechnische Bauwerke, Ernst & Sohn, Part Flachgründungen (Norbert Vogt)
- Yamamoto, K. (2010) Seismic Bearing Capacity of Shallow Foundations near Slopes using the Upper-Bound Method, *Int. J. Geotechnical Engineering*, 4(2), 255-267
- Yu, H.S., Salgado, R., Sloan, S.W., Kim, J.M. (1998) Limit analysis versus limit equilibrium for slope stability, *Journal of Geotechnical and Geoenvironmental Engineering*, Jan. 1998, Vol 124, No 1, pp. 1-11
- Zhu, M. and Michalowski, R.L. (2005) Shape factors for limit loads on square and rectangular footings, *Journal of Geotechnical and Geoenvironmental Engineering*, ASCE, Febr., pp. 223-231

26 Background of the author

Prof. dr. ir. Stefan Van Baars (1968) studied Civil Engineering at the Delft University of Technology and specialised in two fields: Geotechnical Engineering and Hydraulic Engineering. He obtained his PhD degree in Delft in 1996. His PhD thesis entitled “*Discrete element analysis of granular materials*” was awarded Summa Cum Laude. This research was extended with a post-doctoral research position at the University of Sydney.

After Sydney, Stefan Van Baars worked first for the Dutch Ministry of Transport and Public Works on bored tunnels, and subsequently for the Dutch contracting company Strukton on pile foundations and building pits for the high speed trains. He returned in 2001 to the faculty of Civil Engineering of the Delft University of Technology as an assistant professor. There he worked for the chair of Structural Hydraulic Engineering for three years and for the chair of Soil Mechanics for six years. In this position he visited twice the University of Grenoble (Sabbatical leave at Université Joseph Fourier and Invited Professor at the Ecole National de Polytechnique Grenoble). In 2010 he was appointed as full professor of Foundation Engineering and Soil Mechanics at the University of Luxembourg.



This page intentionally left blank